Contents

ASM Sc. J.
Volume 3(1), 2009

RESEARCH ARTICLES

Continued on the inside of the back cover.

ISSN 1823-6782

MOSTI

AKADEMI SAINS MALAYSIA

ASM Science Journal 3(1) 2009

ASM JOURNAL Science

In Pursuit of Excellence in Science

Vol. 3, No. 1, June 2009 • ISSN : 1823-6782

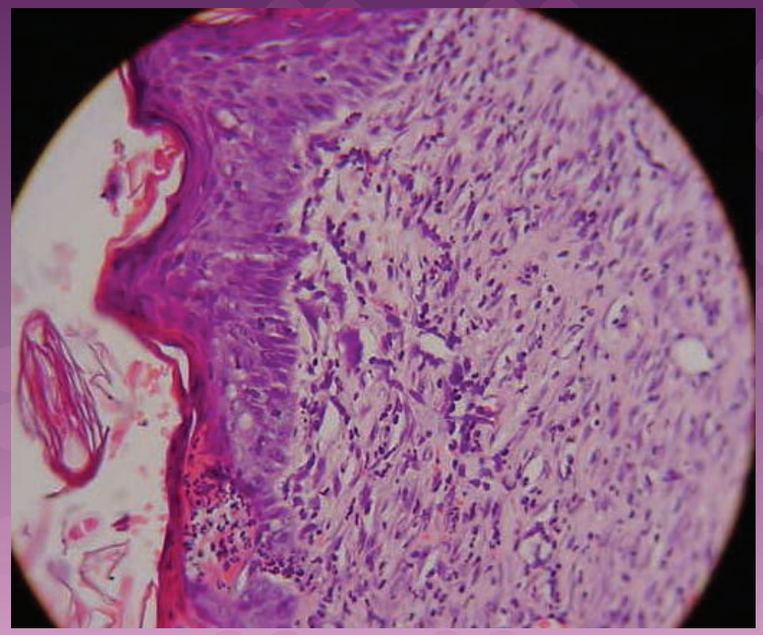

Price (2 Issues)

Malaysia: RM100 (*Individual*)
RM200 (*Institution*)

Other Countries: USD50 (*Individual*)
USD100 (*Institution*)

ASM Science
JOURNAL

Cover:

Researchers from the University of Malaya working in the area of molecular medicine, chemistry, oral medicine and periodontology have collaborated in assessing the effects of topical application of *Orthosiphon stamineus* leaf extract on the rate of wound healing and histology of healed wound. This enlarged H&E stain image (original magnification of *Figure 7* about 40 × found in page 56) in the article entitled "Acceleration of Wound Healing by *Orthosiphon stamineus* Leaf Extract in Rats" shows the histological section of healed wound dressed with blank placebo. The granulation tissue contains less collagen, fibroblast and blood capillaries and more inflammatory cells.

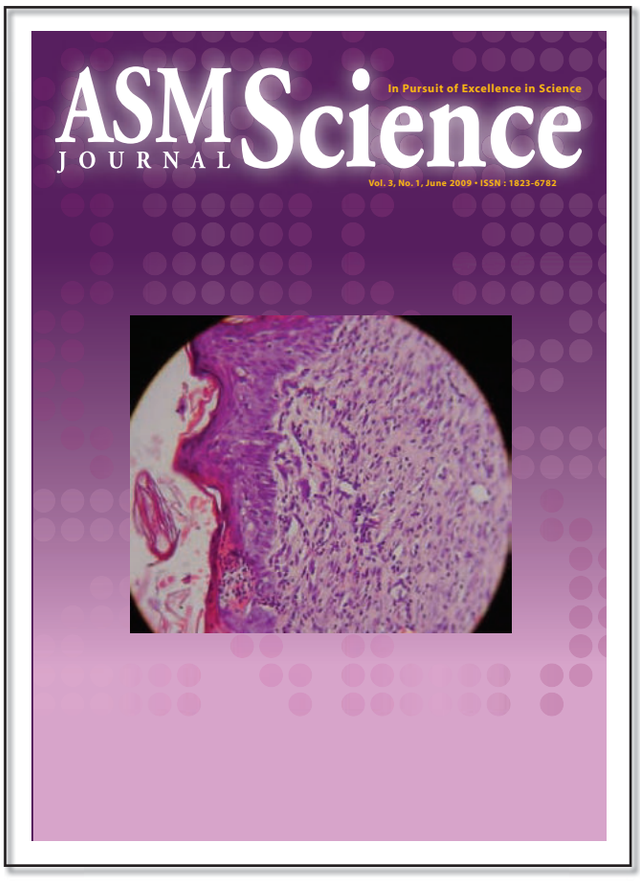

Published by the Academy of Sciences Malaysia

The Academy of Sciences Malaysia (ASM)

The Academy of Sciences Malaysia (ASM) was established, under the *Academy of Sciences Act 1994* which came into force on 1 February 1995, with the ultimate aim to pursue excellence in science. Thus the mission enshrined is to pursue, encourage and enhance excellence in the field of science, engineering and technology for the development of the nation and the benefit of mankind.

The functions of the Academy are as follows:

- To promote and foster the development of science, engineering and technology
- To provide a forum for the interchange of ideas among scientists, engineers and technologists
- To promote national awareness, understanding and appreciation of the role of science, engineering and technology in human progress
- To promote creativity among scientists, engineers and technologists
- To promote national self-reliance in the field of science, engineering and technology
- To act as a forum for maintaining awareness on the part of the Government of the significance of the role of science, engineering and technology in the development process of the nation and for bringing national development needs to the attention of the scientists, engineers and technologists
- To analyse particular national problems and identify where science, engineering and technology can contribute to their solution and accordingly to make recommendations to the Government
- To keep in touch with developments in science, engineering and technology and identify those developments which are relevant to national needs to bring such developments to the attention of the Government
- To prepare reports, papers or other documents relating to the national science, engineering and technology policy and make the necessary recommendations to the Government
- To initiate and sponsor multi-disciplinary studies related to and necessary for the better understanding of the social and economic implications of science, engineering and technology
- To encourage research and development and education and training of the appropriate scientific, engineering and technical man power
- To establish and maintain relations between the Academy and overseas bodies having the same or almost similar objectives in science, engineering and technology as the Academy
- To advise on matters related to science, engineering and technology as may be requested by the Government from time to time; and
- To carry out such other actions that are consistent with the *1994 Academy of Sciences Act* as may be required in order to facilitate the advancement of science, engineering and technology in Malaysia, and the well being and status of the Academy.

The Academy is governed by a Council. Various Working Committees and Task Forces are charged with developing strategies, plans and programmes in line with the Academy's objectives and functions.

The functions of the Council are:

- To formulate policy relating to the functions of the Academy
- To administer the affairs of the Academy
- To appoint such officers or servants of the Academy as are necessary for the due administration of the Academy
- To supervise and control its officers and servants
- To administer the Fund; and
- To convene general meetings of the Academy to decide on matters which under this Act are required to be decided by the Academy.

The Academy has Fellows and Honorary Fellows. The Fellows comprise Foundation Fellows and Elected Fellows. The Academy Fellows are selected from the ranks of eminent Malaysian scientists, engineers and technocrats in the fields of medical sciences, engineering sciences, biological sciences, mathematical and physical sciences, chemical sciences, information technology and science and technology development and industry.

The Future

Creativity and innovation are recognised the world over as the key measure of the competitiveness of a nation. Within the context of K-Economy and the framework of National Innovation System (NIS), ASM will continue to spearhead efforts that will take innovation and creativity to new heights in the fields of sciences, engineering and technology and work towards making Malaysia an intellectual force to be reckoned with.

Contents

ASM Sc. J.
Volume 3(1), 2009

RESEARCH ARTICLES

RESEARCH ARTICLES

REVIEW

ANNOUNCEMENTS

ASM Sci. J., **3(1)**, 1–5

Effect of Matrix Transformation on Minimization of Quadratic Functional

J.O. Omolehin[1*], M.K.A. Abdulrahman[2], K. Rauf[1] and A.O. Ameen[3]

The convergence profile of the conventional Conjugate Gradient Method (CGM) algorithm is based on the symmetry of the control operator for quadratic functions.

This work considers the quadratic functions with a non-symmetric control operator under suitable matrix transformations. It was proved that the conventional CGM algorithm produced results that were favourably comparable in relation to problems with symmetric control operator equivalent.

Key words: quadratic functions; convergence profile; conjugate gradient method; matrix transformation; symmetric control operator

Consider the quadratic functional of the form:

$$f(x) = f_0 + \langle a, X \rangle_H + \frac{1}{2}\langle X, AX \rangle_H \quad (1)$$

where A is an $n \times n$ symmetric positive definite constant matrix operator on Hilbert space H, a is a vector in H and f_0 is a constant term. The conventional CGM algorithm is used as a computation method for the minimization of the above problem and it has been proved that the CGM algorithm enjoys a quadratic rate of convergence. That is the method converges in at most n iterations for an n-dimensional problem, what follows is the convergence rate of the CGM algorithm.

CONVERGENCE PROFILE OF THE CONVENTIONAL CGM ALGORITHM

To fully understand the numerical task reported in this work it will be necessary to show the convergence rate of CGM algorithm (Abdul Rahman 2007; Ibiejugba *et al*. 2003; Jonathan 1994; Lipschutz 1987; Omolehin 2006; Omolehin & Rauf 2006).

Recall the quadratic functional:

$$f(X) = f_o + \langle a, X \rangle_H + \frac{1}{2}\langle X, AX \rangle_H$$

where f_0 is a constant, H is a Hilbert space, X is a nxn dimensional vector in H, a positive definite constant matrix operator (John & Karin 2001; Wayne, Charles & Pablo 1993).

The convergence rate of the CGM algorithm is given as:

$$E(X_n) = \left\{\frac{1-\frac{m}{M}}{1+\frac{m}{M}}\right\}^{2n} E(X_o)$$

where m and M are the smallest and largest eigen values of A, respectively.

Proof: see (Ibeijugba *et al*. 2003).

Define $E(X) = \frac{1}{2}\langle (X - X^*), A(X - X^*) \rangle_H$

Therefore,

$$\begin{aligned} E(X) &= \frac{1}{2}\langle (X - X^*), A(X - X^*) \rangle_H \\ &= \frac{1}{2}\langle X + A^{-1}a, A(X + A^{-1}a) \rangle_H \\ &= \frac{1}{2}\langle X + A^{-1}a, AX + AA^{-1}a \rangle_H \\ &= \frac{1}{2}\langle X + A^{-1}a, AX + a, AX + a \rangle_H \\ &= \frac{1}{2}\langle X, AX \rangle_H + \frac{1}{2}\langle X, a \rangle_H + \frac{1}{2}\langle A^{-1}a, AX \rangle_H \\ &\quad + \frac{1}{2}\langle A^{-1}a, a \rangle_H \end{aligned}$$

[1] Mathematics Department, University of Ilorin, Ilorin, Nigeria
[2] Mathematics, Statistics and Computer Science Department, Kaduna Polytechnic, Kaduna, Nigeria
[3] Computer Science Department, University of Ilorin, Ilorin, Nigeria
Corresponding author (e-mail: omolehin_joseph@yahoo.com)

$$= \frac{1}{2}\langle X, AX\rangle_H + \frac{1}{2}\langle X, a\rangle_H + \frac{1}{2}\langle A^{-1}a, AX\rangle_H + \frac{1}{2}\langle -X^*, a\rangle_H$$

$$= \frac{1}{2}\langle X, AX\rangle_H + \frac{1}{2}\langle X, a\rangle_H + \frac{1}{2}\langle X^*, AX^*\rangle_H + \frac{1}{2}\langle A^{-1}a, AX\rangle_H$$

$$E(x) = F(X) - F_o + \frac{1}{2}\langle X^*, AX^*\rangle_H = F(X) - \tilde{F}(o)$$

Therefore, *E(X)* is *F(X)* plus a constant term, hence the convergence of *E(X)* is considered instead of that of *F(X)* as from now.

Recall that:

$$E(X) = \frac{1}{2}\langle X + A^{-1}a, AX + a\rangle_H = \frac{1}{2}\langle A^{-1}(AX + a), AX + a\rangle_H = \frac{1}{2}\langle A^{-1}g(X), g(X)\rangle_H$$

Hence,

$$E(X_i) - E(X_{i+1}) = \frac{1}{2}\langle X_i - X^*, A(X_i - X^*)\rangle_H - \frac{1}{2}\langle X_{i+1} - X^*, A(X_{i+1} - X^*)\rangle_H$$

But,

$X_{i+1} = X_i + \alpha_i p_i$, therefore:

$$E(X_i) - E(X_{i+1}) = \frac{1}{2}\langle X_i - X^*, A(X_i - X^*)\rangle_H - \frac{1}{2}\langle X_i + X_i p_i - X^*, A(Xi + \alpha_i p_i - X^*)\rangle_H$$

$$= \frac{1}{2}\langle X_i - X^*, A(X_i - X^*)\rangle_H - \frac{1}{2}\langle X_i - X^*, A(X_i - X^*)\rangle_H - \frac{1}{2}\alpha_i\langle p_i, A(X_i + \alpha_i p_i - X^*)\rangle_H - \frac{1}{2}\alpha_i\langle X_i - X^*, Ap_i\rangle_H$$

$$= -\frac{\alpha_i}{2}\langle p_i, A(X_i - X^*)\rangle_H - \frac{1}{2}\alpha_i\langle X_i - X^*, Ap_i\rangle_H - \frac{1}{2}\alpha_i\langle p_i, A\alpha_o p_o\rangle_H$$

$$= -\alpha_i\langle p_i, Ax_i + a\rangle_H - \frac{1}{2}\alpha_i{}^2\langle p_i, Ap_i\rangle_H - \frac{1}{2}\alpha_i^2\langle p_i, Ap_i\rangle_H$$

$$= -\alpha_i\langle p_i, g_i\rangle_H - \frac{1}{2}\alpha_i\langle g_i, g_i\rangle \quad \text{since } \alpha_i = \frac{\langle g_i, g_i\rangle_H}{\langle p_i, Ap_i\rangle_H}$$

$$= -\alpha_i\langle -g_i + \beta_{i-1}p_{i-1}, g_i\rangle_H - \frac{1}{2}\alpha_i\langle g_i, g_i\rangle_H$$

$$= \alpha_i\langle g_i, g_i\rangle_H - \alpha_i\beta_{i-1}\langle p_{i-1}, g_i\rangle_H - \frac{1}{2}\alpha_i\langle g_i, g_i\rangle_H$$

$$= \alpha_i\langle g_i, g_i\rangle - \frac{1}{2}\alpha_i\langle g_i, g_i\rangle_H \quad (\text{since } \langle p_{i-1}, g_i\rangle_H = 0 \text{ by orthogonality of } p_{i-1} \text{ and } g_i)$$

$$= \alpha_i\langle g_i, g_i\rangle_H - \frac{1}{2}\alpha_i\langle g_i, g_i\rangle_H = \frac{1}{2}\alpha_i\langle g_i, g_i\rangle_H = \frac{\frac{1}{2}\langle g_i, g_i\rangle^2{}_H}{\langle p_i, Ap_i\rangle_H} \quad \text{because } \alpha_i = \frac{\langle g_i, g_i\rangle}{\langle p_i, Ap_i\rangle}$$

Hence,

$$E(X_i) - E(X_{i+1}) = \frac{\langle g_i, g_i\rangle^2{}_H E(X_i)}{\langle p_i, Ap_i\rangle_H \langle g_i, A^{-1}g_i\rangle_H}$$

Using the fact that $g_i = \beta_{i-1}p_{i-1} - p_i$, where $\beta_{i-1} = \frac{\langle g_i, g_i\rangle_H}{\langle g_{i-1}, g_{i-1}\rangle_H}$

We get:

$$\langle g_i, Ag_i\rangle_H = \langle \beta_{i-1}p_{i-1}, A(\beta_{i-1}p_{i-1} - p_i)\rangle_H = \beta_{i-1}{}^2\langle p_{i-1}, Ap_{i-1}\rangle_H + \langle p_i, Ap_i\rangle_H$$

$\geq \langle p_i, Ap_i\rangle_H$, since $\langle p_{i-1}, Ap_{i-1}\rangle_H \geq 0$ (due to the positive definiteness of operator *A*),

$$\langle g_i, Ag_i\rangle_H \geq \langle p_i, Ap_i\rangle_H$$

Therefore,

$$E(X_i) - E(X_{i+1}) \geq \frac{\langle g_i, g_i\rangle^2{}_H E(X_i)}{\langle g_i, Ag_i\rangle_H \langle g_i, A^{-1}g_i\rangle_H}$$

But for a bounded self-adjoint operator in a Hilbert space *H*, Kantorovich (Hasdorff 1976; Andrew & Chelsea 1977; Pinch 1993) established the following inequality:

$$\frac{\langle X, X\rangle^2{}_H}{\langle X, AX\rangle_H \langle X, A^{-1}\rangle_H} \geq \frac{4mM}{(m+M)^2},$$ where m and M are respectively the greatest lower and least upper bounds of the spectrum of operator *A*. Using Kantorovich's inequality, we obtain:

$$E(X_{i+1}) \leq \left\{\frac{1 - \frac{m}{M}}{1 + \frac{m}{M}}\right\}^{2n} E(X_o), \text{ for all } m \leq M.$$

This shows the convergence rate of the CGM.

MATRIX TRANSFORMATION

Suppose A is a non-symmetric matrix, it is then partitioned into two parts as follows:

$$A = \frac{1}{2}(A + A^T) + \frac{1}{2}(A - A^T) \tag{2}$$

where, the first part is symmetric and the second part is skew symmetric. For subsequent development, the second part can be neglected since the main diagonal elements will be zero. We can now replace our new matrix by B as follows:

$$B = \frac{1}{2}(A + A^T) \tag{3}$$

where, B is the symmetric transform of A.

MAIN RESULTS

Suppose the operator A in (Equation 1) is non-symmetric, we now replace A by B in Equation 3 to obtain:

$$f(x) = f_0 + \langle a, X\rangle_H + \frac{1}{2}\langle X, BX\rangle_H \tag{4}$$

where, B is the transform of A.

Theorem

Suppose B is the symmetric transform of A in Equation 3 then,

(i) the functional (Equation 1) is equivalent to the functional (Equation 4)

(ii) $\frac{1}{2}\langle X, AX\rangle_H = \frac{1}{2}\langle X, BX\rangle_H$

Proof

Let $f : \Re^n \to \Re$ then the minimization of f is given by:

$$f(X) = f_0 + \langle a, X\rangle_H + \frac{1}{2}\langle X, AX\rangle_H$$

and,

$$f(X) = f_0 + \langle a, X\rangle_H + \frac{1}{2}\langle X, BX\rangle_H$$

where, A is the non-symmetric nxn matrix and B is the symmetric transform of A. It is enough to prove (ii). Let,

$$\frac{1}{2}X^T AX = \frac{1}{2}.\begin{pmatrix} x_1 \\ x_2 \\ . \\ . \\ x_n \end{pmatrix}^T . \begin{pmatrix} a_{11} & a_{12} & . & . & a_{1n} \\ a_{21} & a_{22} & . & . & a_{2n} \\ . & . & . & . & . \\ . & . & . & . & . \\ a_{n1} & a_{n2} & . & . & a_{nn} \end{pmatrix} \begin{pmatrix} x_1 \\ x_2 \\ . \\ . \\ x_n \end{pmatrix}$$

$$= \frac{1}{2}(a_{11}x_1^2 + a_{22}x_2^2 + \ldots + a_{nn}x_n^2 + (a_{12} + a_{21})x_1x_2 + \ldots + (a_{1n} + a_{n1})x_1x_n + (a_{2n} + a_{n2})x_2x_n + \ldots + (a_{n,n-1} + a_{n-1,n})x_nx_n) \tag{5}$$

Also,

$$\frac{1}{2}X^T BX = \frac{1}{2}.\begin{pmatrix} x_1 \\ x_2 \\ . \\ . \\ x_n \end{pmatrix}^T . \begin{pmatrix} a_{11} & \frac{a_{12}+a_{21}}{2} & . & . & \frac{a_{1n}+a_{n1}}{2} \\ \frac{a_{21}+a_{12}}{2} & a_{22} & . & . & \frac{a_{2n}+a_{n2}}{2} \\ . & . & . & . & . \\ . & . & . & . & . \\ \frac{a_{1n}+a_{n1}}{2} & \frac{a_{2n}+a_{n2}}{2} & . & . & a_{nn} \end{pmatrix} \begin{pmatrix} x_1 \\ x_2 \\ . \\ . \\ x_n \end{pmatrix}$$

$\Rightarrow$

$$= \frac{1}{2}(a_{11}x_1^2 + a_{22}x_2^2 + \ldots + a_{nn}x_n^2 + (a_{12} + a_{21})x_1x_2 + \ldots + (a_{1n} + a_{n1})x_1x_n + (a_{2n} + a_{n2})x_2x_n + \ldots + (a_{n,n-1} + a_{n-1,n})x_nx_{n-1}) \tag{6}$$

Therefore, the two functionals are equivalent. Equations 5 and 6 are equal and the result follows. The necessary conditions for the minimization of the two functionals are:

$$\nabla f(X) = a^T + AX = a^T + BX = 0 \tag{7}$$

and the respective optimum will be:

$$X^* = -aA^{-1} = -aB^{-1} \tag{8}$$

NUMERICAL RESULTS

Minimize:

$$f(X) = f_0 + \langle a, X\rangle_H + \frac{1}{2}\langle X, AX\rangle_H$$

and compare the result with the minimization of

$$f(X) = f_0 + \langle a, X\rangle_H + \frac{1}{2}\langle X, BX\rangle_H$$

for the following problems:

Problem 1:

$$f_0 = 1 \quad a = (1,1) \quad A = \begin{pmatrix} 1 & 2 \\ 3 & 4 \end{pmatrix}$$

Problem 2:

$$f_0 = 1 \quad a = (1,1,1) \quad A = \begin{pmatrix} 2 & 2 & 3 \\ 2 & 0 & 1 \\ 2 & 4 & 2 \end{pmatrix}$$

Problem 3:

$$f_0 = 1 \quad a = (1,1,1,1) \quad A = \begin{pmatrix} 1 & 1 & 2 & 3 \\ 2 & 0 & 4 & 5 \\ 3 & 1 & 2 & 0 \\ 0 & 2 & 1 & 3 \end{pmatrix}$$

Problem 4:

$$f_0 = 1 \quad a = (1,1) \quad A = \begin{pmatrix} 3 & 1 \\ 3 & 4 \end{pmatrix}$$

Problem 5:

$$f_0 = 1 \quad a = (1,1,1) \quad A = \begin{pmatrix} 1 & 2 & 1 \\ 1 & 4 & 3 \\ 2 & 1 & 3 \end{pmatrix}$$

Problem 6:

$$f_0 = 1 \quad a = (1,1,1,1) \quad A = \begin{pmatrix} 1 & 1 & 1 & 3 \\ 1 & 2 & 1 & 1 \\ 1 & 1 & 3 & 0 \\ 0 & 2 & 1 & 3 \end{pmatrix}$$

The optimal results of quadratic functionals with non-symmetric operators and their symmetric transform equivalent is depicted in Table 1.

CONCLUSION

X^* is the optimum and $^f(X^*)$ is the optimal value. It can be seen from the table that the optimal values for non-symmetric B and the symmetric operator A corresponding to the transform B are favourably comparable. The

Table1. Optimal results of quadratic functionals with non-symmetric operators and their symmetric transform equivalent.

	Optimal values with A		Optimal values with B	
	X^*	$^f(X^*)$	X^*	$^f(X^*)$
Problem 1	(–1, 1)	1	(0.667, –0.667)	1
Problem 2	(0.5, 0, 0)	0.75	(–0.222, 0, –0.222)	0.778
Problem 3	(3.753, –1.251, –5.004, 2.502) × 10^{14}	–2.053 × 10^{13}	(–0.046, –0.148, –0.234, –0.099)	0.737
Problem 4	(–0.3333,0)	0.833	(–0.25, –0.125)	0.813
Problem 5	(–0.75, –0.25, 0.25)	0.625	(–2.8, 0.4, 0.8)	0.2
Problem 6	– (0.235, 0.235, 0.176, 0.118)	0.618	(–5, 0, 1, 2)	0

next study will consider the convergence rate of our transform.

Date of submission: July 2008
Date of acceptance: December 2008

REFERENCES

Abdulrahman, MKA 2007, 'Conjugate gradient method for solving non-symmetric matrix operators', M. Sc. dissertation.

Andrew, PS & Chelsea, CW 1977, *Optimum system control,* 2nd edn, Prentice-Hall, New Jersey.

Pinch, ER 1993, *Optimal control and the calculus of variation*, Oxford University Press, New York.

Ibiejugba, MA *et al*. 2003, *Foundation postgraduate course on computational methods and application in optimization*, National Mathematical Centre, Abuja, Nigeria.

John, MH & Karin, M 2001, "PDMATRIX"—Programs to make matrix positive definite.

Jonathan, RS 1994, *An Introduction to the conjugate gradient method without agonizing pain*.

Hasdorff, L 1976, *Gradient optimization and nonlinear control*, John Wiley & sons, London.

Lipschutz, S 1987, *Theory and problems of linear algebra (Metric Edition)*, McGraw-Hill Inc., Singapore.

Omolehin, JO 2006, 'Further result on CGM Algorithm', *Journal of the Mathematical Association of Nigeria*, vol. 33, no. 2b, pp. 374–388.

Omolehin, JO & Rauf, K 2006, 'Computational capability of CGM algorithm', *Creative Math. and Inf*., no. 15, pp. 93–106.

Wayne, B, Charles, RJ & Pablo, T 1993, 'The real positive definite completion problem for a simple cycle', *Journal of Linear Algebra and its Application*, vol. 192, pp. 3–31.

ASM Sci. J., **3(1)**, 7–16

Fractal Dimension Algorithm for Automatic Detection of Oil Spills in RADARSAT-1 SAR

M. Marghany[1*], A.P. Cracknell[1] and M. Hashim[1]

This paper introduces a method for modification of the formula of the fractal box counting dimension. The method is based on the utilization of the probability distribution formula in the fractal box count. The purpose of this method is to use it for the discrimination of oil spill areas from the surrounding features e.g. sea surface and look-alikes in RADARSAT-1 SAR data. The result showed that the new formula of the fractal box counting dimension was able to discriminate between oil spills and look-alike areas. The low wind area had the highest fractal dimension peak of 2.9, as compared to the oil slick and the surrounding rough sea. The maximum error standard deviation of the low wind area was 0.68 which performed with a 2.9 fractal dimension value.

Key words: fractal analysis; algorithms; oil spill detection; RADARSAT-1 SAR; probability distribution; look-alikes

Synthetic aperture radar (SAR) has been recognized as a powerful tool for oil spill detection. Several algorithms have been introduced for the automatic detection of oil spills in SAR images. These algorithms have involved three steps: (i) dark spot detection, (ii) dark spot feature extraction, and (iii) dark spot classification. Various classification algorithms for oil spill detection have been utilized, including pattern recognition algorithm (Fukunaga 1990), spatial frequency spectrum gradient (Lombardini *et al*. 1989; Trivero *et al*. 1998) and fuzzy and neural networks technique (Mohamed *et al*. 1999; Calabresi *et al*. 1999). Dark spot detection is done by adaptive thresholding. This step is controlled by wind conditions and the type of SAR sensors. However, threshold procedures have failed to detect thin and linear slicks. Available *in situ* wind measurements can be used to determine the threshold while the local homogeneity can be used to determine the threshold if there are no *in situ* wind measurements. In fact, oil spill detection by SAR images is not at all an easy task. For one thing there are other physical phenomena apart from oil slicks which can also generate dark patches and for another thing, SAR images are affected by multiplicative noise known as speckle. In this context, dark patches that are not due to oil spills are described as look-alikes. They can be due to low wind speed area, internal waves, biogenic films, grease ice, wind front areas, areas sheltered by land, rain cells, current shear zones, and up-welling zones (Petromar 1981; Lombardini *et al*. 1989; Trivero *et al*. 1998; Calabresi *et al*. 1999).

In this context, the power-to-mean ratio is considered as a good measurement of texture homogeneity. Utilization of sea surface homogeneity in a SAR image is a function of wind speed conditions. For high or medium wind speeds greater than about 3 ms^{-1}, the sea water surrounding dark areas will appear fairly homogenous. This explains the weak possibilities of the presence of oil spill look-a-likes in SAR scenes under these conditions. However with a low wind speed of less than 3 ms^{-1}, there could be a large number of oil spill look-a-likes present in SAR imagery (Trivero *et al*. 1998). The detection of oil spill and look-a-like features in SAR scenes can be obtained by using power-to-mean ratio values. The power-to-mean ratio is used to adjust the threshold. Various authors (Solberg & Solberg 1996; Solberg & Volden 1997; Kanna *et al*. 2003 & Nirchio *et al*. 2005) have reported that for RADARSAT-1 SAR, thresholding is done at three different scales. However, using three different scales did not work well for ENVISAT due to the larger pixel size of the selected product types.

A new approach was introduced by Maged (2001) to detect thin and linear slicks by using the Lee algorithm (Touzi 2002). The Lee Filter is primarily used on radar data to remove high frequency speckle without removing edges or sharp features in the images. Maged and van Genderen (2001), reported that the Lee algorithm operates well to determine linear slick features. According to Maged (2001), the Lee algorithm avoids decreasing resolution by making a weighted combination of running average which reduces the noise in the slick's edge areas without sacrificing edge sharpness. Recently, Huang *et al*. (2005) explored the segmentation of oil slicks using a partial differential equation (PDE)-based level set method with ERS-2 SAR data. They concluded that the level set method allows an extraction of smooth and ideal boundaries rather

[1] Department of Remote Sensing, Faculty of Geoinformation Science and Engineering, Universiti Teknologi Malaysia, 81310 UTM, Skudai, Johore Bahru, Malaysia

[*] Corresponding author (e-mail: maged@fksg.utm.my; magedupm@hotmail.com)

than a number of zigzag edges. However, this method failed to distinguish between oil slicks and dark spot areas that were located close to the coastline due to low wind speed and were not oil slicks. In fact, this method produced automatic snake contours around the presence of any dark spot areas in SAR imagery. Furthermore, Maged and van Genderen (2001) introduced a new approach by using texture algorithms for the automatic detection of oil spills in a RADARSAT-1 SAR image. In fact, grey-tone spatial-dependence or co-occurrence matrices provide the basis for a number of measures including range, variance, standard deviation, entropy, or uniformity within a moving kernel window (Tricot 1993). However, computing the texture features from a co-occurrence matrix may become critical due to the multiplicative noise impacts. Different approaches to texture identification have been introduced that involve exploiting the fractal algorithm which can be estimated from a specific multi-resolution representation of the SAR images. Fractal analysis provides tools for measuring how the geometric complexity (the number of discrete objects, perimeter to area ratios and degree of spatial auto-correlation) of imaged objects changes when the image resolution is altered. The main question that can be raised is how the fractal algorithm can be used to discriminate between oil spills and look-alikes in RADARSAT-1 SAR data.

FRACTAL ANALYSIS AND SAR DATA

According to Redondo (1996) fractal geometry can be used on occasion to discriminate between different textures. A fractal refers to entities, especially sets of pixels, which display a degree of self-similarity at different scales. Self-similarity is the foundation for fractal analysis and is defined as a property of a curve or surface where each part is indistinguishable from the whole, or where the form of the curve or surface is invariant with respect to scales, meaning that the curve or surface is made of copies of itself at reduced and enlarged scales (Pentland 1984).

The most well known procedures that have been proposed for estimating the fractal dimension of SAR images are box counting, fractal Brownian motion (Falconer 1990; Gado & Redondo 1999 ; Benelli & Garzelli 1999) and fractal interpolation function system dimension of images (Aiazzi *et al*. 2001). Initially, Falconer (1990) introduced the fractional Brownian motion model with SAR image intensity variation which has shown promise in the SAR data textures. In fact, both the sea surface and its backscattered signal in the SAR data can be modeled as fractals (Wornell & Oppenheim 1992; Maragos & Sun 1993; Benelli & Garzelli 1999; Aiazzi *et al*. 2001).

By contrast, Gado and Redondo (1999) found that a box counting fractal dimension model provided excellent discrimination between oil spills and look-alikes, although the backscatter information which could allow an initial robust localization of the oil spills, had not been considered. Furthermore, Benelli and Garzelli (1999) used a multi-resolution algorithm which was based on fractal geometry for texture analysis. They found that the sea surface was characterized by an approximately steady value of fractal dimension, while the oil spills have a different average fractal dimension compared to look-alikes.

This work has hypothesized that the dark spot areas (oil slick or look-alike pixels) and their surrounding backscattered environmental signals in the SAR data could be modeled as fractals. In this context, a box-counting fractal estimator could be used as a semiautomatic tool to discriminate between oil spills, look-alikes and surrounding sea surface waters. In addition, the utilization of a probability density formula in the box-counting equation could improve the accuracy of discrimination between oil slick pixels and surrounding feature pixels such as ocean surface and look-alikes. The procedures which were used to discriminate oil spills from the surrounding sea surface environment are shown in Figure 1.

METHODOLOGY

Data Set

The SAR data acquired in this study were from the RADARSAT-1 Standard 2 beam mode (S2) image. According to Hashim *et al*. (2006), an oil spill occurred on 20 December 1999 along the coastal water of the Malacca Straits. The RADARSAT-1 SAR is a C-band instrument with a variable acquisition swath, presenting a large variety of possible incidence angles, swath widths, and resolutions (RADARSAT International 2006). It is argued that oil slicks can be detected with a contrast as small as 4 dB (Kotova *et al*. 1998; Farahiday *et al*. 1998; Lu *et al*. 2000). This indicates that a large part of the RADARSAT-1 swath could be useful for oil slick detection. Recently, Ivanov *et al.* (2002) reported that the RADARSAT-1 SAR, in its ScanSAR Narrow mode with swath width that exceeds 300 km, is an attractive tool for marine oil pollution detection. They showed that the entire ScanSAR image can be used for oil slick detection, at least for suitable wind conditions.

The standard two beam mode is C-band and has a low signal-to-noise ratio due to its HH polarization with wavelength of 5.6 cm and frequency of 5.3 GHz. The RADARSAT-1 SAR standard two beam data has spatial resolution of 12.5 m × 12.5 m and the swath area of 110 km × 100 km. The incidence angle is between 23.7º and 31.0º (RADARSAT International 2006).

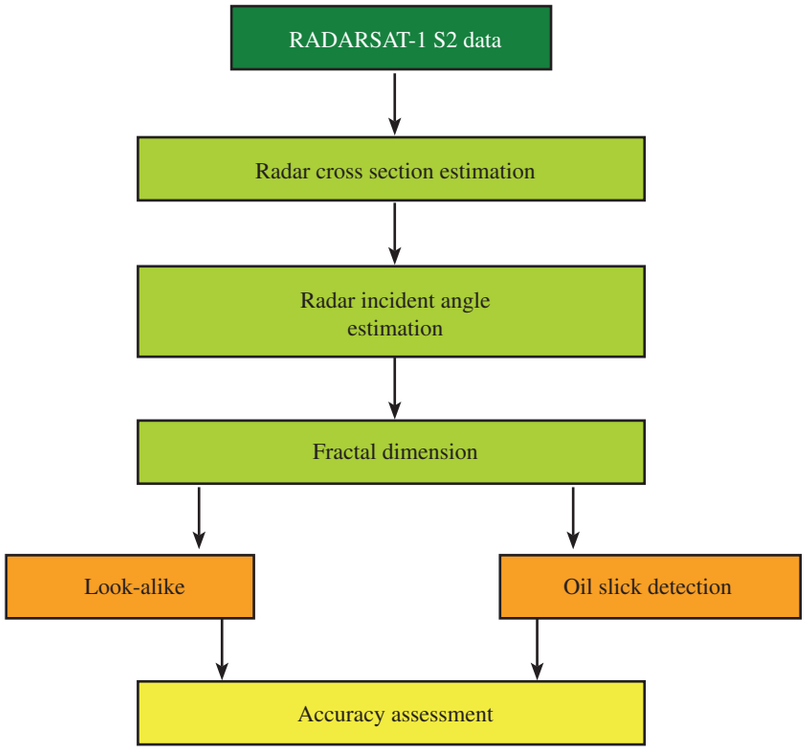

Figure 1. Block diagram of fractal dimension algorithm.

Fractal Algorithm for the Oil Spill Identification

The oil slick detection tool uses fractal algorithms to detect the self-similar characteristics of RADARSAT-1 SAR image intensity variations. A box-counting algorithm introduced by Benelli and Garzelli (1999) was used in this study. The box counting algorithm was used to divide a convoluted line of slick which was embedded in the SAR image plane (*i,j*), into smaller boxes. This was done by dividing the initial length of the convoluted line of the slick at backscatter level β_s by the recurrence level of the iteration (Gado & Redondo 1999). We define a decreasing sequence of backscattering β_s tending from β_0 the largest value, to less than or equal to zero. The fractal dimension D (β_s) as a function of the RADARSAT-1 SAR image intensity β_s is given by:

$$D(\beta_s) = D_B = \lim_{s \to \infty} \frac{\log M(\beta_s)}{-\log(\beta_s)} \quad (1)$$

where, $M(\beta_s)$ denotes the number of boxes which are needed to cover the various slick areas with different backscatter intensity β_s in the RADARSAT-1 SAR image. In addition, the subscript *s* indicates the backscatter amplitude and its unit is dB. The number of boxes was non-overlapping which was calculated from the fractal dimension algorithm and had a square shape with side length l_s unit. This is an odd, positive integer centred on an arbitrary point in the RADARSAT-1 SAR backscatter image surface. Therefore, side length was needed to cover a fractal profile, of backscatter image β_s^{-D}, where D is the fractal dimension that was to be estimated. Moreover, the box numbers were chosen based on the length of convoluted line of slick at backscatter level β_s. If the profile being sampled is a fractal object, then $M(\beta_s)$ should be proportional to β_s^{-D}, i.e., the following relation, which was adopted from Milan *et al*. (1993), should be satisfied:

$$M(\beta_s) = C\beta_s^{-D} \quad (2)$$

where C is a positive constant derived from a linear regression analysis between log $M(\beta_s)$ and log (β_s). As different box sizes were needed to cover the length of convoluted line of slick at backscatter level β_s, a number of points were produced in the log-log plane. The dimension $D(\beta_s) = D_B$ could be estimated from a linear regression of these points (Milan *et al*. 1993).

In practice, it is difficult to compute $D(\beta_s)$ using Equation 1 due to the discrete RADARSAT-1 SAR images surfaces, and so approximations to this relationship are employed. First, the RADARSAT-1 SAR intensity image β is treated as a two-dimensional matrix ($\beta \times \beta$). This $\beta \times \beta$ intensity image matrix is divided into non-overlapping or abutted windows of size $l \times l$, where l is the length of

the convoluted line of the slick in the RADARSAT-1 SAR image ($\beta \times \beta$). In addition, for each window, there is a column of accumulated boxes, each box with size of $l^2_s \times l$. The backscatter values (β_0) are stored at each intersection of the column *i* and row *j* of the various slick areas. Then *l* is calculated by using the differential box counting proposed by Sarkar and Chaudhuri (1994):

$$\left[\frac{\beta_s}{l}\right] = \left[\frac{\beta}{l_s}\right] \tag{3}$$

Let the minimum and maximum (β_s) in the (*i, j*) window fall in boxes numbered *n* and *m*. The total number of boxes needed to cover the various slick pixels in the RADARSAT-1 SAR image with the box size $l^2_s \times l$ is:

$$M(\beta_s) = \sum_{i,j}^{l} n(\beta_0) - m(\beta_s) + 1 \tag{4}$$

Let $P[M(\beta_s), l_s]$ be the probability of the total number of boxes $M(\beta_s)$ with box sizes l_s. This probability should be directly proportional to the number of boxes $\sum_{i,j}^{l} n(\beta_0) - m(\beta_s) + 1$ spanned on the windows. By using Equation 4, the expected number of boxes with size which is needed to cover the slick pixels can be calculated using the following formula:

$$M(\beta_s) = \sum_{i,j} \frac{1}{n} P[M(\beta_s), l_s] \tag{5}$$

According to Fiscella *et al*. (2000), the probability distribution of the dark area belonging to slick pixels can be calculated using the formula below:

$$P[M(\beta_s)] = \{1 + \prod_n q_n[M(\beta_s)] / p_n[M(\beta_s)]\} \tag{6}$$

Let $n = \sum_{i,j}^{l} n(\beta_0) - m(\beta_s) + 1$, q and p be the probability distribution functions for look-alike and oil spill pixel areas, respectively. From Equations 5, 6 and 1 one can get a new formula for estimating the fractal dimension D_B:

$$D(\beta_s) = D_B = \lim_{s \to \infty} \frac{\log \sum_{i,j} n^{-1} \{1 + \prod_n q_n[M(\beta_s)] / p_n[M(\beta_s)]\}}{-\log(\beta_s)} \tag{7}$$

In practice, the limit of M going to zero cannot be taken as it does not produce a texture image for oil spills or look-alikes in SAR data. Using fractal dimensions to quantize texture for segmentation, we may divide the slick's pixel areas into overlapping sub-images. Each sub-image is centred on the pixel of interest. We then estimate the fractal dimension $D(\beta_0)$ within each sub-image, and assign the fractal dimension value to the central pixel of each sub-image. This will produce a textured image that may be used as an additional feature in slick pixel classification.

RESULTS AND DISCUSSIONS

The RADARSAT-1 SAR Standard 2 beam mode (S2) image was selected for testing the proposed fractal algorithm. The RADARSAT-1 SAR image detail in Figure 2 contains a confirmed oil-slick which occurred near the west coast of Peninsular Malaysia on 20 December 1999 (Hashim *et al*. 2006). Figure 3 shows the variation of the average backscatter intensity along the azimuth direction in the oil-covered area as a function of the incidence angle for RADARSAT-1 SAR. The backscattered intensity is damped by –10 dB to –18 dB which is above the RADARSAT-1 noise floor value of nominally –20 dB. The RADARSAT-1 image covered an area located in between 101º 01' 01.01" E to 101º 17' 11.5" E and 2º 25' 38.6" N to 2º 34' 23.5" N. This result of backscatter variation across oil spill locations agrees with the study of Maged and Mazlan (2005).

The proposed method for estimating the fractal dimension was applied to the raw RADARSAT-1 SAR data by using a 10×10 block at full resolution (Figure 4). Figure 4b showed the resulting fractal map. The fractal dimension map showed good discrimination between different textures on the RADARSAT-1 SAR image. The resulting fractal dimension map appeared to correlate well with image texture regions (Figures 4a and 4b). The oil slick pixels were dominated by lower fractal values than look-alikes and the surrounding environment (Figure 4b). It was interesting to find that the region of the oil slick had fractal values between 1.5 and 2.3 which might indicate the spreading of the oil spill. As the fractal dimension value increased, the oil spill become more thin which could be noticed in areas of A to C. In fact, a thick oil spill dampens small scale waves and reduces the roughness of the sea surface compared to a thin oil spill, so that there is no Bragg resonance (Bern *et al*. 1993). In this context, the fractal dimension is a function of sea surface level intensities over the RADARSAT-1 SAR image which expresses the self similarity (Benelli & Garzelli 1999). The fractal dimension values of look-alikes are between 2.6 and 2.8 which could be seen in the areas F and E. The highest fractal dimension values of 3.4 and 4.0 in the areas D and G represented the occurrence of shear current flow and the presence of a ship, respectively (Table 1). However, we could expect the fractal dimensions to be within 2 – 3, but not 1.5 – 3.6. This would be attributed to the high impact of speckles existing in the RADARSAT-1 SAR image. It was interesting to discover that the fractal dimension algorithm based probability was able to extract ship wake information in area H with a value of 3.6. This indicated that the corresponding value of fractal dimension for different categories allowed a multi-fractal characterization of the different features in a RADARSAT-1 SAR image. These results confirm the study of Maged & Mazlan (2005).

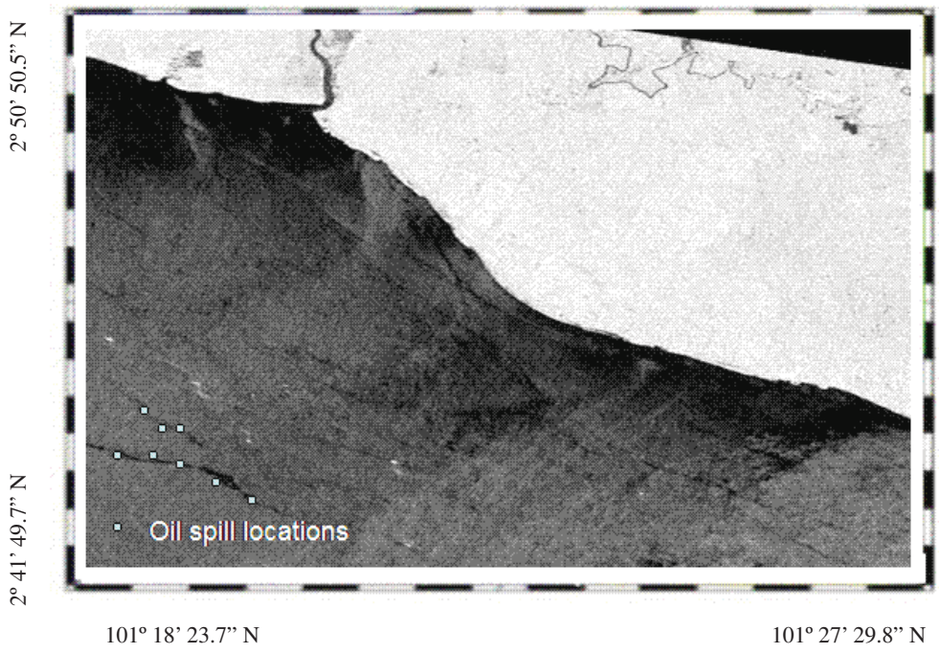

Figure 2. Oil spill locations are indicated by small squares.

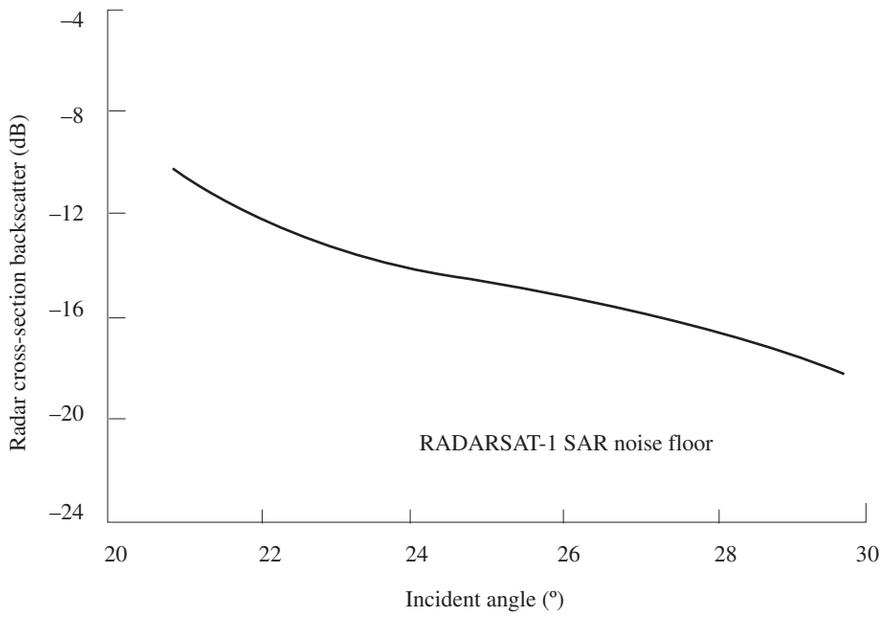

Figure 3. Radar cross-section intensity along oil slick locations.

Table 1. Fractal dimension with different classes.

Areas	Fractal dimension
Oil spill	
A	1.5
B	2.3
C	1.9
Shear current	
D	3.4
Look-alikes	
E	2.8
F	2.6
Ship	
G	4.0
H	3.6

Figure 5 shows the density slicing of the fractal map for the large scale area of Figure 2. It could be seen that the low wind zone areas were observed close to the coastline with a 2.6 fractal value. The look-alikes occupy narrow areas which were observed parallel to the coastline with a 2.8 fractal value. The wide distribution of dark zone pixels represents the natural slick in low wind areas (Henschel *et al.* 1997) which is aligned with what could be a current shear or convergence zone. This result confirms the output result of Figure 4b. By contrast with natural slicks and low wind areas, the oil slicks were located away from the coastline with fractal values between 2.0 and 2.6 which agrees with Figure 4b. The density slicing map (Figure 5) confirmed the result of oil spill spreading which was shown in Figure 4b.

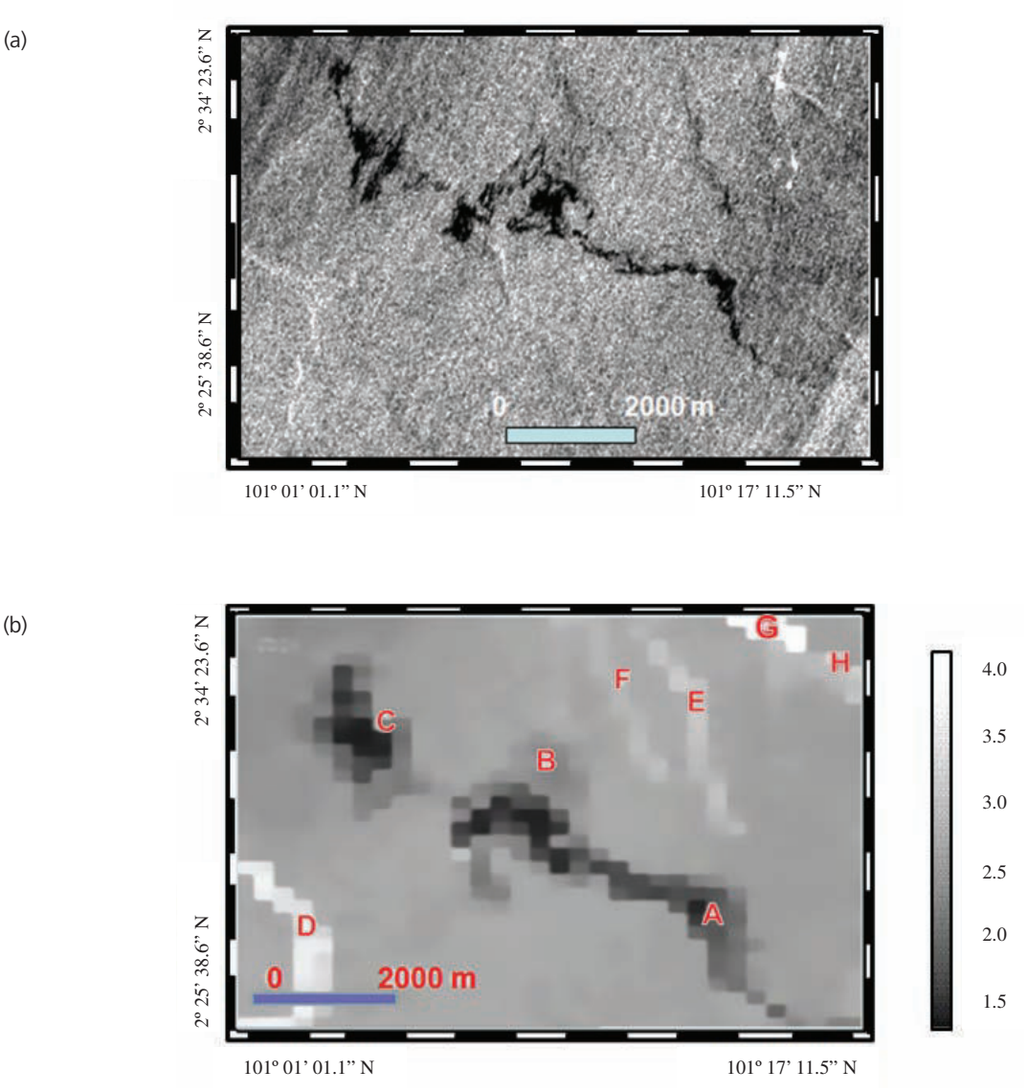

Figure 4. (a) RADARSAT-1 SAR texture feature of oil spill and (b) fractal map.

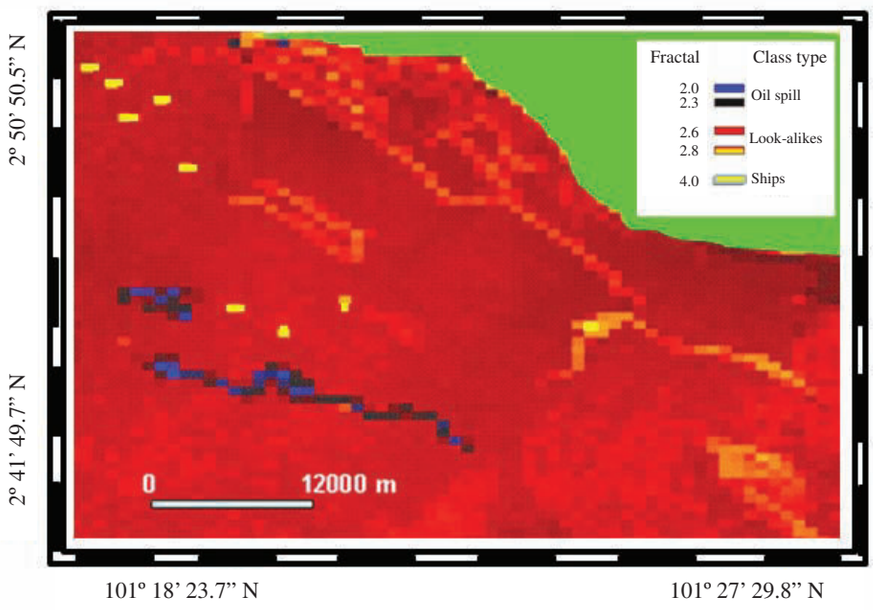

Figure 5. Density slicing map for fractal dimension.

Figure 6 shows the comparison between the oil slick fractal dimension curve and the surrounding environment condition curves. The maximum fractal value of 4.0 was observed for a group of ships with a 0.9 normalized backscatter value. However, ships and its wakes are not considered as fractal features. In this circumstance, the ship's pixels and its wake had higher values than oil spill, look-alikes and sea surface. This confirmed the study of Bertacca *et al*. (2005) and indicates that the strong amplitude of variation in a RADARSAT-1 SAR image can be mapped as fractal discontinuities and small details are easily detected, e.g. ships. This result confirms the study of Maged and Mazlan (2005). Furthermore, it was apparent that the oil spill areas had a parabolic curve with a maximum fractal dimension peak value of 2.3 and normalized RADARSAT-1 SAR backscatter value of 0.03 (Figure 6). It was also found that the sea surface was dominated by a wide steady peak of fractal dimension (Figure 6), which was 2.7, while the oil spill had substantially different values of fractal dimension, which ranged between 1.9 and 2.6 (Figure 6). In fact, the sea surface is considered as a non-fractal object. According to Falconer (1990), the slope measure of non-fractal objects corresponds to the complexity of the objects, with the natural implication that the sea surface would have a steady value (Figure 6). By contrast, the look-alike had a normal distribution curve with fractal dimension peak of 2.8 and the normalized backscatter was between 0.15 and 0.55; this was distinguishable from the oil slick and the surrounding rough sea (Figure 6). There appeared to be a reduction in the maximum fractal dimension of the oil slick compared to that of the look-alike. This could be due to the short spatial extent of the oil spill. It could also be seen that there are small differences of 0.2 and 0.3 between the fractal values of the maximum peaks of look-alike, sea surface and oil spill, respectively (Figure 6). This could be attributed to high surface wind speed which induced sea surface roughness in the RADARSAT-1 SAR image along the surrounding area of the oil slicks and look-alike areas. This made small differences between the fractal results for oil spills and the surrounding sea surface (Bertacca *et al.* 2005).

Figure 7 shows the density probability distribution of the fractal dimension values of oil slick, look-alikes and low wind zones. The oil slick had a lower peak value of density probability compared to the look-alike and low wind zones. The oil slick probability density peak was 0.27 while the look-alike and low wind zones peak values were 0.39 and 0.43, respectively. Figure 8 shows an exponential relationship between fractal dimension and standard deviation of the estimation error for fractal dimension of oil spill, look-alike and sea surface pixels. In Figure 8, the ship and its wake pixels were not taken into account as they were not considered as fractal. The maximum error standard deviation was 0.68 which corresponded to the 0.29 fractal dimension value. This could be attributed to the fact that the fractal dimension could be viewed as a measure of the scale of the self-similarity of the object. In a statistical fractal set, the interference looks statistically similar if the scale was reduced which is similar to the result of Bertacca *et al.* (2005). This indicates that fractal analysis is a good

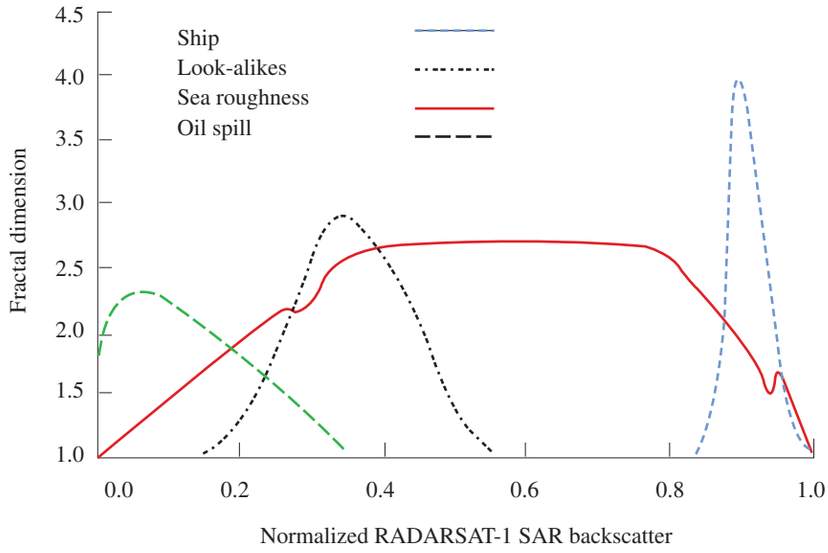

Figure 6. Fractal dimension curve for different features.

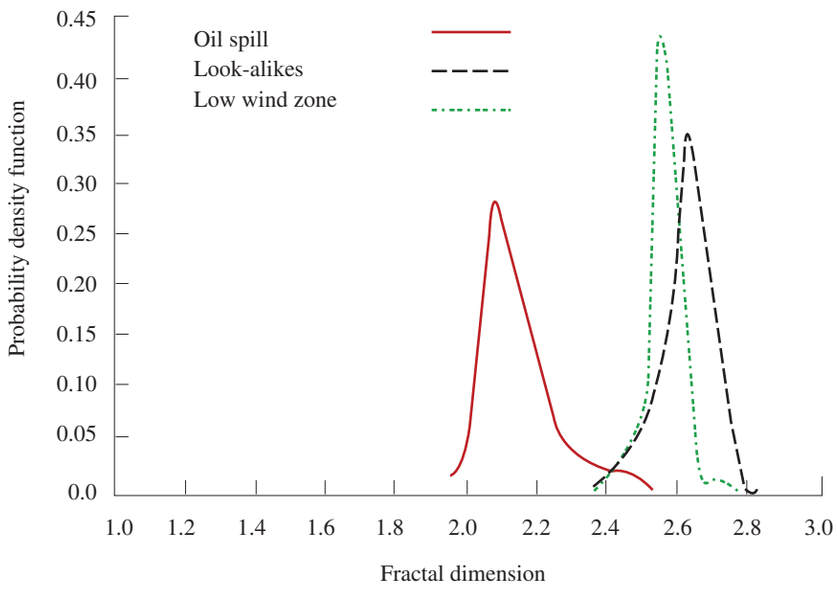

Figure 7. Probability density for fractal dimension distribution.

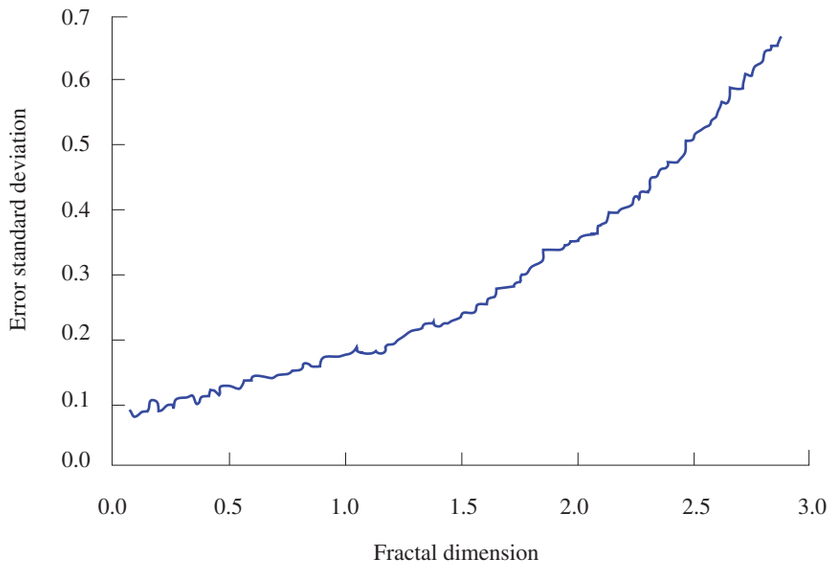

Figure 8. Accuracy assessment of fractal dimension performance for oil spill, look-alike and sea state pixels.

method to discriminate regions of oil slick from surrounding water features.

The use of fractal dimension based on the probability distribution function (PDF) improved the discrimination between oil spill, look-alikes, sea roughness and low wind zones. In fact, involving the PDF formula in the fractal dimension map directly related the textures at different scales to fractal dimensions. In addition, this modification of the fractal equation reduced the problems of speckle and sea clutter and assists in the accurate classification of different textures over SAR images.

CONCLUSION

The utilization of RADARSAT-1 SAR imagery for oil slick detection was implemented by using a fractal dimension algorithm as an automatic tool to discriminate between an oil slick and other surface features such as slick look-alikes and variability of surface roughness. The oil spill had characteristic values of fractal dimension which ranged between 1.9 and 2.6. The sea surface roughness had a steady value of 2.6 fractal dimension. The interesting result was that the low wind area was characterised by the highest value of 2.9 fractal dimension. It can be said that the new approach of the fractal box counting dimension algorithm could be used as an automatic tool for oil spill, and look-alike detections.

Date of submission: April 2008
Date of acceptance: December 2008

REFERENCES

Aiazzi, B *et al.* 2001, 'Multiresolution estimation of fractal dimension from noisy images', *SPIE-IS&T Journal of Electronic Imaging*, vol. 10, pp. 339–348.

Benelli,G & Garzelli, A 1998, 'A multi-resolution approach to oil-spills detection in ERS-1 SAR images', *Image and Signal Processing for Remote Sensing*, vol. 4, pp. 145–156.

Benelli, G & Garzelli, A 1999, 'Oil-spill detection in SAR images by fractal dimension estimation', in *Proceedings of Geoscience and Remote Sensing Symposium, IGARSS'99, Hamburg, Germany, 28 June–2 July*, IEEE Geoscience and Remote Sensing Society, USA. Vol. 2, pp. 1123–1126.

Bern, TI *et al*. 1993, 'Oil spill detection using satellite based SAR; experience from a field experiment', *Photogrammetric Engineering and Remote Sensing*, vol. 59, pp. 423–428.

Bertacca, M, Berizzi, F & Mese, ED 2005, 'A FARIMA-based technique for oil slick and low-wind areas discrimination in sea SAR imagery', *IEEE Transactions on Geosciences and Remote Sensing*, vol. 43, pp. 2484–2439.

Calaberesi, G *et al*. 1999, 'Neural networks for the oil spill detection using ERS-SAR data. In *Proceedings of Geoscience and Remote Sensing Symposium, IGARSS'99, Hamburg, Germany, 28 June – 2 July*, IEEE Geoscience and Remote Sensing Society, USA, vol. 1, pp. 215–217.

Farahiday, I, Suryono, GF & Arvelyna, Y 1998, 'Utilization of RADARSAT SAR data for oil slick detection and vessel ship monitoring application: ADRO 630 project', *GIS and remote sensing year book*, Academic press, New York, BPPT 97/98.

Fiscella, B *et al.* 2000, 'Oil spill detecting using marine SAR images', *International Journal of Remote Sensing*, vol. 21, No. 18, pp. 3561–3566.

Falconer, K 1990, *Fractal geometry*, John Wiley & Sons, New York.

Fukunaga, K 1990, *Introduction to statistical pattern recognition*, 2nd edn, Academic Press, New York.

Gade, M & Redondo, JM 1999, 'Marine pollution in european coastal waters monitored by the ERS-2 SAR: a comprehensive statistical analysis', In *Proceedings of Geoscience and Remote Sensing Symposium, IGARSS'99, Hamburg, Germany, 28 June-2 July*, IEEE Geoscience and Remote Sensing Society, USA, vol. 2, pp. 1375–1377.

Hashim, M, Ibrahim, AL & Ahmad, S 2006, 'Mapping and identifying oil spill occurrences in Malaysian water (Straits of Malacca and South China Sea) using 2000-2005 archived Radarsat-1 SAR', Evaluation Report, Department of Remote Sensing, Universiti Teknologi Malaysia.

Henschel, MH *et al*. 1997, 'The ocean monitoring workstation: experience gained with RADARSAT', in *Proceedings of Geomatics in the Era of RADARSAT*, Canadian Center of Remote Sensing, 25–30 May, Ottawa.

Huang, B, Li, H & Huang, X 2005, 'A level set method for oil slick segmentation in SAR images', *International Journal of Remote Sensing*, vol. 26, pp. 1145–1156.

Ivanov, A, He, M & Fang, MQ 2002, 'Oil spill detection with the RADARSAT SAR in the waters of the Yellow and East Sea: a case study', in *23rd Asian Conference on Remote Sensing, 13–17 November, Nepal,* Asian Remote Sensing Society, Japan, vol. 1, pp. 1–8.

Kanna, T *et al*. 2003, 'Detection of oil slick signatures in SAR images by fusion of hysteresis thresholding responses', in *Proceedings of Geosciences and Remote Sensing Symposium, IGARSS'03, Toulouse, France, 8 June–12 June*, IEEE Geosciences and Remote Sensing Society, USA, vol 3, pp. 2750–2752.

Kotova, L, Espedal, HA & Johannessen, OM 1998, 'Oil spill detection using spaceborne SAR: a brief review', in *Proceedings of 27th International Symposium on Remote Sensing Environmental*, 8–12 June, Norwegian Defence Research Establishment, Tromsø, pp. 791–794.

Lombardini, PP *et al*. 1989, 'Modulation of the spectra of short gravity waves by sea surface films: slick detection and characterization with microwave probe', *Journal of Atmospheric and Oceanic Technology*, vol. 6, 882–890.

Lu, J, Kwoh, LK & Lim, H 2000, 'Mapping oil pollution from space', *Backscatter* (February), pp. 23–26.

Maragos, P & Sun, FK 1993, 'Measuring the fractal dimension of signals: morphological covers and iterative optimization', in *IEEE Transactions on Signal Processing*, vol. 41, pp. 108–121.

Maged, M 2001, 'RADARSAT automatic algorithms for detecting coastal oil spill pollution', in *International Journal of Applied Earth Observation and Geoinformation*, vol. 3, pp.191–196.

Maged, M & van Genderen, J 2001, 'Texture algorithms for oil pollution detection and tidal current effects on oil spill spreading', *Asian Journal of Geoinformatics*, vol. 1, pp. 33–44.

Maged, M & Mazlan, H 2005, 'Simulation of oil slick trajectory movements from the RADARSAT-1 SAR', *Asian Journal of Geoinformatics*, vol. 5, pp. 17–27.

Milan, S, Vachav, H & Roger, B 1993, '*Image processing analysis and machine vision*', Chapman and Hall Computing, New York.

Mohamed IS, Salleh, AM & Tze, LC 1999, 'Detection of oil spills in Malaysian waters from RADARSAT Synthetic Aperture Radar data and prediction of oil spill movement', in *Proceeding of 19th Asian Conference on Remote Sensing, China, Hong Kong, 23–27 November*, Asian Remote Sensing Society, Japan, vol. 2, pp. 980–987.

Nirchio, F *et al*. 2005, 'Automatic detection of oil spill from SAR images', *International Journal of Remote Sensing*, vol. 26, pp. 1157–1174.

Petromar 1981, *Petroleum and the marine environment*, Graham and Trotman, London.

Pentland, AP 1984, 'Fractal-based description of natural scenes', in *IEEE Transactions Pattern Analysis and Machine Intelligent*, vol. 6, pp. 661–674.

Redondo, JM 1996, 'Fractal Description of density interfaces', *Journal of Mathematics and its Applications*, vol. 5, 210–218.

RADARSAT International 2006, *RADARSAT applications* <(http:\ www.rsi.ca\March 3, 2006)>.

Sarkar, N & Chaudhuri, BB 1994, 'An efficient differential box-counting approach to compute fractal dimension of image', in *IEEE Transactions Systems, Man. Cyber-net*, vol. 24, 115–120.

Solberg, AHS & Solberg, R 1996, 'A large-scale evaluation of features for automatic detection of oil spills in ERS SAR images', In *International Geosciences and Remote Sensing Symposium´96, 27-31 May, Lincoln, Nebraska*, IEEE Geosciences and Remote Sensing Society , USA, vol. 3, pp.1484–1486.

Solberg, AHS & Volden, E 1997, 'Incorporarion of prior knowledge in automatic classification of oil spills in ERS SAR images', In *International Geosciences and Remote Sensing Symposium´97, 3–8 Aug., Singapore*, IEEE Geosciences and Remote Sensing Society, USA, vol. 1, pp.157–159.

Teivero, P *et al*. 1998, 'SAR detection and characterization of sea surface slicks', *International Journal of Remote Sensing*, vol. 19, 543–548.

Tricot, C 1993, *Curves and fractal dimension*, Springer Verlag.

Touzi, R 2002, 'A review of speckle filtering in the context of estimation theory', *IEEE Transactions on Geosciences and Remote Sensing*, vol. 40, pp. 2392–2404.

Wornell, GW & Oppenheim, A 1992, 'Estimation of fractal signals from noisy measurements using wavelets', *IEEE Transactions Signal Processing*, vol. 40, pp. 611–623.

ASM Sci. J., **3(1)**, 17–26

Non-linear Analysis of Water Thrust on Bakun Concrete Faced Rockfill Dam

M.H. Ahmad*[1], J. Norzaie[2], F. Al Qbadi[2] and B.D. Daniel[1]

The functions of dams are for water supply, flood control and hydroelectric power generation. A concrete faced rockfill dam (CFRD) is preferred by dam consultants due to its many advantages. It is designed to withstand all applied loads, namely gravity load due to its massive weight and hydrostatic load due to water thrust from the reservoir. The structural response of the Bakun CFRD which is the second highest dam in the world after the Shuibuya Dam, was analyzed using finite element method. A two-dimensional plane strain finite element analysis of the non-linear Duncan-Chang hyperbolic model was used in the study of the dam in respect to the deformation and stresses of the main dam of Bakun CFRD project. The Dead-Birth-Ghost element technique was used to simulate sequences of the construction of the dam. The comparison of rigid and flexible foundation on the behaviour of the dam is discussed in this study. In the finite element modeling, the concrete slab on the upstream was represented through a six-noded element, while the interface characteristic between the dam body and the concrete slab was modeled using an interface element. The maximum settlement and stresses of the cross-section were found and their distribution was discussed and tabulated in the form of contours. The effect of reservoir filling loading had a gradual effect on the dam response behaviour. Comparisons with no water impoundment in the dam were also discussed.

Key words: CFRD dams; non-linear; finite element analysis; water fillings; Bakun Dam; simulation; reservoir; hydrostatic pressure; plane strain

With rapid population growth and accelerating economic development, the supply of electricity and water to the masses requires urgent attention to ensure sustainable usage. Dams form a part of a controlled irrigation system but they also have other roles to play, i.e. in flood control and hydroelectric power generation. There are a few factors that are needed to be considered carefully when designing a dam, i.e. safety, economy, efficiency and appearance. Since the construction of dams are considered as mega infrastructure projects and for any nation, many international organizations such as the International and National Commission on Large Dams (ICOLDS) are necessarily involved in the documentation of data of a Concrete Faced Rockfill Dam (CRFD) in its design and construction stage. Dams are designed to withstand all applied loads, e.g. gravity load, hydrostatic pressures, hydrodynamic pressures, etc. CFRD is recognized as one of the best choices by dam consultants and engineers for its advantages.

The principal safety of CFRD is studied mainly through its structural responses such as deformation and stresses. In this study, 2-D software was used to study the structural response of the Bakun Dam. The written program has Simulation of Birth, Dead and Ghost element techniques, input parameters for non-linear analysis, contact between different material representing interface behaviour and simulation of loading during dam construction and reservoir filling. Structural analysis was conducted considering two types of load: the first type was the load due to self-weight only which was taken during the period of construction; while the second type was self-weight plus hydrostatic force from reservoir filling. The objectives of this paper are to study the effect of hydrostatic pressure and also to compare the behaviour of the Bakun Dam for rigid and flexible foundations.

PREVIOUS FINDINGS

Nobari and Duncan (1972a and 1972b) have presented a method for computation of movements in dams due to reservoir filling. The technique has been applied to Oroville Dam, California and it shows good agreement between computed and measured values for horizontal movements. Alberro (1972) compared field measurements with finite

[1]Structural and Material Engineering Dept., Faculty of Civil and Environmental Engineering, Universiti Tun Hussein Onn Malaysia (UTHM), 86400 Parit Raja, Batu Pahat, Johor, Malaysia

[2]Civil Engineering Department, Faculty of Engineering, Universiti Putra Malaysia, 43400 UPM Serdang, Selangor, MALAYSIA

* Corresponding author (e-mail: hilton@uthm.edu.my)

element computations for the El Infiernillo Dam in Mexico. The computed and measured values in this case were found not to be in agreement. This discrepancy was primarily due to the sensitivity of the elastic constants used in the analysis of stresses, load history and testing techniques.

Xingzheng *et al*. (2002) used 3-D finite element analysis to evaluate stresses and deformation of the Yutiao CFRD in China during its construction and reservoir filling stage. He found that the maximum horizontal displacement occured 0.34 m upstream and 0.47 m downstream during the final stages of construction. After the reservoir was filled, the peak deformation was observed at 0.22 m upstream while the downstream reading was the same as during the construction stage. Maximum vertical displacement however, showed its peak settlement at 0.82 m and in the case after filling the reservoir, the settlement increased slightly. Maximum major and minor principal stresses of the dam during construction showed values of 1.78 MPa and 0.74 MPa, respectively and occured at the bottom of the dam. After filling the reservoir, it gave readings of 1.87 MPa and 0.70 MPa, respectively.

Chen *et al*. (2000) used the nonlinear elastic developed hyperbolic method, model E-B, by Duncan *et al*. (1984), to analyze Shuibuya Dam's (233 m) concrete face rockfill. The maximum horizontal deformation of the dam was 0.20 m upstream at the end of construction, while it was 0.67 m downstream at the end of filling the reservoir. The maximum vertical deformation occurred at 2/3 of the dam height with a value of 1.67 m at the end of construction and 0.77 m at the end of filling the reservoir. The maximum principle major and minor stresses are 3.18 MPa and 1.02 MPa, respectively, at the end of construction, and, 3.52 MPa and 1.27 MPa at the end of reservoir filling.

Khalid *et al*. (1990) developed a two dimensional nonlinear finite element program and studied in great detail, the structural response of the Cethana CFRD, located in Australia. The maximum vertical and horizontal stresses in both cases at the end of construction and at the end of impounding, occurred at the mid-bottom of the dam. Instrumentation installed at Centhana Dam provided comprehensive data on the structure's behaviour during construction, during filling of the reservoir and for a short period of operation. During construction, settlement was approximately proportional to the height of the rockfill, when rock was placed continuously. Creep settlement continued with no increase in fill loading. A high rate of settlement continued for up to 2 months after the top 12 m of rockfill was placed and after the reservoir was filled. The vertical and horizontal deflections of the crest during a period of about 11 months following the commencement of filling the reservoir were (a) maximum vertical = 0.069 m (b) Horizontal downstream maximum = 0.041 m and (c) Horizontal transverse = 0.018 m towards centre from left and 0.008 m toward centre from right. The deflection of the membrane was essentially normal to the face and was a maximum of about 0.013 m at about the lower 0.4 point of the slope. After filling the reservoir; the strains in the facing were in compressive mode, the maximum being 207 $\times 10^{-6}$ in the slope direction and 290 $\times 10^{-6}$ in the transverse direction.

A common assumption in modeling soil-structure interaction by earlier researchers was that the foundation was assumed as rigid which led to ignoring differential ground motions and its effects on the dam. This reduced the complexity of the problem (i.e. the number of additional degrees of freedom for accounting for the interaction), and made it possible to present general results that could be used for different structures. Khalid *et al*. found that for a flexible foundation, the $\sigma_{\theta,y}$ stress in the structure was in the same order as $\sigma_{Rs,y}$ stress, while it was zero for fixed-base models and near zero for very stiff foundations, which reduced significantly the effects of differential ground motion. The results for the transfer-function of the average motion along the base of the structure showed that flexible foundations were not efficient in scattering short wavelengths and thus did not shield the structure from being excited. He discovered that the assumption made in the soil-structure interaction model that the foundation is rigid was valid, μ_F / μ_s should be more than 20 (for ρ_F / ρ_s = 1). If the foundation is more flexible than SSI models with a rigid foundation; the assumption will not model the consequences of differential motion of the ground and may underestimate the stresses in the structure.

FINITE ELEMENT METHOD

The finite element method (FEM) is a powerful tool for numerical procedures in analyzing structures and continua. Problems involving long bodies where geometry and loading do not significantly vary in the longitudinal direction are referred to as cases of plane strain. Finite element analysis was used to study the behaviour of rockfill and predict strains in various portions of the rockfill. The results obtained were promising and the method could be broadly used in future.

The isoparametric formulation makes it possible to generate elements that are non-rectangular and have curved sides. In formulating isoparametric elements, natural co-ordinate systems must be used f (ζ, η). The displacements are expressed in terms of natural co-ordinates, but must be differentiated with respect to global co-ordinates x, y and z.

Six-noded isoparametric elements are also known as incremental elements, wherein the displacement variations in ζ and η directions are different. In the case of CFRD, the

isoparametric elements become slender due to the minimal thickness of the face concrete slab. In quadrilateral element derivations we will need the Jacobian two-dimensional transformations that connect the differentials of $\{x,y\}$ to those of $\{\xi,\eta\}$. From the chain of partial differentiation, derivatives of displacements, u with respect to ξ and η may be expressed in matrix form as:

$$\begin{Bmatrix} \frac{\partial u}{\partial \xi} \\ \frac{\partial u}{\partial \eta} \end{Bmatrix} = \begin{bmatrix} \frac{\partial x}{\partial \xi} & \frac{\partial y}{\partial \xi} \\ \frac{\partial x}{\partial \eta} & \frac{\partial y}{\partial \eta} \end{bmatrix} \begin{Bmatrix} \frac{\partial u}{\partial x} \\ \frac{\partial u}{\partial y} \end{Bmatrix} = [J_c] \begin{Bmatrix} \frac{\partial u}{\partial x} \\ \frac{\partial u}{\partial y} \end{Bmatrix} \quad (1)$$

where, $[J]$ = Jacobian matrix of (x,y) with respect to $\{\xi,\eta\}$.

The rockfill embankment in CFRD is represented by eight-noded isoparametric elements or in CFRD analysis known as parabolic elements. These elements give quadratic variation of strain. The trapezoidal element containing eight nodes can give solutions for eight unknowns. The stiffness matrix is the summation of the quantities at nine integration points (Gaussian points). Here, the stiffness matrix in local co-ordinates is written as:

$$[K] = \int_{-1}^{+1}\int_{-1}^{+1} [B]^T [D][B] * t * |J| \; d\xi \; d\eta \quad (2)$$

$$|J| = \sum_{i=1}^{8} \frac{\partial N_i}{\partial \xi} x_i * \sum_{i=1}^{8} \frac{\partial N_i}{\partial \eta} y_i \quad - \quad \sum_{i=1}^{8} \frac{\partial N_i}{\partial \xi} y_i * \sum_{i=1}^{8} \frac{\partial N_i}{\partial \eta} x_i \quad (3)$$

where, $[K]$ = stiffness matrix; $[B_j]$ = strain-displacement matrix; $[D_j]$ = elasticity matrix; $|J|$ = determinant of $[J]$; t = thickness of element; N_i = shape function at i.

In general, the CFRD dam is built on the soil. Modulus of elasticity of soil (E_{soil}) and concrete (C_{con}) are totally different. Thus it needs a surface between these two elements which is known as 'Interface'. Two parameters have been introduced in the interface element, which are K_{ss}, denoting the shear stiffness and K_{nn} which is the normal differential displacements. The stiffness matrix of the interface element can be written as:

$$[K] = \int [B_j]^T [D_j][B_j] \, ds \quad (4)$$

$$[D] = \begin{bmatrix} K_{ss} & 0 \\ 0 & K_{nn} \end{bmatrix} \quad (5)$$

where, $[K]$ = stiffness matrix; $[B_j]$ = strain-displacement matrix at joint; $[D_j]$= elasticity matrix for the joint; K_{ss} = shear stiffness; K_{nn} = normal differential displacements; ds = the small length of the joint.

Development of infinite elements has helped in proper physical modeling of the far field behaviour and also reduction in the number of elements and also the computational cost. There are two types of infinite elements, namely mapped type and decay type. The mapped type is the most commonly used infinite element. Improved infinite element is based on mapping for modeling of unbounded domain problems. By mapping of $-1 \le \xi \ge +1$, the following expression will be obtained;

$$x = N_0(\xi) x_0 + N_2(\xi) x_2 \quad (6)$$

where, $N_0(\xi) = \frac{\xi}{1-\xi}$, $N_2(\xi) = 1 + \frac{\xi}{1-\xi}$

All the equations above are taken from Zienkiewicz (1979).

BAKUN HYDROELECTRIC DAM

The Bakun hydroelectric power dam is located at the Balui River in Sarawak, Malaysia. Costing approximately RM5.8 billion, the Bakun Dam will be 205 meters high with an approximate crest length of 748.85 m and fill volume of 17 000 000 m^3, once completed. The dam face is essentially a slab of concrete placed against rockfill on the upstream slope that extends from the dam crest to the plinth. Excavation of earth and soil was carried out before the plinth was constructed from concrete. A 7.5 m high 'L' type concrete parapet wall at the upstream of the crest serves as an access road with a dam slope of 1 V:1.4 H at the upstream and 1 V:1.3 H at the downstream. The dam consists of different zones as shown in Figure 1 and Table 1.

MODELLING OF BAKUN CFRD

This dam was modeled as a two-dimensional structure. It was divided into layers and each layer was discreted into elements, comprising of nodes depending on the types of element. The geometry of the dam and the material properties in each section of the dam were designed based on actual data. Each element was discretized according to the respective layer and fitted according to the type of material in the respective section of the dam model. For soil-structure interaction problems, the layer between main dam and concrete face was based on the assumption that no slip occured between the structures and the soil or there was no possibility for shear stresses to develop (interface was perfectly smooth). Two types of dam foundation were considered; namely rigid foundation and flexible foundation as shown in Figure 2.

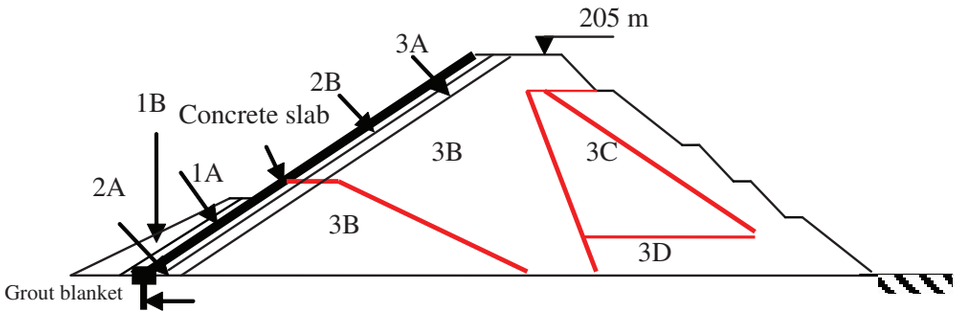

Figure 1. Different zones in Bakun Dam.

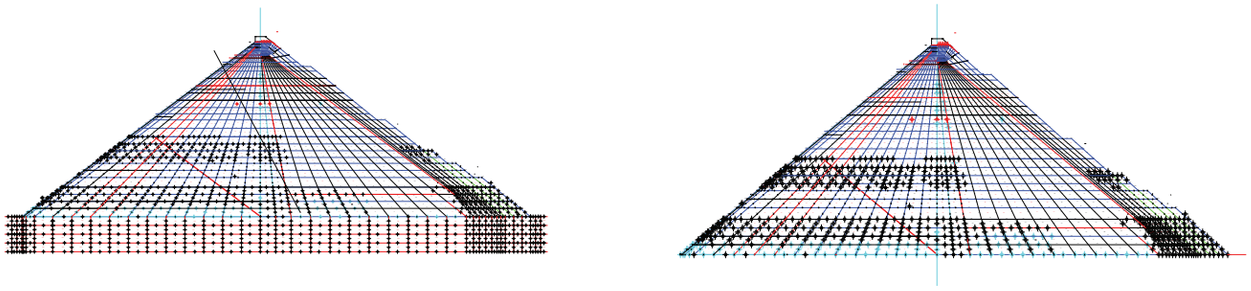

Flexible foundation
(a)

Rigid foundation
(b)

Figure 2. Finite element meshes.

Table 1. Different zones for Main Bakun Dam.

Zone	Designations
Concrete slab	Having a variable thickness reducing with the height, based on formula 0.3+0.003H.
Zone 1A & 1B	Both zones as supporting zones for the upstream, over the lower deck of the perimeter joint.
Zone 2A	A well compacted processed fine filter zone (processed fresh Greywacke). This zone also has a special well graded cushion material.
Zone 2B	Has well graded cushion material selected from fresh greywacke, with a maximum size of 100 mm, this zone is immediately behind the face slab.
Zone 3A	A transition material placed adjacent to zone 2B with maximum size of 300 mm and minimum size of 5 mm.
Zone 3B	The upstream zone forming approximately 50% – 60% of the embankment including the integrated cofferdam. Consist of slightly weathered rock to fresh greywacke.
Zone 3C	A zone within the downstream placed and compacted in layers about 1m thick. It consists of 70% fresh greywacke with 30% mudstone. Maximum size 1200 mm to 5 mm.
Zone 3D	This zone is placed and compacted in layers up to 2 meters thick and dosed to downstream face of the dam to serve as slope protection, also used within the valley bottom to serve a high-capacity under drain. It consist of coarse slightly weathered to fresh greywacke rockfill materials with maximum size 1500 mm.

For the first case, the dam was designed on a fixed base or rigid foundation. The dam was divided into eight zones and then further divided into 28 layers. Each layer was discreted into 936 elements to give a total of 2870 nodes. There were three types of isoparametric elements used in this case; namely eight noded isoparametric elements, six noded isoparametric elements, and an interface isoparametric element. In this case, the boundary condition was fixed at the base of the dam. For the latter case, the model of the main dam was the same as the former case with the addition of foundation layers at the bottom of the main dam. The foundation was divided into four layers and each layer had infinite elements on both sides. The addition to the four layers of foundation gave the increment of 170 elements and 508 nodes to give a sum of 1103 elements and 3378 nodes. The dam which was divided into 32 layers was assumed to be fixed at 40 m below the foundation level.

The finite element program which was written for linear analysis was modified to incorporate material non-linearity, sequential construction of the dam for non-linear analysis and incremental reservoir filling. In the case of geotechnical problems like the height of the Bakun Dam, the non-linearity arose from the stress dependence of the stress-strain material parameters. The isotropic hyperbolic model which was implemented in this study was able to capture the non-linear behaviour and pressure-dependency effects. It also generated the parameter of E_t at each level of loading, which included constitutive parameters according to E-B parameters such as K, n, R_f, ϕ, $\Delta\phi$, K_b, K_{ur}, m as listed in Table 2.

The Birth, Dead and Ghost element techniques which were used by Norzaie (1999) were used in the finite element program to simulate the sequence of construction of the dam and each layer was loaded to signify the particular stage of construction. At the end of Bakun Dam construction, it was planned to impound water after the completion of the dam body and in this analysis the reservoir was considered to be filled in a single stage. Water loading was applied normal to the upstream face.

ANALYSIS AND RESULTS

Non-linear Analysis during the Sequence of Construction

Water load was imposed on any sloping surface of the dam. The results of the hydrostatic pressure acted perpendicular to the upstream face as a force consisting of horizontal and vertical components. In simple mathematical concepts, a resultant force, W, which acts on an inclined surface can be resolved into horizontal and vertical components as shown in Figure 3.

Triangular loading distributed on the concrete face of the elements located at the upstream face applied simulated stress to the reservoir thrust. The analysis of Bakun Dam at the end of filling the reservoir had the same general objectives as at the construction period. However, the main reason in carrying out such analysis was to verify the capability of the model in predicting the behaviour of this type of dam during filling the reservoir, whereby the unloaded stress paths and principal stress axis rotations play an important role in the general behaviour of the dam.

The study of both contours in Figure 6 indicates that at any horizontal elevation, the maximum horizontal displacement occurs at the upstream face and gradually decreases for points in a downstream direction. The maximum horizontal displacement occurrs on the upstream face at about mid-height. The maximum horizontal displacement for the flexible foundation was 1.2 m and it was 0.3 m for the rigid foundation. The difference of 0.9 m was because large dams like the Bakun Dam have a larger effect on horizontal water thrust compared with the main dam from the reservoir.

The upstream rockfill embankment was seen to settle downwards upon application of reservoir load. The maximum vertical displacement with foundation case occurred at the upstream side close to the centreline of the dam near the foundation level. It was seen that at any

Table 2. Parameters for Duncan's E-B Model.

Material	γ	K	n	ϕ	$\Delta\phi^o$	m	Rf	Kb	K_{ur}
Cushion material	22.8	400	0.35	50.6	7	0.22	0.78	520	800
Transition material 3A	22.5	780	0.30	52.5	8	0.25	0.77	525	1500
Rockfill 3B	21.3	850	0.30	52.5	10	0.20	0.77	550	1700
Rockfill 3C	20.6	700	0.35	48.0	7	0.10	0.73	300	1500
Rockfill 3D	20.5	760	0.35	52.5	10	0.18	0.76	460	1500
Foundation	19.0	300	0.45	38.0	2	0	0.8	150	600

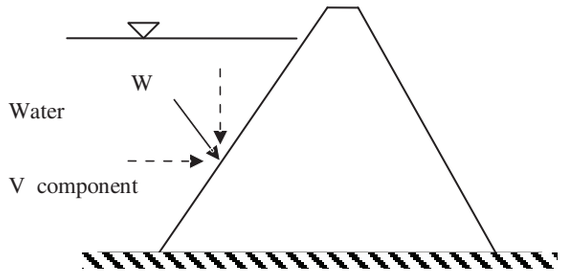

Figure 3. Face sealing 'concrete faced' due to water head.

horizontal elevation, the vertical displacement was higher at the upstream face and gradually reduced towards points on the downstream side. At the elevation below the foundation level, the smaller interval gave a higher difference of stresses, as the contours were closer apart compared to the main rockfill. The maximum value of horizontal stress for the flexible foundation type was 3.4 m.

For the rigid foundation type, the maximum value of stress was produced at the centerline of the dam. Compared to the vertical displacement at the end of construction which is illustrated in Figure 5, the maximum value of vertical displacement at the end of reservoir fillings increased by 0.1 m (Figure 5 gave 1.1 m and Figure 4 gave 1.2 m). The vertical and horizontal displacements were considerably affected by the water thrust exerted onto the upstream of the dam.

Contours of horizontal, vertical, shear, major and minor principal stress for full reservoir conditions are shown in Figures 7 to 9. These stresses also included the stresses at the end of construction which were fed into the computer as on initial condition, adding to the hydrostatic pressure to enable the analysis for a full reservoir condition.

The comparison of horizontal and vertical stress contours for a full reservoir condition (Figures 7 and 8) with those of end of construction (Figure 10) introduced the effect of application of reservoir load on the horizontal and vertical stresses in the rockfill. It was seen that with an application of reservoir water load, both the horizontal and vertical were increased considerably in the upstream at the centre of the dam cross-section.

In comparison between Figure 8 and Figure 10 using a flexible foundation, the maximum value of horizontal stress was higher, i.e. 1000 kN/m^2 and 1125 kN/m^2 at the end of construction and at the end of filling the reservoir respectively, occurring at the foundation level. Even though both analyses did not produce much difference in the magnitude of maximum horizontal stress occurring closer to the downstream, there was an increase of values at the upstream side. This was due to the extra force exerted by the water thrust from the reservoir to the upstream face. In the case of rigid foundation, the maximum values of horizontal stresses were 2000 kN/m^2 and 1875 kN/m^2 for filling the reservoir and end of construction, respectively.

Figure 10 gives the end of construction analysis, yielding maximum values of vertical stresses of 3000 kN/m^2 and 3375 kN/m^2 for with and without foundation cases respectively, at the foundation layer. On the other hand, Figure 7 yielded 3500 kN/m^2 for both cases. Comparisons of both contours at the end of construction and filling the reservoir looked much similar and no major changes were produced, as in the contours of horizontal stresses.

For the 'with foundation' case, there was an obvious effect of filling the reservoir compared to the rigid foundation case where the effects of filling the reservoir at the downstream were very minimal. In the case of CFRD, a buoyancy effect was absent and the water load was applied on the upstream sloping face resulting in a considerable increase in both the horizontal and vertical stresses in the upstream portion of the rockfill embankment section.

A comparison of shear stresses for a full reservoir condition with the analysis at the end of construction shown in Figures 9 and 10 indicated an application of water load. The zero shear value shifted from the centre of the dam at end of construction to the region at the upstream side. The shear in the downstream portion was further increased (+600 kN/m^2 with foundation and +475 kN/m^2 without foundation) compared to +400 kN/m^2 at the end of construction while the shear in the upstream portion was considerably reduced (–150 kN/m^2 and –200 kN/m^2, respectively) compared to –400 kN/m^2 at the end of construction. This was quite understandable because at the end of construction the rockfill had a tendency to spread out from the centre towards the upstream and downstream face, while the water load tried to push the whole dam in a downstream direction resulting in more shear stress. However, there was an increase of maximum stress value which occurred at the small region at the heel of the upstream for both cases.

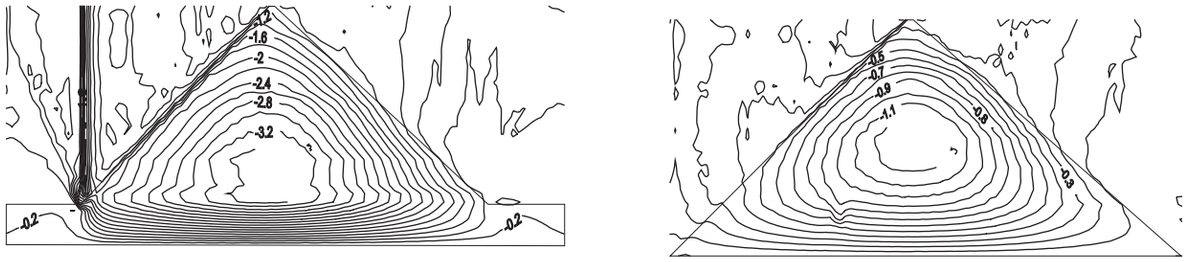

(a) (b)

Figure 4. Contours for vertical displacement with reservoir operation for with and without (rigid) foundation for non-linear analysis.

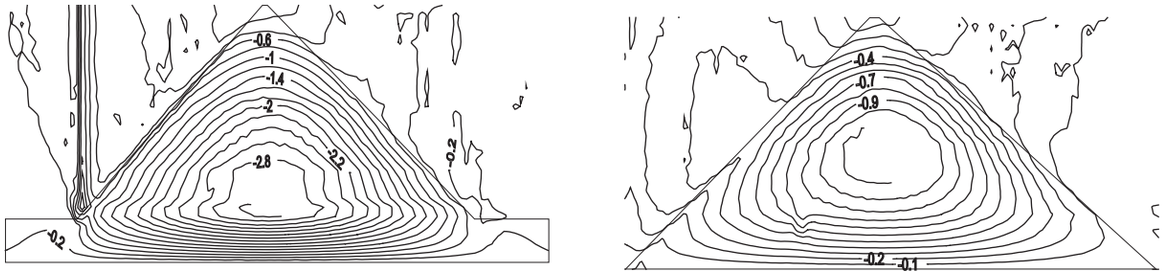

(a) (b)

Figure 5. Contours for vertical displacement at the end of construction for with and without (rigid) foundation non-linear analysis.

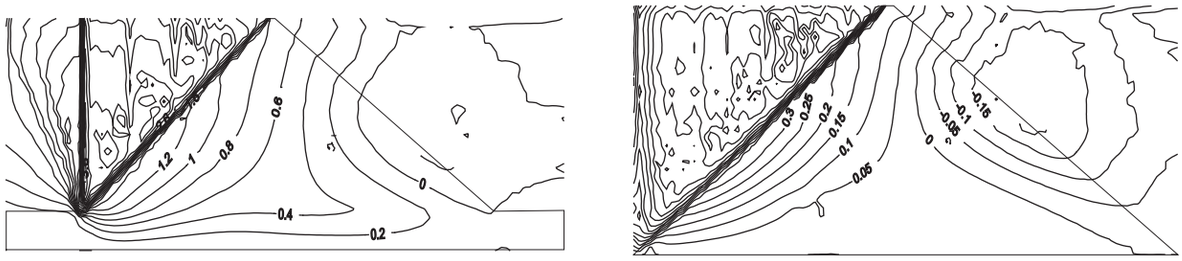

(a) (b)

Figure 6. Contours for horizontal displacement with reservoir operation for with and without (rigid) foundation for non-linear analysis.

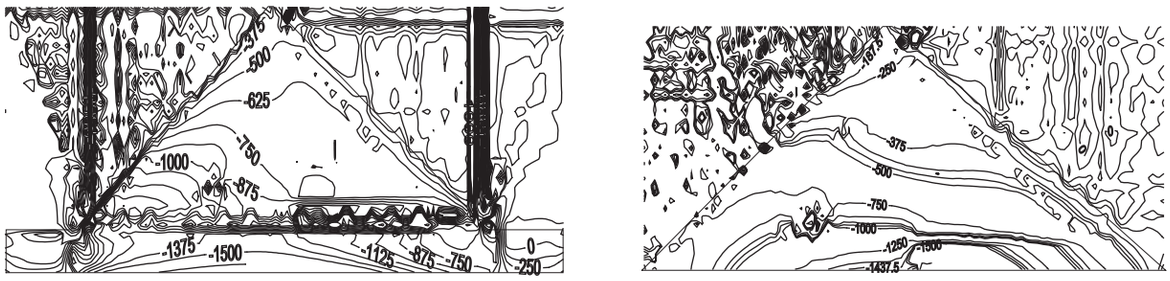

(a) (b)

Figure 7. Contours of normal stress, σ_x at reservoir operations for with and without foundation for non-linear analysis.

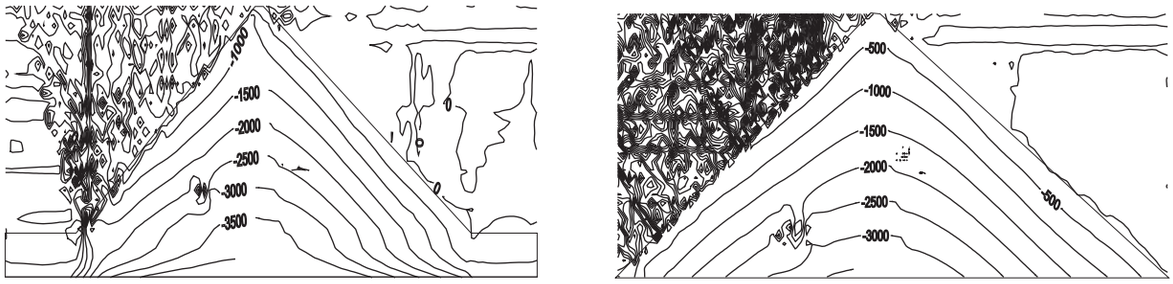

(a) (b)

Figure 8. Contours of normal stress, σ_y at reservoir operations for with and without foundation for non-linear analysis.

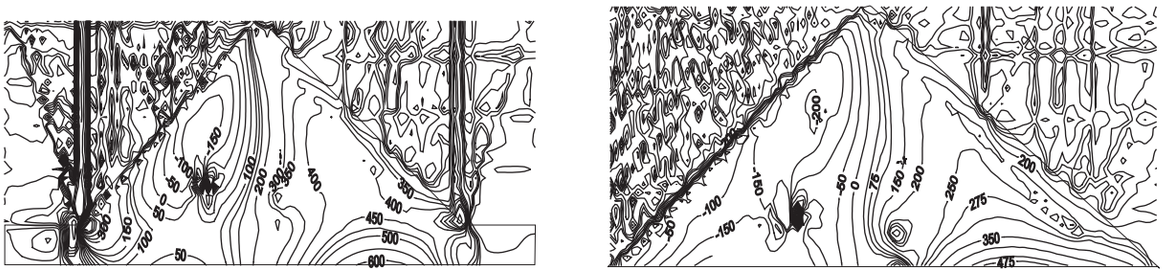

(a) (b)

Figure 9. Contours of shear stress, τ_{xy} at reservoir operations for with and without foundation for non-linear analysis.

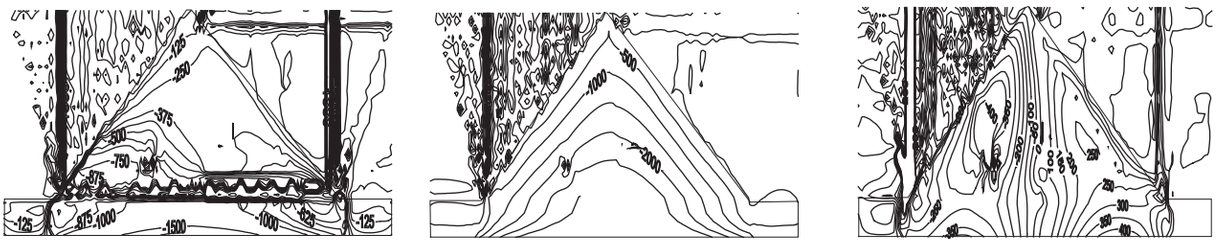

(a) (b) (c)

Figure 10. Contours of normal and shear stresses, σ_x, σ_y and τ_{xy} at the end of construction for with foundation for non-linear analysis.

As proposed by Singh and Varshney (1995), a simple way of calculating the factor of safety due to water loading was used as shown in Table 3 which represented a very high factor of safety against sliding, meaning that there was no possibility of sliding between the concrete slab and the body of the dam. The details of the calculation are shown in Table 3.

CONCLUDING REMARKS

The 205 m high Bakun CFRD that is currently under construction in Sarawak was modeled and discretized using finite element analysis. Two cases, with (flexible) foundation and without (rigid) foundation were analyzed using a few elements; namely interface elements (between face slab and main rockfill), six noded isoparametric elements, eight noded isoparametric elements (main rockfill), and infinite element (for element in foundation layers only).

The FEA program simulation technique using Birth-Dead-Ghost sequence was easily understood since simulation in the stages of construction considered each layer which comprised of several elements. The model was idealized for plane strain problems and types of loadings were simulated as non-linear analysis. By using the latest hyperbolic non-linear elastic model version (Duncan-Chang 1984), two cases of loading were considered and the case at the end of reservoir impoundment (the values, i.e. displacement, strains and stresses) obtained at the end of construction were stored in the program. Effects on hydrostatic pressure imposed at the upstream of Bakun CFRD were discussed. Contours at the end of construction and end of reservoir fillings were also discussed.

Based on the analyses that was carried out, the following conclusions were drawn:

(i) There was an increase in vertical displacement with a percentage of 11.8% and 8.3% for 'with foundation', and 'without foundation', respectively compared to the end of construction before the water impoundments.

(ii) Horizontal displacement increased for both cases which showed an increment of 0.8 m and 0.1 m for the case of 'with foundation' and 'without foundation', respectively. The maximum value of horizontal displacement occurred near the upstream slope.

(iii) By comparison with the end of construction analysis, there was an increase of σ_x and σ_y during filling the reservoir due to water thrust exerted on the main dam slope. There was a slight increment of the σ_x value along the upstream of the dam and a larger increment in the σ_y value towards to the base of the dam.

(iv) The maximum value of the normal stresses, σ_x occurred at the 1/3 of the Bakun CFRD height from the heel near the upstream slope for both 'with foundation' and 'without foundation'

Table 3. Calculating safety factor as proposed by Singh and Varshney (1995).

Description	Forces (kN)
Water pressure force ($P_w = \gamma_w \times h^2 / 2$)	194242.91
Horizontal component of water pressure ($P_w \sin \theta$)	112901.18
Vertical component of water pressure, ($P_w \cos \theta$)	158062.11
Weight of rockfill of the dam	1287671
Total vertical forces	158062.11 + 1287671 = 1445733.11
Ratio of vertical forces to horizontal forces	1445733.11 / 112901.18 = 8 >1

cases. For σ_y, due to the 'overburden' phenomenon of the self-weight of the dam, the maximum stresses took place at the middle of the base of the dam for both cases.

(v) The behaviour of major and minor principal stresses were the same with slight increases in the maximum and minimum value of vertical and horizontal normal stresses.

(vi) While normal stresses, σ_x and σ_y increased compared to the end of construction, the major and minor principal stresses increased as well. Through observation at its contours, the 'with foundation' case had a more significant increase compared to the 'without foundation' case. Similarly, minor principal stresses experienced an increase along the upstream at the upstream slope face and substantially increased at the middle of the dam, as did the vertical stresses. For rigid foundation, minor principal stresses yielded a smaller value of maximum horizontal stresses but there was no difference between major principal stress and vertical stress.

Date of submission: October 2007
Date of acceptance: December 2008

REFERENCES

Alberro, J 1972, 'Stress-strain analysis of El Infiernillo Dam', in *Proceedings of the ASCE Speciality Conference on Performance of Earth and Earth Retaining Structures*, Purdue University, Indianna, ASCE, New York, vol. 1 (Part 1) pp. 837–852.

Chen, C, Wang, D & Tan, J 2000, 'Emulating analysis for Shuibuya Concrete Faced Rockfill Dam', in *20th Congress of ICOLD, International Symposium on Concrete Faced, China*.

Clough, RW & Woodward, RJ 1967, 'Analysis of embankment stresses and deformations', *Journal of the Soil Mechanics and Foundations Division*, A.S.C.E, vol. 93 (SM4), pp 529–549.

Varma, CVJ 1992, *Rockfill dams — finite element analysis to determine stresses and deformations in membrane type rockfill dam*, Central Board of Irrigation and Power, New Delhi, pp. 110–116.

Duncan, JM *et al*. 1980, *Strength stress-strain and bulk modulus parameters for finite element analyses of stresses and movements in soil masses*, Report No. UCB/GT/80-01, Department of Civil Engineering, University of California, Berkeley.

Duncan, JM, Seed, W & Ozawa, Y 1984, *FEADA84*: A *computer program for finite element analysis of dams*, *Department of Civil Engineering*, Virginia Polytechnic Institute and State University, Blackburg, pp. 30–63.

Hinton, E & Owen, DRJ 1977, *Finite element programming*, Academies Press, London.

Khalid, S *et al*. 1990, 'Nonlinear analysis of concrete face rockfill dam', *Journal of Geotechnical Engineering*, vol. 116, no. 5, pp. 822–837.

Nobari, ES & Duncan, JM 1972a, *Effect of reservoir filling on stresses and movements in earth and rockfill dams*, Report TE-72-1, University of California, Department of Civil Engineering.

Nobari, ES & Duncan, JM 1972b, 'Movements in dams due to reservoir filling', in *Proceedings, ASCE Speciality Conference on Performance of Earth and Earth Retaining Structures*, Purdue University, Indiana, ASEC, New York, vol. 1 (Part 1), pp. 797–815.

Noorzaie, J, Golinavaz, H & Pakbas, MC 1999, 'Nonlinear analysis of earth and rockfill dams considering the sequence of construction', *Journal Computational Mechanics for the Next Millennium Solid Mechanics and Fluid Mechanics*, vol. 1.

Singh, B & Varshney, RS 1995, *Engineering for embankment dams*, Balkema, USA.

Zienkiewicz, OC 1979, Finite element method, 3rd edn, Tata McGraw-Hill Publishing Limited, New Delhi.

Xingzheng W, Xin, J & Tian, H 2002, *Three dimensional stress and displacement analysis of Yutiao Concrete Faced Rockfill Dam*, Key project of Electric Power Corporation, China.

ASM Sci. J., **3(1)**, 27–30

SOA-based Multi-wavelength Source

S.W. Harun[1*], A.H. Sulaiman[2] and H. Ahmad[2]

We demonstrate a multi-wavelength light source using a semiconductor optical amplifier (SOA) in conjunction with an array waveguide grating (AWG). The experimental results showed more than 20 channels with a wavelength separation of 0.8 nm and an optical signal-to-noise ratio of more than 10 dB under room temperature. The channels operated at the wavelength region from 1530.4 nm to 1548.6 nm, which corresponded to AWG filtering wavelengths with SOA drive current of 350 mA. The proposed light source had the advantages of a simple and compact structure, multi-wavelength operation and the system could be upgraded to generate more wavelengths.

Key words: multi-wavelength light source; SOA; AWG; multi-wavelength; optical signal-to-noise ratio

Multi-wavelength sources are becoming an increasingly attractive solution in fulfilling the role of a laser source for a wide range of applications that include optical fibre sensors and dense wavelength division multiplexing (DWDM) communications applications. There are many methods of generating simultaneous multiwavelength output such as Brillouin/erbium fibre lasers (BEFLs) (Park *et al*. 2005; Harun *et al*. 2007) and multiwavelength erbium-doped fibre lasers (MWEDFL) (Chow *et al*. 1996; Yamashita & Hotate 1996; Graydon *et al*. 1996; Sun, Qin & Huang 2000; Dong *et al*. 2000). However, the BEFLs have a limited channel number and a fixed channel spacing of about 0.08 nm. Stable multiwavelength sources based on erbium-doped fibres (EDFs) are difficult to obtain due to the homogeneous broadening of laser modes. MWEDFLs were reported either by immersing the EDF in liquid nitrogen (Yamashita & Hotate 1996) or using specially designed twin-core EDF (Graydon *et al*. 1996). Recently, semiconductor optical amplifiers (SOAs) have received much attention for signal amplification in optical networks (Kelly *et al*. 2004). Compared to conventional optical amplifiers, SOAs have many advantages such as compactness, lightness, lower power consumption as well as being mass producible. Additionally, the SOA is a gain medium with a dominant inhomogeneous broadening property and thus can generate multiple lasing wavelengths at room temperature (Harun *et al*. 2008).

In this short communication, a new and simple configuration of multi-wavelength light source was proposed and demonstrated using a SOA and array waveguide grating (AWG). The multi-wavelength source had several important advantages such as stable multi-wavelength operation at room temperature, a broad workable wavelength band and no need for optical pump lasers. The proposed multi-wavelength source used an SOA and AWG which were built together in one chip. This made the device much more compact compared with the conventional multi-wavelength source. The compact device was suitable for use in field applications.

EXPERIMENTAL SET-UP

Figure 1 shows the configuration of the proposed multi-wavelength source using a SOA and an AWG. The SOA was driven by various bias current settings and the temperature of the SOA was set at 30ºC using a laser diode controller. The current flow through the SOA generated the spontaneous emission of photons from the semiconductor gain medium due to the recombination of electron-hole pairs. The generated amplified spontaneous emission (ASE) signal of the SOA was then filtered by the AWG, allowing only the ASE signal spectrum that fell within the filter pass-band to pass through the AWG, to generate a simultaneous multi-wavelength output light. An optical circulator was used to route the ASE from the SOA into the AWG and the filtered light from the AWG into an optical spectrum analyzer (OSA).

The SOA was made from an InGaAsP-InP ridge waveguide with facets angled at 10º and was antireflection coated. It had a saturated output power of 10 dBm, a maximum bias current of 400 mA and had a centre operating wavelength of 1534 nm with a spectral width of 40 nm. The SOA had a small signal gain of 20 dB with a gain saturation current of 160 mA. The noise figure of the SOA averaged 10 dB for the low signal and 7 dB for the high signal. The

[1] Department of Electrical Engineering, Faculty of Engineering, University of Malaya 50603 Kuala Lumpur, Malaysia
[2] Photonics Laboratory, Department of Physics, University of Malaya, 50603 Kuala Lumpur, Malaysia
[*] Corresponding author (e-mail: swharun@um.edu.my)

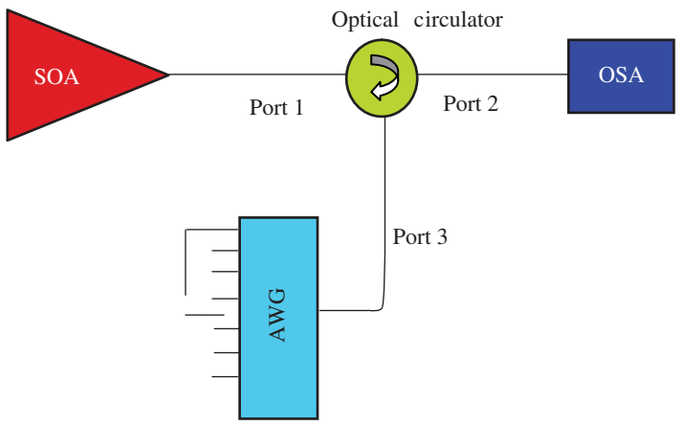

Figure 1. Configuration for the multi-wavelength source.

SOA would manifest a strong resonant when it was biased at a high current which generated a ripple in an output ASE spectrum. The AWG used in this experiment was a 24 channel AWG with a channel spacing of 100 GHz or 0.8 nm. Port 1 of the AWG began at 1530.4 nm and the last port, port 24 was at 1548.6 nm. Two output ports of the AWG were connected together in the experiment. The insertion loss of AWG varied from 2.2 to 3.3 dB within ports 1 to 24.

RESULTS AND DISCUSSION

Figure 2 shows the ASE spectrum of the SOA when the bias current was set at 350 mA. The ASE had a power of above –30 dBm within the wavelength range of 1510 to 1550 nm. The ASE power peaked at around 1530 nm region with two lasing wavelengths due to the back reflection in the SOA cavity. A power ripple was also observed in the spectrum which was due to a strong resonant in the laser cavity. The output spectrum of the multi-wavelength source is shown in Figure 3, showing more than 20 wavelengths within 19 nm bandwidth of C-band with most of the peak power above –45 dBm and channel spacing of 0.8 nm. The SOA's bias current and temperature was set at 350 mW and 30 degree Celcius, respectively. In the experiment, two output ports of the AWG were connected together, as shown in Figure 1. All three combinations of port connection showed almost similar output as shown in Figure 3. The laser wavelength spacing was controlled by the AWG spacing which was determined by phase difference between the light paths. The ASE light from the SOA was sliced into multiple wavelength channels by AWG through inference effects. Due to the phase difference among the AWG ports when the two propagating beams met at the coupling region, it interfered constructively and destructively, to generate a multi-wavelength light source. The channel spacing of the light source was determined by the amount of phase difference which was dependent on the AWG design. The gain characteristics of the SOA and insertion loss variation among the channels of the AWG also contributed to the variation of peak power. Figure 3 also shows that a optical signal-to-noise ratio (OSNR) of over 10 dB was obtained for the most of the channels under room temperature. One or two channels of the output spectrum was missing due to some defect inside the AWG, as shown in Figure 3.

The results after monitoring the output spectrum of Figure 3 for a long time indicated that the wavelength spacing kept remains constant with only slight power fluctuations among the output channels. This behaviour could be attributed to the clamped gain in the SOA-based laser through lasing line oscillation (Tiemmeijer *et al*. 1995). From the experiment, it could be seen that the multi-wavelength source was able to generate a stable and narrow spaced channel for DWDM or sensor applications. The multi-wavelength source design was considerably compact due to its use of the SOA and AWG. The system could also be upgraded to more lasing wavelengths by simply upgrading a number of channels of the AWG.

CONCLUSION

A compact multi-wavelength light source was demonstrated using an SOA and an AWG. The source generated more than 20 channels within 1530.4 nm to 1548.6 nm wavelengths at 1530.7 nm, 1531.5 nm, 1632.3 nm and 1533.1 nm. At the SOA drive current of 350 mA, most of the channel wavelengths had a peak power above –45 dBm and OSNR above 10 dB. The laser showed stable multi-wavelength channels with a wavelength separation

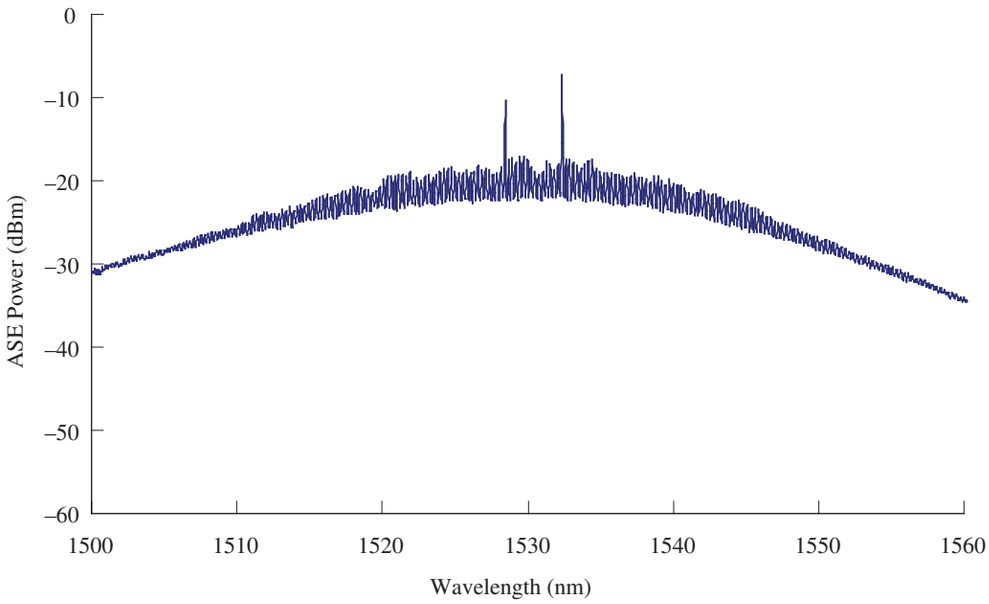

Figure 2. ASE spectrum of the SOA at bias current of 350 mA.

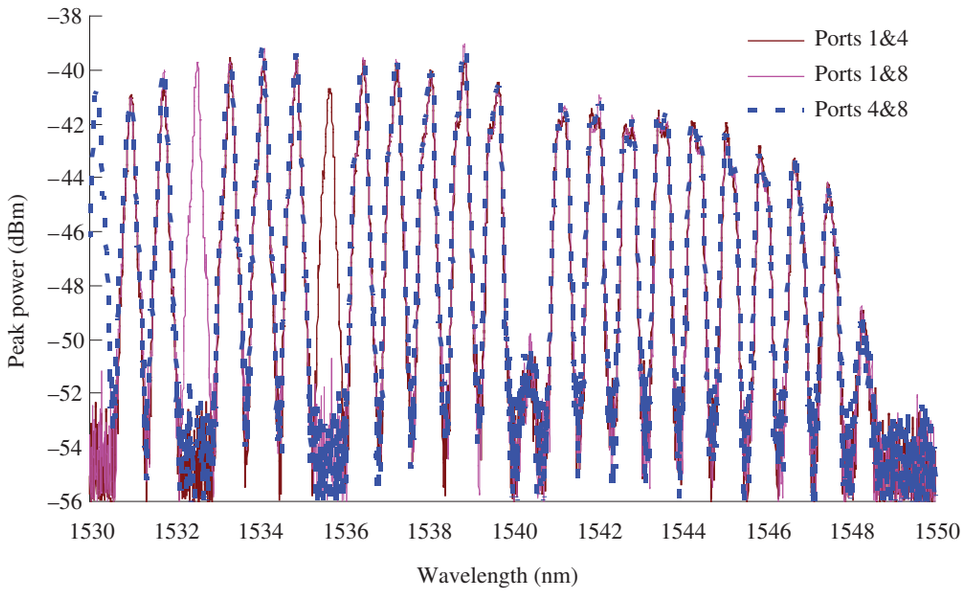

Figure 3. Output spectra of the multi-wavelength light source at different output ports combination.

of 0.8 nm. The proposed source had the advantage of stable multi-wavelength outputs at room temperature with simple and compact structure. It had many potential applications in DWDM and sensor applications.

Date of submission: November 2007
Date of acceptance: December 2008

REFERENCES

Chow, J *et al.* 1996, 'Multiwavelength generation in an erbium-doped fiber laser using in fiber comb filters', *IEEE Photon. Technol. Lett*., vol. 8, pp. 60–62.

Dong, XP *et al*. 2000, 'Multiwavelength erbium-doped fiber laser based on a high-birefringence fiber loop mirror', *Electron. Lett*., vol. 36, pp. 1609–1610.

Graydon, O *et al*. 1996, 'Triple-frequency operation of an Er-doped twincore fiber loop laser', *IEEE Photon. Technol. Lett*., vol. 8, pp. 63–65.

Harun, SW *et al.* 2008, 'Multi-wavelength source based on SOA and EDFA in a ring cavity resonator,' *Optoelectronics and Advanced Materials — Rapid Communications*, vol. 2, pp. 317–319.

Harun, SW *et al*. 2007, 'Self-excited Brillouin-erbium fiber laser for DWDM applications', *Optics and Laser Technology*, vol. 39, no. 1, pp. 94–97.

Kelly, AE *et al*. 2004, 'High performance semiconductor optical amplifiers', in *Optical Fiber Communication Conference*, vol. 2, pp. 3.

Park, KD *et al*. 2000, '53-line multi-wavelength generation in Brillouin/erbium fiber laser with enhanced Stokes feedback coupling', *Optic. Fiber Commun*., (OFC2000), Baltimore, paper ThA4.

Sun, J, Qiu, J & Huang, D 2000, 'Multiwavelength erbium-doped fiber lasers exploiting polarization hole burning', *Opt. Commun.*, vol. 182, pp. 193–197.

Tiemmeijer, LF *et al*. 1995, 'Reduced intermodulation distortion in 1300 nm gain-clamped MQW laser amplifiers', *IEEE Photon Technol. Lett*., vol. 7, pp. 284–286.

Yamashita, S & Hotate, K 1996, 'Multiwavelength erbium-doped fibre laser using intracavity etalon and cooled by liquid nitrogen', *Electron. Lett.*, vol. 32, pp. 1298–1299.

ASM Sci. J., **3(1)**, 31–37

Pattern-pulsed MfVEP Waveform of Age-related Macular Degeneration Patients

Y. Rosli[1*], T.L. Maddess[2], A.C. James[2] and X.L. Goh[2]

Responses were recorded from normal healthy subjects and age-related macular degeneration (AMD) patients and evaluated, using a new variant of mfVEP. Subjects information was recorded using 64 EEG channels with a computer-based acquisition system. The stimulus layout was a 84 region cortically-scaled dartboard comprising 12 sectors and seven concentric rings subtending a diameter of 23º, presented dichoptically at 60 Hz. Data from the control and AMD patients were statistically compared when fitted concurrently into the multiple regression analysis. The Pattern-pulse mfVEP technique could distinguish between normal eyes and those with a definite diagnosis of dry and wet AMD when responses from the macula were considered.

Key words: age-related; macular degeneration; pattern-pulsed; mfVEP; EEG channels; waveform; dicoptic stimulus

Age-related macular degeneration (AMD) is a degenerative condition of the central retina (macula). It has a devastating impact as it causes the loss of retinal photoreceptors in the late stages, ultimately leading towards the loss of visual acuity if the foveal region which is responsible for fine vision is damaged (Curcio *et al*. 1996; Owsley *et al*. 2000; Reme *et al*. 2003). It is the most common cause of vision loss in the USA. AMD has been estimated to affect between 0.7% to 1.9% of the population studied in the USA (The Beaver Dam Eye Study; Wisconsin); Netherlands (Rotterdam) and Australia (Blue Mountain; Sydney and Victoria); (Klein *et al*. 1992; Mitchell *et al*. 1995; Vingerling *et al*. 1995; van Newkirk *et al*. 2000). It is stated to be the leading cause of irreversible visual loss for individuals over 50 years of age in Australia (Attebo *et al*. 1996; VanNewkirk *et al*. 2001). Many earlier electro-physiological studies using full-field study stimuli have established abnormalities in AMD patients. In electro-oculogram studies, Walter *et al.* (1999) found an overall decrease in amplitude in their AMD patients and a similar result has been obtained for gaAMD patients (Falsini *et al*. 1999). In mfERG studies, the amplitude was greatest in the fovea and decreases gradually with eccentricity in the control subject (Huang *et al*. 2000), the variability of the response density was greater from the central retina (eccentricity 0º to 9º) compared to from the peripheral retina (13.1º–18.7º) as reported by Verdon & Haegerstrom-Portnoy (1998). A summary of changes in response to various retinal diseases have been summarized in a mfERG study by Hood (2000). The common finding is that, damage to the photoreceptors caused decrease in the amplitude of local mfERG responses compared to normal responses, leading to a decrease in response density.

The present study was carried out to compare the response from normal healthy subjects and AMD patients using a new type of multifocal VEP (mfVEP) recording technique, the pattern-pulse multifocal VEP (James 2003). In mfVEP, the areas of cortex were independently stimulated according to a binary m-sequence governing the contrast of each of many stimuli; therefore the optic pathway conditions could be diagnosed using responses from multiple individual segments of the visual field, allowing topographic visual field deficits to be characterized using measures such as reduced response amplitudes or abnormal latencies. Although AMD affects central vision, peripheral vision may remain unaffected. Having this in mind, the stimulus for mfVEP used in this study encompassed the macula (ring/eccentricity 1–5; see stimulation delivery, below) but it also covered more peripheral retina (ring/eccentricity 6–7; see stimulation delivery, below). Stimuli presented in eccentricities six and seven were thus outside the anatomically defined macula. Since small stimulation techniques like this study is recommended in patients with retinal pathology (Walter *et al*. 2000), one might expect the focal retinal abnormalities in AMD to affect the mfVEP responses from the central retina more that the responses from the peripheral retina.

[1]Department of Biomedical Science, Faculty of Allied Health Sciences, Universiti Kebangsaan Malaysia, Jalan Raja Muda Abdul Aziz, 53300 Kuala Lumpur, Malaysia
[2]Australian Research Centre of Excellence for Visual Sciences, Research School of Biological Sciences, Building 46, Australian National University, Canberra 2602 ACT, Australia
* Corresponding author (e-mail: rosli@rsbs.anu.edu.au)

METHODS AND DATA ACQUISITION

Subjects Selection Criteria

Twenty-six subjects were recruited for the control group with no history of eye diseases, no complaints concerning visual function, best corrected acuity, normal interocular pressure and normal visual field. The age range was 20 to 77 years (mean 39.0 ± 15.8 years) and 11 were females. AMD patients were recruited from patients seen within the past two years at the Canberra Eye Hospital, Australia. Four patients with wet AMD (cvAMD) in either eye or both eyes (mean age 75.0 ± 17.0 years) participated in the study. None of the subjects had systemic diseases or were on medication (e.g. chloroquine) known to affect retinal function. Patients with ocular diseases other then AMD were excluded. All subjects were informed of any potential risks prior to participation and gave written consent. This research was approved by Australian National University Human Research Ethics Committee and adhered to the tenets of the Declaration of Helsinki.

Subject Preparation

A correctly sized head cap with 64 electrode channels was placed over the subjects' head. Electrode holders on the head cap were filled with gel (Signa Gel, Parker), pin-type active electrodes were used and the contact quality was checked by the offset values in the BioSemi acquisition software (Biosemi Ltd, Amsterdam).

Multi-modal Data Acquisition System with Active Electrodes (ActiveView)

The experimental data were simultaneously sampled at 256 Hz per channel and collected using the ActiveTwo BioSemi data acquisition software, ActiveView. The pin type Active Ag-AgCl electrodes mounted on the head cap were connected to the Biosemi 64 channel A/D interface box. The A/D-box digitized each of the 64 sensory signals with 24 bit resolution and the output were sent to the data collection computer. The collected data were buffered and streamed in near real time by data acquisition software (ActiveView, BioSemi).

Stimulus Delivery

The stimuli subtended a diameter of 23º and were presented dichoptically at a 60 Hz frame rate. The stimulus layout was an 84 region cortically-scaled dartboard, with 12 sectors and 7 concentric rings. The increasing eccentricity of the ring centres were 1.6º, 3.0º, 4.8º, 7.1º, 10.2º, 14.3º, and 19.8º permitting approximately similar areas of cortical area V1 to be stimulated by each region, generating results of a similar magnitude across eccentricities. Each recording run lasted for 241.75 s, carried out in four segments of average duration 60.94 s; with 14 505 frames per run. Within each frame, one or more regions could be active 9 (Figure 1). Each 4 × 4 checkerboard pattern was pulsed on for 33 ms with the black checks having a luminance of 1 cd/m^2, and the white checks having a brightness of 180 cd/m^2. When these checkerboards were displayed, 50% of the time they had one or the other check polarity and when no checkerboard was present the monitor was maintained at the mean luminance of 90 cd/m^2. Stimulus markers were output by the stimulus computer's parallel port and recorded in the response file.

Data Analysis

The continuously recorded data file was transferred to a data analysis environment (Matlab; Mathworks, Natick,

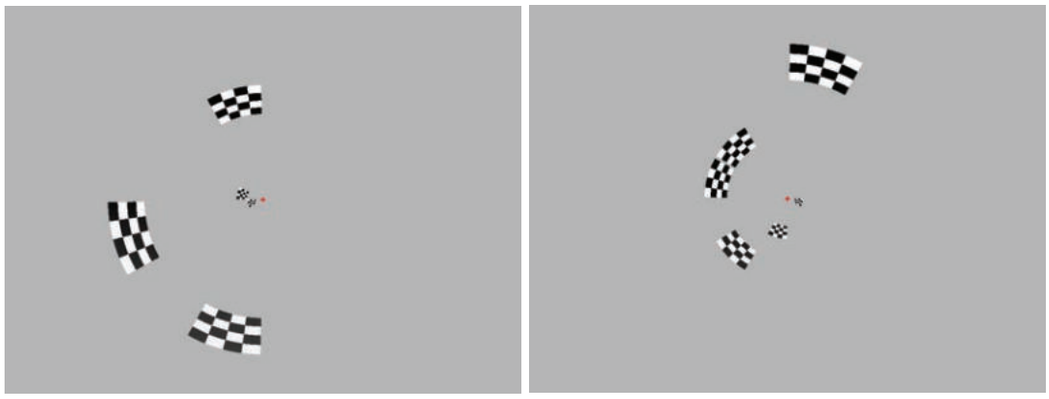

Figure 1. Sample of dichoptic stimulus at frame 708; that is delivered concurrently to the left eye (OD, left panel) and the right eye (OS, right panel).

MA). The set of 64 scalp electrodes was augmented with a zero signal for the reference channel Fpz and the average signal over the resultant set was subtracted from each signal, to give an average-referenced response signal set. Mean responses from all channels over the 84 regions and normal subjects were extracted and these were compared to mean responses collected at channel POz and from the occipital electrodes channels. Regression analysis was later carried out. A rectilinear layout was used to represent these sets of response waveforms obtained from the 64 electrode-array on a scalp plot matching the dartboard stimulus. The layout was indexed vertically by the polar angle above the horizon of the region's center, from –75º to 75º, and horizontally by the eccentricity in the visual fields (the left or the right of the regions center).

RESULTS AND DISCUSSION

The mean responses of the normal control subjects exhibited waveforms at all eccentricities (Figure 2), with slight changes in the amplitude with increasing eccentricity. Among the AMD patients however, the amplitude decrease was dramatic, showing a decrease in response to the inner visual regions, especially in the central eccentricity. Interestingly, not one region showed absence of responses from either OS or OD, although we observed a lag in the waveforms from the OS and OD, or deficits in either waveforms depending on the case. The focal electrophysiological deficits found in AMD were consistent with the loss of rods and cones (Curcio *et al*. 1996) in and around the retinal area of AMD that had been reported before (Verdon & Haegerstrom-Portnoy 1998). We observed very significant ($p<0.000$) amplitude depression in the inner four rings in AMD patients. This concurred with the report by Jurklies *et al*. (2002) who reported that in cvAMD patients the response densities were reduced within the central 5° (in this study, eccentricity 4 was at 4.8°). We deduced that it could be that the reduction seen signified that there had been some form of deterioration on average that had started to take place in these eyes in comparison with the MERG study by Li (2001), who reported the significant abnormality in the foveal amplitude and the foveal latency of MERG in pre AMD or early AMD eyes as well as asymptomatic contralateral eyes. Earlier studies have reported notable pathological changes in patients with AMD with reduced amplitudes indicating there were only a few cells present (Walter *et al.* 1999; Walter *et al*. 2000).

As mentioned, the data from the normal control subjects and the AMD patients were fitted concurrently in the multiple regression analysis model, hence statistical response comparison could be made between the groups with minimum error since the compounding factors

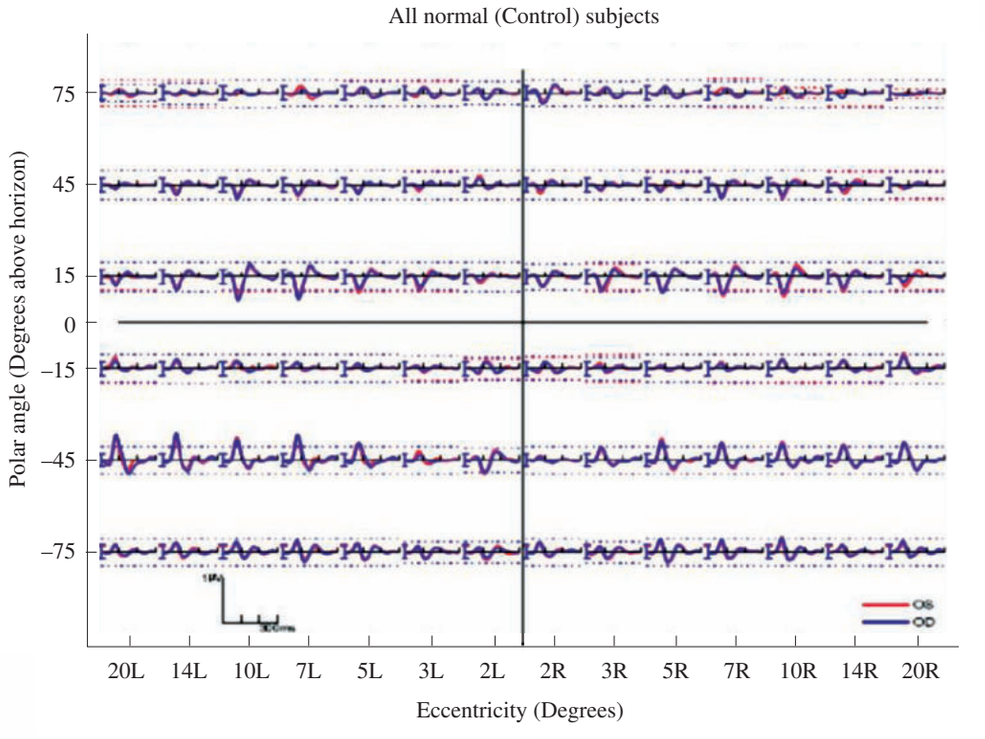

Figure 2. Rectilinear layout of the response set of the grand means from all the 26 normal subjects; the left eye (OD) and the right eye (OS) responses were almost superimposed showing good responses from healthy retinas.

were removed in the parsimonious model. By fitting the effects of gender and age independently, we now had an unambiguous picture of the other independent effects such as the presence of AMD. For the normal control subjects, it was found that eccentricity did not significantly affect the mean responses as was thought initially. There was also a significant interaction between age and repeats, at a significance level of 0.29 ± 0.05 μV ($p<0.000$) indicating older subjects performed better with the number of repeats. The responses from the normal control subjects eyes were found to be similar to the tested normal control eye. As a new technique that was only starting to be explored, assessment of the mfVEP's repeatability under the recording conditions used in this study was an important determinant of the utility of this technique. We also found from the regression analysis model (not shown) that better responses were recorded with the number of repeats for subjects regardless of the gender and the age.

In the case of bilateral cvAMD, subject 219 (male, 81 y., OS 6/60, OD 6/36: Figure 3), still showed response from the legally blind eye (due to disciform macular degenerative leakage with haemorrhage). Response amplitudes from his better eye, OS were bigger in the lower hemifield with reduced response of the inner three eccentricities in the lower hemifield and at almost all eccentricities in the upper hemifield. Another subject in this category was 227 (female, 77 y., Figure 4). The response amplitude in this subject was reduced dramatically in almost all eccentricities, both upper and lower visual hemifields.

In the case of unilateral AMD, subject 221(male, 51 y., OD was the better eye 6/5; OS had exudative cvAMD, Figure 5) the response amplitude showed patchy response, mainly reduced amplitude not confined to the upper but also in the lower eccentricities and at almost all eccentricities. Similarly, subject 234 (female, 91 y., OD, 6/12, Figure 6) also showed a remarkable difference between the response amplitude between both eyes, understandingly from the condition of the tested eye, in addition to the reduced response amplitudes of the upper hemifield.

These early results proved that in the cases of advance AMD, the peripheral vision might be affected too. It was also worthy to note that there were indeed small responses from legally blind eyes, as none of the mfVEP waveforms were completely extinguished. This could only mean that this technique was able to stimulate the remaining retinal neurons of patients who were blind from a end stage photoreceptor generative disease like AMD. The pattern pulse mfVEP technique could detect these changes remarkably well and was able to pick up these differences from the different stages of this debilitating disease. Future work would involve a detailed analysis of macular retinal function along with classification, extent and location of abnormalities of the pathogenesis of AMD.

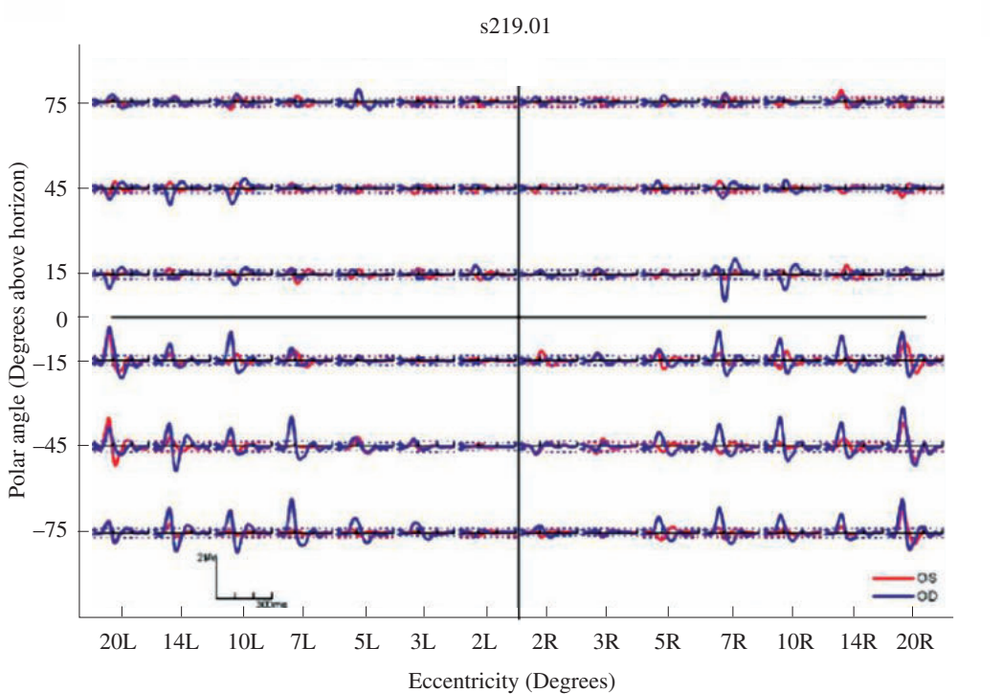

Figure 3. Rectilinear layout of the response set of the grand means from bilateral AMD subject 219; showing patchy reduced responses from both eyes.

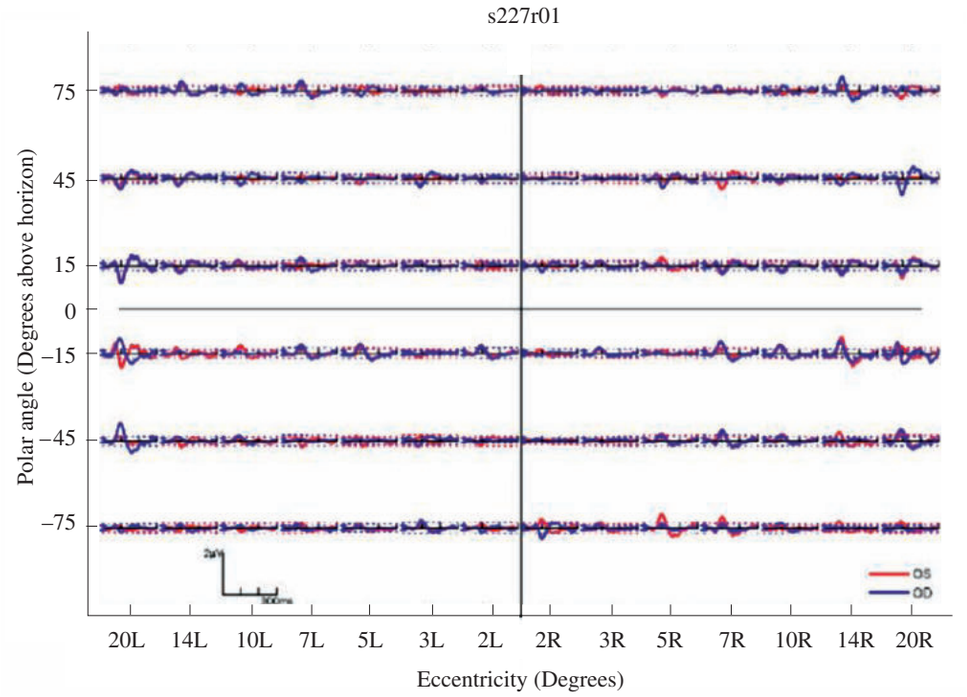

Figure 4. Rectilinear layout of the response set of the grand means from bilateral AMD subject 227, showing the severely reduced responses especially in the central regions.

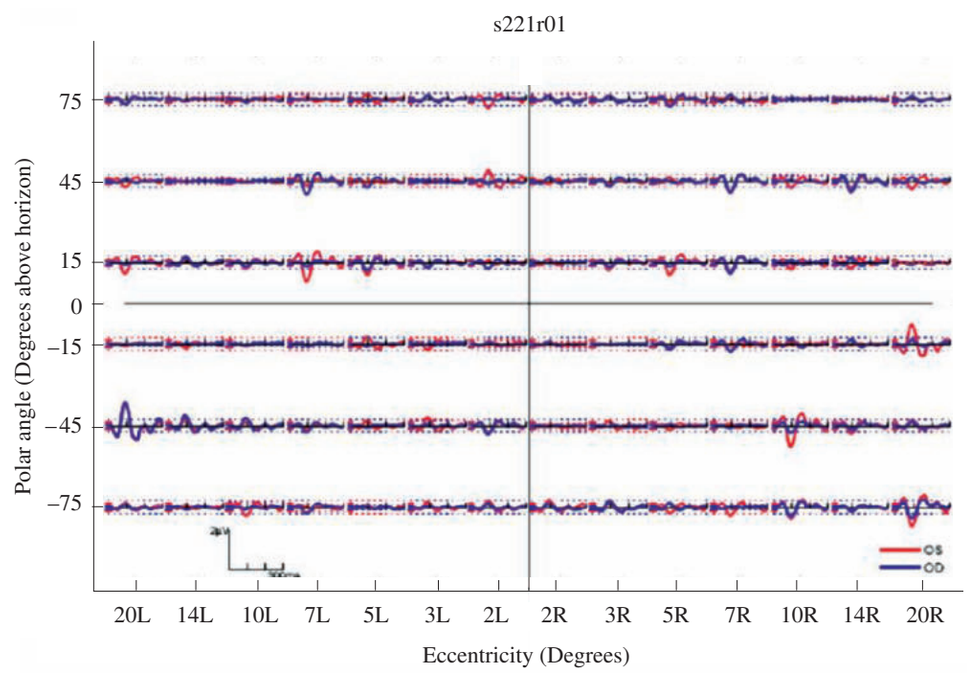

Figure 5. Rectilinear layout of the response set of the grand means from unilateral AMD subject 221. Although the left eye (OD) is the better eye, it has already showing early signs of possible retinal degeneration.

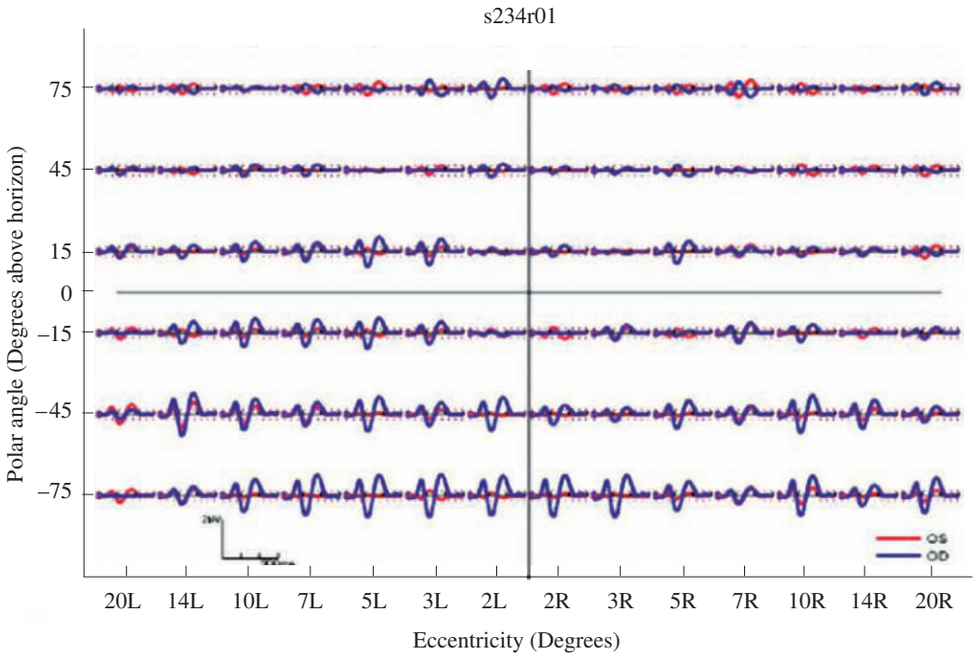

Figure 6. Rectilinear layout of the response set of the grand means from unilateral AMD subject 234. In this subject, the OD is the better eye, with the severely reduced responses from the right eye (OS) from almost all the tested regions. The OD responses were smaller in the upper visual hemifield, again probably showing early signs of retinal changes.

ACKNOWLEDGEMENTS

The authors wish to thank The Canberra Eye Hospitals and the patients who had volunteered to make this study possible.

Date of submission: January 2008
Date of acceptance: June 2009

REFERENCES

Attebo, K *et al.* 1996, 'Visual acuity and the causes of visual loss in Australia: the Blue Mountains eye study', *Ophthalmology,* vol. 103, no. 3, pp. 357–364.

Curcio, C *et al*. 1996, 'Photoreceptor loss in age-related macular degeneration', *Invest. Ophthalmol. Vis. Sci.,* vol. 37, no. 7, pp. 1236–1249.

Falsini, B *et al*. 1999, 'Focal electroretinograms and fundus appearance in nonexudative age-related macular degeneration',*Graefe's Archive for Clinical and Experimental Ophthalmology*, vol. 237, pp. 193–200.

Hood, DC 2000, 'Assessing retinal function with the multifocal technique', *Progress in Retinal and Eye Research*, vol. 19, pp. 607–646.

Huang, S *et al*. 2000, 'The multifocal electroretinogram in the age-related maculopathies', *Documenta Ophthalmologica*, vol. 101, pp. 115–124.

James, A 2003, 'The pattern pulse multifocal visual evoked potential', *Invest. Ophthalmol. Vis. Sci*., vol. 44, pp. 879–890.

Jurklies, B *et al*. 2002, 'Monitoring retinal function in neovascular maculopathy using multifocal electroretinography — early and long-term correlation with clinical findings', *Graefe's Archive for Clinical and Experimental Ophthalmology*, vol. 240, no. 4, pp. 244–264.

Klein, R *et al*. 1992, 'Prevalence of age related maculopathy: The Beaver Dam Study', *Ophthalmology*, vol. 99, pp. 933–943.

Li, J, Tso, M & Lam, T 2001, 'Reduced amplitude and delayed latency in foveal response of multifocal electroretinogram in early age related macular degeneration', *British Journal of Ophthalmology*, vol. 85, pp. 287–290.

Mitchell, P *et al.* 1995, 'Prevalence of age-related maculopathy in Australia: The blue mountains eye study', *Ophthalmology*, vol. 102, no. 10, pp. 1450–1460.

Owsley, C *et al*. 2000, 'Psychophysical evidence for rod vulnerability in age-related macular degeneration', *Invest. Ophthalmol. Vis. Sci*., vol. 41, no. 1, pp. 267–273.

Reme, CE *et al*. 2003, 'Why study rod cell death in retinal degenerations and how', *Documenta Ophthalmologica*, vol. 106, no. 1, pp. 25–29.

Van Newkirk, M, Mukesh B *et al*. (2000). 'The prevalence of age-related maculopathy: the visual impairment project,' *Ophthalmology*, vol. 107, pp. 1593–1600.

Van Newkirk, M *et al*. 2001, 'Cause-specific prevalence of bilateral visual impairment in Victoria, Australia : the visual impairment project', *Ophthalmology*, vol. 108, no. 5, pp. 960–967.

Verdon, WA & Haegerstrom-Portnoy G 1998, 'Topography of the multifocal electroretinogram', *Documenta Ophthalmologica*, vol. 95, no. 1, pp. 73–90.

Vingerling, J *et al*. 1995, 'The prevalence of age-related maculopathy in the Rotterdam Study', *Ophthalmology*, vol. 102, pp. 205–210.

Walter, P *et al*. 2000, 'Unusual visual evoked potentials in patient with age-related macular degeneration', *Opthalmologica*, vol. 214, pp. 312–319.

Walter, P *et al*. 1999, 'Electrophysiological abnormalities in age-related macular degeneration', *Graefe's Archive for Clinical and Experimental Ophthalmology*, vol. 237, pp. 962–968.

ASM Sci. J., **3(1)**, 39–44

Fluorescence Characteristics of 3-Nitro-2-phenoxypyridine and 3-Nitro-2(4-methyl)phenoxypyridine

Z. Abdullah[1]*, Z.I.A.Halim[1], M.A.A. Bakar[1] and A.M. Idris[1]

3-Nitro-2-phenoxypyridine and 3-nitro-2-(4-methyl)phenoxypyridine were obtained when 2-chloro-3-nitropyridine was treated with phenol and *p*-cresol, respectively. Fluorescence studies were carried out in various solvents, in capped and uncapped conditions and for differing concentrations. Both 3-nitro-2-phenoxypyridine and 3-nitro-2-(4-methyl)phenoxypyridine were fluorescent compounds but 3-Nitro-2-(4-methyl)phenoxypyridine was more fluorescent than 3-nitro-2-phenoxypyridine in all the solvents used. The fluorescence intensity decreased with concentration and time.

Key words: 3-nitro-2-phenoxypyridine; 3-nitro-2-(4-methyl)phenoxypyridine; fluorescence; phenol; *p*-cresol; electron

The pyridine ring systems are very widely distributed in nature, especially in the plant kingdom. Many important alkaloids are pyridine derivatives (Joule, Mills & Smith 1995). The pyridine ring plays a key role in several biological processes, such as in the oxidation/reduction of coenzyme nicotine adenine dinucleotide (NAPP) (Badger 1961; Acheson 1967).

The fluorescence characteristic of pyridine or other heterocyclics have not been extensively studied, even though a wide variety of heterocylic compounds are believed to be fluorescent (Bridges, Davies & William 1966).

This work involved synthesizing various pyridine derivatives and was followed by studying their fluorescence characteristics in various solvents, over time intervals and with different concentrations. This work was also aimed to study the effect of electron donating and electron withdrawing groups on fluorescence intensity. However, this paper will only report on the fluorescence characteristics of 3-nitro-2-phenoxypyridine and 3-nitro-2-(4-methyl) phenoxypyridine.

MATERIALS AND METHODS

Synthesis of 3-Nitro-2-phenoxypyridine

Phenol (0.26 ml), sodium hydroxide (0.1248 g) and water (1 ml) were refluxed until a residual solid was formed. 2-Chloro-3-nitropyridine (0.5014 g) was added to the mixture and refluxed for another 4 h. The mixture was evaporated and the slurry was extracted with chloroform (2 × 10 ml). The chloroform extracts were washed with 5% sodium hydroxide (10 ml) and water (3 × 10 ml) and dried over anhydrous sodium sulphate. Evaporation of the solvent gave the product, a light yellow brownish solid. TLC was carried out to check the purity of the product. Yield: 0.3502 g, 52%; IR(cm^{-1}) : 2923.83–2855.46, 1577.22, 1459.97, 1246.82; ^{1}H NMR (400 MHz, $CDCl_3$) , δ:8.30, m, 2H (H-4, H-6), 7.42, dd, 2H (H-2', H-6'), 7.25, t, 1H (H-5), 7.10, m, 3H (H-3', H-4', H-5'); ^{13}C NMR (400 MHz, $CDCl_3$) , δ:150.789 (C-2), 147.516 (C-1'), 146.778 (C-3), 130.454 (C-6, C-4), 124.706 (C-2', C-6'), 120.806 (C-4'), 116.700 (C-3', C-5'), 113.238 (C-5); M^+: 216.00; $C_{11}H_8N_2O_3$ requires M^+ =216.19

Synthesis of 3-Nitro-2-(4-methyl)phenoxypyridine

p-Cresol (0.51 ml), sodium hydroxide (0.1952 g) and water (2 ml) were heated until a solid was formed. The solid and 2-chloro-3-nitropyridine (0.7737 g) were refluxed for about 7 h. The mixture was evaporated and the residue slurry was extracted with chloroform (25 ml). The chloroform extracts were washed with 5% sodium hydroxide (10 ml) and water (3 × 10 ml), and dried over anhydrous sodium sulphate. Evaporation of solvent gave the products as a light yellow brownish solid. Yield: 0.2276 g, 20.28%; IR(cm^{-1}) : 2954.00–2854.08, 1577.22, 1592.42–1506.72, 1456.77–1424.65, 1245.97–1164.67, 805.24; ^{1}H NMR (400 MHz, $CDCl_3$) , δ:8.30, m, 2H (H-5, H-4), 7.42, t, 2H (H-3', H-5'), 7.25, d, 1H (H-5), 7.09, m, 2H (H-2', H-6'); 2.38, s, 3H, s, (CH_3); ^{13}C NMR (400 MHz, $CDCl_3$) , δ:156.372 (C-2), 152.023 (C-2', C-4'), 150.451 (C-3), 135.717 (C-5, C-4),

[1]Department of Chemistry, Faculty of Science, University of Malaya, 50603 Kuala Lumpur, Malaysia
* Corresponding author (e-mail: zana@um.edu.my)

130.487 (C-2', C-6'), 121.673 (C-3', C-5'), 118.243 (C-5), 21.165 (C of CH_3); M^+: 230.00; $C_{12}H_{10}N_2O_3$ requires M^+ =230.22

SPECTROSCOPIC ANALYSIS

All solvents were re-distilled before use. Melting points were determined with Electrothermal Melting Point Apparatus and were not corrected. Infrared spectra were recorded using Perkin Elmer 298 Infrared Spectrometer and FTIR Perkin Elmer 1600 Series. ^1H and ^{13}C NMR spectra were recorded on a Joel JNM-LA400 FT and Joel-EX90A FT NMR systems spectrometer. The mass spectrum were recorded using GCMS Hewlett-Packard HP 6890 Series with mass selective indicator.

FLUORESCENCE STUDIES

3-Nitro-2-phenoxypyridine and 3-nitro-2-(4-methyl) phenoxypyridine of the same concentrations were prepared in ethanol, ether, tetrahydrofuran, ethyl acetate and acetonitrile. Different concentrations of these compounds in tetrahydrofuran were prepared to study the effect of concentration on fluorescence intensity. The fluorescence measurement was carried out in a quartz cell, using Fluorescence Spectrometer Model F-2000 Hitachi at room temperature with the same settings for all samples.

RESULTS AND DISCUSSION

Treatment of 2-chloro-3-nitropyridine with phenol and *p*-cresol gave 3-nitro-2-phenoxypyridine and 3-nitro-2-(4-methyl)phenoxypyridine respectively, as shown in Scheme 1. The structures of both compounds were confirmed by infrared, ^1H NMR, ^{13}C NMR and GC-Mass spectra as recorded in the experimental section.

2-Chloropyridine showed a weak fluorescence peak in both acetonitrile and tetrahydrofuran at 438 nm and when excited at 378 nm while no fluorescence peak was observed in ethanol, ethyl acetate and chloroform (Noordini *et al*. 2008). 2-Chloro-3-nitropyridine on the other hand, is a non-fluorescent compound. The presence of a nitro group in the pyridine ring diminished the fluorescence characteristics of this compound through electron withdrawal capabilities and as a result reduced the electron density in the system.

Table 1 shows the fluorescence characteristics of 3-nitro-2-phenoxypyridine in various solvents in capped and uncapped conditions. It can be seen from the table that 3-nitro-2-phenoxypyridine fluorescenced in tetrahydrofuran and ether only.

Higher fluorescence intensity was observed in tetrahydrofuran as compared to ether. This observation was probably due to a complex forming between 3-nitro-2-phenoxypyridine and the solvents, thus reducing the

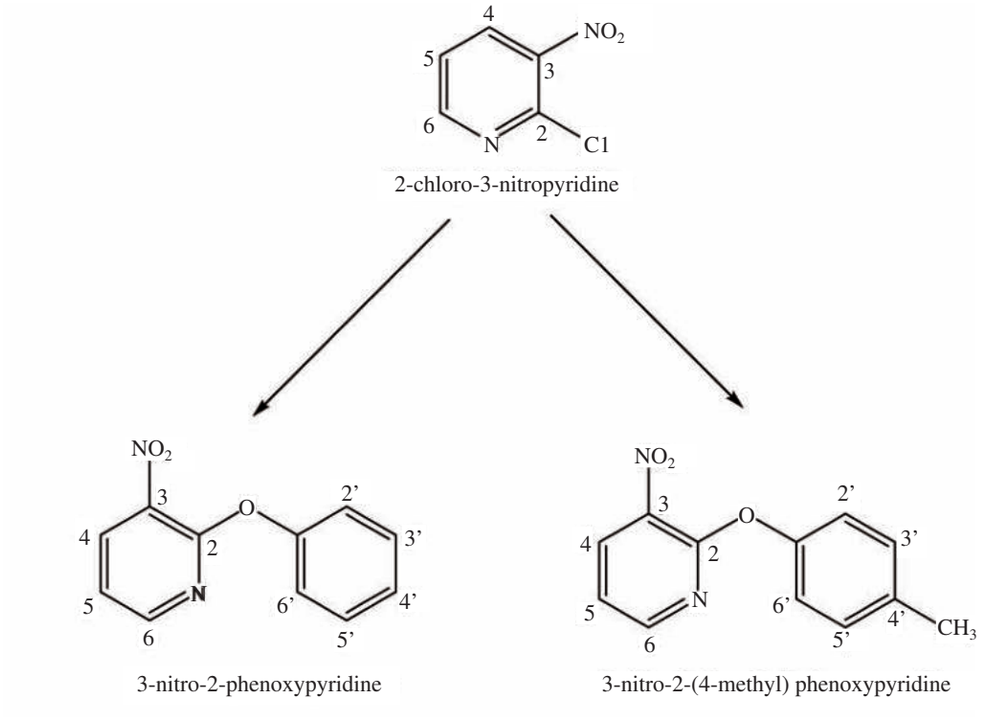

Scheme 1

Table 1. Fluorescence characteristics of 3-nitro-2-phenoxypyridine in various solvents in capped and uncapped conditions.

Condition	Solvent	Excitation wavelength/nm	Fluorescence wavelength/nm	Intensity
Capped	Tetrahydrofuran	286	306	3.372
	Ether	275	325	1.325
	Ethanol		Non-fluorescent	
	Methanol		Non-fluorescent	
	Acetonitrile		Non-fluorescent	
	Chloroform		Non-fluorescent	
	Dichloromethane		Non-fluorescent	
Uncapped	Tetrahydrofuran	286	306	3.683
	Ether	275	326	1.193
	Ethanol		Non-fluorescent	
	Methanol		Non-fluorescent	
	Acetonitrile		Non-fluorescent	
	Chloroform		Non-fluorescent	
	Dichloromethane		Non-fluorescent	

transition n to π*. As a result, a relatively high fluorescence intensity was observed. The lower fluorescence intensity observed when ether was used was believed to be due to the complex that was formed with ether being less rigid as compared to the complex formed with tetrahydrofuran. As a result, some of the energy absorbed was dissipated as heat and a low fluorescence intensity was recorded.

Figures 1 and 2 show the fluorescence spectra of 3-nitro-2-phenoxypyridine in ether and tetrahydrofuran in capped and uncapped conditions.

The fluorescence intensity of 3-nitro-2-phenoxypyridine in capped condition was higher than in uncapped condition. The same phenomena was observed with all other systems studied (Noordini *et al*. 2008). This phenomena, which was observed with the uncapped condition is believed to be due to the unlimited amount of oxygen in the quartz cell which quenched the fluorescence intensity of the compounds (Dehmlow & Dehmlow 1980; Haroutounion & Katnezellenbogen 1995). Oxygen has an unusually large diffusion coefficient. Thus, prolonged exposure of the solution to the atmosphere could result in a large quantity of oxygen diffusing into the solution (Wen *et al*. 2008). As a result, a decrease in fluorescence intensity was observed.

Table 2 shows the fluorescence characteristics of 3-nitro-2(4-methyl)phenoxypyridine in various solvents for capped and uncapped samples. Similar observations as 3-nitro-2-phenoxypridine were recorded.

Table 2 shows that 3-nitro-2-(4-methyl)phenoxypyridine was more fluorescent than 3-nitro-2-phenoxypyridine of similar concentration. The higher fluorescence intensity which was observed with 3-nitro-2-phenoxypyridine was due to the presence of a –CH3 group, an electron donor substituent which donates the electrons to the system, thus increasing the electron density within the system (Wen *et al*. 2008). As a result, an increase in fluorescence intensity was observed. The intensity of fluorescence peaks in capped and uncapped conditions was observed to be having similar characteristics to that of 3-nitro-2-phenoxypyridine. The fluorescence spectra of 3-nitro-2-(4-methyl)phenoxypyridine in various solvents are shown in Figures 2 and 3.

Tables 3 and 4 show the fluorescence characteristics of both compounds with time and concentrations, respectively.

Both compounds showed a decrease in fluorescence intensity with time as shown in Table 3 for capped samples. The same observations were recorded with pyrimidine and pyrazine systems studied earlier (Abdullah 2006).

The fluorescence characteristic of these compounds versus concentrations in tetrahydrofuran were as shown in Table 4. It can be seen that both compounds showed a decrease in fluorescence intensity with concentrations which was probably due to the solute quenching effect.

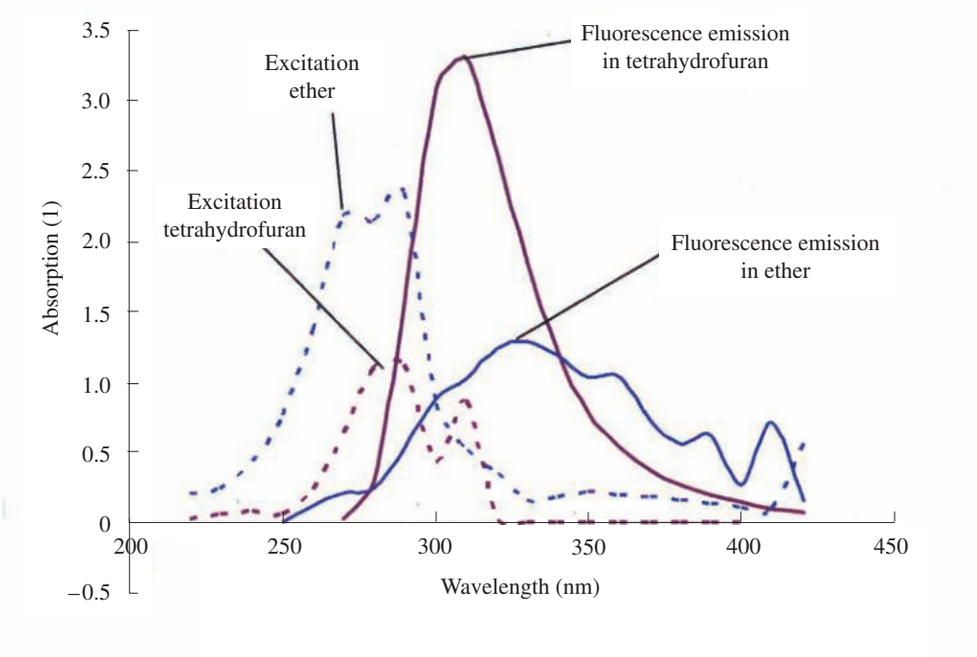

Figure 1. Fluorescence spectra of 3-nitro-2-phenoxypyridine in ether and tetrahydrofuran in capped condition.

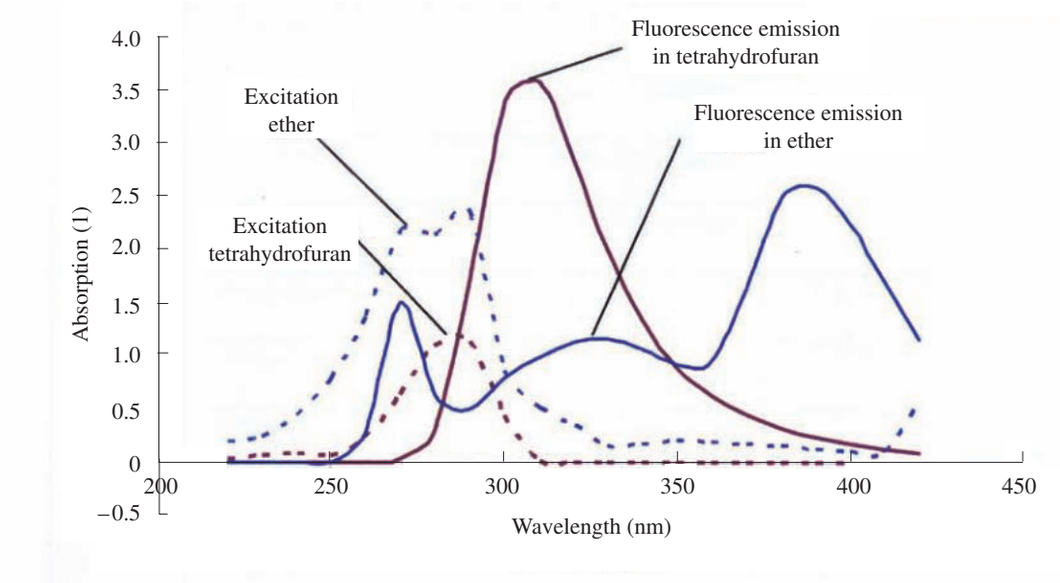

Figure 2. Fluorescence spectra of 3-nitro-2-phenoxypyridine in ether and tetrahydrofuran in uncapped condition.

Table 2. Fluorescence characteristic of 3-nitro-2-(4-methyl)phenoxypyridine in various solvents.

Condition	Solvent	Excitation wavelength/nm	Fluorescence wavelength/nm	Intensity
Capped	Tetrahydrofuran	286	306	3.409
	Ether	275	328	1.460
	Ethanol		Non-fluorescent	
	Methanol		Non-fluorescent	
	Acetonitrile		Non-fluorescent	
	Chloroform		Non-fluorescent	
	Dichloromethane		Non-fluorescent	
Uncapped	Tetrahydrofuran	286	306	3.326
	Ether	275	327	1.418
	Ethanol		Non-fluorescent	
	Methanol		Non-fluorescent	
	Acetonitrile		Non-fluorescent	
	Chloroform		Non-fluorescent	
	Dichloromethane		Non-fluorescent	

Table 3. Fluorescence characteristics of 3-nitro-2-phenoxy pyridine and 3-nitro-2-(4-methyl)phenoxypyridine versus time in capped condition.

Compound	Duration/min	Excitation wavelength/nm	Fluorescence wavelength/nm	Intensity
3-nitro-2-phenoxypyridine	Immediately	286	306	3.372
	30		305	3.305
	60		306	3.205
	120		306	3.106
3-nitro-2-(4-methyl) phenoxypyridine	Immediately	287	307	3.409
	30		306	3.394
	60		306	3.296
	120		306	3.170

Table 4. Fluorescence characteristics of 3-nitro-2-phenoxy pyridine and 3-nitro-2-(4-methyl)phenoxypyridine in different concentrations.

Compound	Concentration/M	Solvent	Excitation wavelength/nm	Fluorescence wavelength/nm	Intensity
3-nitro-2-phenoxypyridine	4.35×10^{-4}	THF	286	309	1.156
	4.40×10^{-5}	THF	286	306	2.060
	4.63×10^{-6}	THF	286	306	3.372
3-nitro-2-(4-methyl) phenoxypyridine	4.35×10^{-4}	THF	289	308	0.144
	4.40×10^{-5}	THF	289	306	2.672
	4.63×10^{-6}	THF	289	306	3.409

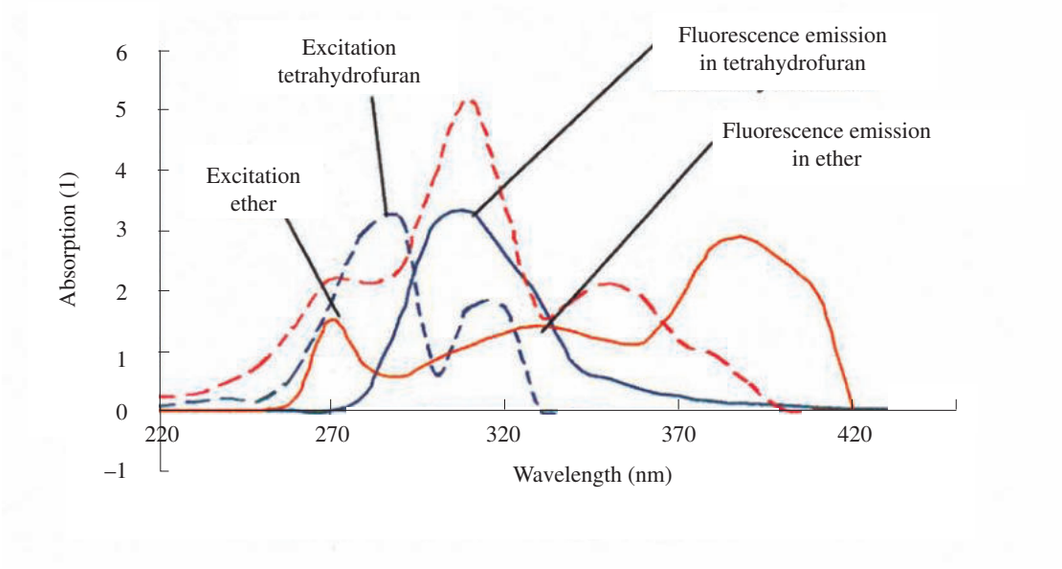

Figure 3. Fluorescence spectra of 3-nitro-2-(4-methyl)phenoxypyridine in uncapped condition in various solvents.

CONCLUSION

2-Chloropyridine is a fluorescent compound but on introduction of a nitro group at C-3 i.e. in 2-chloro-3-nitropyridine, no fluorescence peak was recorded. Both 3-nitro-2-phenoxypyridine and 3-nitro-2-(4-methyl) phenoxypyridine were fluorescent compounds, but -nitro-2-(4-methyl)phenoxypyridine was more fluorescent than 3-nitro-2-phenoxypyridine. Both compunds showed a gradual decrease in fluorescence intensity with time and concentration. The fluorescence intensity was reduced on prolonged exposure to air.

ACKNOWLEDGEMENTS

Financial support of this work by the Academy of Science and University of Malaya is gratefully acknowledged.

Date of submission: April 2008
Date of acceptance: June 2009

REFERENCES

Joule, JA, Mills, K, & Smith, GF 1995, *Heterocyclic chemistry*, Chapman and Hall, New York.

Badger, GM 1961, *The chemistry of heterocyclic compounds*, Adelaide, South Australia.

Acheson, RM 1967, *An introduction to the chemistry of heterocyclic compounds*, John Wiley and Sons, New York.

Bridges, JW, Davies, DS & William, RT 1966, *Biochem J*., vol. 98, pp. 451.

Noordini, MS *et al*. 2008, 'Fluorescence properties of 2-N-anilino and 2-N-piperidinopyridines: effect of solvents', *Inter. Journal of Chem. Sciences*, vol. 6, no. 2, pp. 933–941.

Abdullah, Z *et al*. 2004, 'Fluorescence studies and selected 2-alkylaminopyrimidines', *Molecules*, vol. 9, pp. 520–526.

Dehmlow, EV & Dehmlow, SS 1980, *Phase transfer catalysis*, Verlag Chemie.

Haroutounion, SA & Katnezellenbogen, JA 1995, *Tetrahedron*, vol. 51, no. 6, pp. 1585–1598,

Wen, YT *et al.* 2008, 'Two photo-absorption properties of disubstituted antracene. Effect of 9, 10 substituents', *Journal of Fluorescence*, vol. 18, pp. 403–411.

ASM Sci. J., **3(1)**, 45–50

Histological Observation of Gingival Enlargement Induced by Cyclosporin A and Nifedipine: A Study in Rabbits

F.H. Al-Bayaty[1*], B.O. Al-Tay[2], S.S. Al-Kushali[3] and L. Mahmmod[2]

A study was undertaken to estimate the histological changes of gingival enlargement induced by Cyclosporin A (CsA) and Nifedipine, separately and in combination. Twelve adult rabbits were divided equally into four main groups. The first group received 10 mg/kg/day Nifedipine, the second received 10 mg/kg/day CsA, and the third received a combination of 10 mg/kg /day Nifedipine and CsA by gastric feeding. The fourth was regarded as a control group. Animals were given the drugs from day 1 of the experiment until day 70. They were then sacrificed for histological purposes. Results showed increase in the thickness of the epithelium with keratosis and acanthosis, and also increased vascularity. Collagen fibres and fibroblasts at different rates in the three histological groups were observed. Significant alveolar bone resorption with increased marrow spaces filled with fatty tissue were found in the CsA group. Non-significant changes in the alveolar bone of the Nifedipine group while subsequent bone resorption and bone deposition were seen in the combination group. These changes could be due to the effect of both drugs. Significant changes in the gingiva and the alveolar bone were shown in the three experimental groups compared with the control group.

Key words: Cyclosporin A, Nifedipine; histological observation; rabbits; epithelium; keratosis; acanthosis; vascularity; alveolar bone

Although gingival enlargement has been recognized as an adverse effect of phenytoin therapy, it has also been reported in association with the use of cyclosporine and calcium channel blockers (Brunt *et al*. 1996). Cyclosporine A (CsA) is a potent immuno-suppressive drug. It has many side effects beside hypertension, nephrotoxicity, hepatotoxicity, tremor and hirsutism, CsA also induces gingival enlargement (Fu *et al.* 2001). Nifedipine is a calcium channel blocker. It too, has many side effects, including peripheral vasodilatation, dizziness, flushing, headache, weakness, nausea, peripheral edema, joint stiffness, dermatitis, pruritis and urticaria. Nifidipine has also been reported to induce gingival enlargement (Kataaoka *et al*. 2001). Since organ transplant patients who were administered CsA often had renal hypertension, they were generally prescribed calcium channel blockers, such as Nifidipine, Diltiazem or Verapamil as vasodilator to control blood pressure. Researchers have demonstrated that treatment with CsA and Nifidipine increased the severity of gingival enlargement when compared with CsA or Nifidipine treatment alone (Ovalle *et al*. 1995). The histological appearance of gingival enlargement induced by CsA and Nifidipine is similar to that of Phenyton induced gingival enlargement. The connective tissue is covered by an overlying irregular multilayered parakeratinized epithelium with elongated retepegs penetrating deep into the subepithelial region. The connective tissue appeared with foci of chronic inflammatory cells and increased vascularity, many large multinucleated osteoclasts and increased eroded surfaces that indicate active resorption at the periodontal aspect of alveolar bone in CsA exposed animals (Fu *et al*. 1999). Nifedipine exhibits an inhibitory effect on bone resorption up to 50%. Calcium channel blockers are mainly prescribed for post-middle-aged patients to control hypertension or myocardial disorders (Henry 1980). CsA is prescribed for a wide range of patients due to its wide spectrum of efficacy. These factors revealed difficulties to evaluate the etiology of drug induced gingival enlargement caused by calcium channel blockers and CsA and to compare the factors involved. The objective of this study was to induce gingival overgrowth in rabbits by CsA, Nifidipine separately and by combination of CsA and Nifidipine, as well as to evaluate the histological changes accrued in the periodontium through histological investigation.

[1]Department of Restorative Dentistry, Faculty of Dentistry, Universiti Teknologi MARA, 40450 Shah Alam, Selangor, Malaysia
[2]College of Dentistry, University of Baghdad, Iraq
[3]College of Sciences, University of Baghdad, Iraq
* Corresponding author (e-mail: drfouadhm@yahoo.com)

MATERIALS AND METHODS

Experimental Animals

Twelve healthy adult rabbits of both sexes, with ages 8–12 months and average weights of 2 Kg ± 250 gm were used in this study. Animals were maintained on standard laboratory diet, allowed free access to tap water and kept in stainless steel cages in an environmentally controlled room. These animals were supplied by the Medical Research Center, AL-Nahrien College of Medicine.

Method of Drugs Administration

Nifidipine administration. Nifidipine (Ronian) in capsules 10mg/capsule was used in this study. Nifidipine is a liquid drug. It was prepared in a dark room by using dim light and given orally by oral tube; this gastric feeding procedure was described by Fu *et al*. 1996 (Figure 1). The daily dose used was 10 mg /Kg of body weight. This dose was suggested by Hsien *et al*. (2001) to be effective in causing gingival enlargement.

Cyclosporin administration. Cyclosporin (sandimmun, neural) was in capsules of 50 mg/capsule.The CsA dose was dissolved in 5% ethanol and given orally by gastric feeding with the aid of an oral tube. The daily dose was 10 mg/Kg of body weight. This dose according to Spolidorio *et al*. (2001) was capable of inducing gingival enlargement in the experimental animals.

All animals were allowed to acclimatize to the laboratory environment for a period of ten days. They were then divided into four groups: three experimental and one control:

- Experimental group No. 1 — Three rabbits received a daily equal dose of Nifidipine10 mg/Kg of body weight by oral tube.
- Experimental groups No. 2 — Three rabbits received a daily equal dose of CsA 10 mg/Kg of body weight by oral tube.
- Experimental groups No. 3 — Three rabbits received a daily equal dose of Nifidipine10 mg/Kg of body weight, in addition to daily equal dose of CsA 10 mg/Kg of body weight by oral tube.
- Control group — Three rabbits received no drug; they were regarded as a control group.

The three experimental groups received the drugs from day 1 to day 70 of the experiment. All the animals were then sacrificed by using an overdose of chloroform inhalation, then the heads were separated and the maxilla, and the mandible were dissected with the surrounding gingival and soft tissue. The soft tissue was then removed for histological examination.

Histological Preparation and Examination

After fixation, the specimens were decalcified in 10% formic acid for three weeks. The decalcified sections were then prepared according to the method described by Donath and Breuner (1992). The specimens were embedded in paraffin wax. Serial sagittal sections were cut from each specimen with the microtome set at 5 microns. The sections were stained with hematoxylin and eosin. All the sections were examined under Olympus light microscope using an objective lens of 4 ×, 10 ×, and 40 ×.

Figure 1. Gastric feeding procedure with the oral tube.

RESULTS

Histological sections obtained from animals of the three experimental groups revealed significant changes in the periodontium compared with those obtained from the control group throughout the same period of the experiment.

Group No. 1 received Nifedipine: Histological investigations of this group demonstrated obvious changes compared to the control group. Sections showed a thickened multilayered hyperkeratinized epithelium, acanthosis, maturation and differentiation in the sulcular epithelium with elongated retepegs. The subepithelial region showed a large number of fibroblasts and collagen fibres. Increased vascularity and presence of congested blood vessels were observed. No significant changes in the alveolar bone of the maxilla and mandible were observed in all animal models (Figures 2 and 3).

Group No. 2 received CsA: Histological changes in this group revealed significant changes compared to both Nifedipine and control groups. It showed a thickened multilayered hyperkeratinized epithelium with acanthosis and elongated finger-like retepegs. The subepithelial region showed increased numbers of fibroblasts and collagen fibres. Increased congested blood vessels were observed. Significant bone resorption with increased marrow spaces filled with fatty tissue and new osteiod formation could be seen in the alveolar bone of the maxilla and mandible (Figures 4, 5 and 6).

Group No. 3 received a combination of CsA and Nifedipine: Observations showed a noticeable acanthosis and hyperkeratinization with elongated irregular broad retepegs. The subepithelial region showed a large amount of collagen fibres and many fibroblasts compared to CsA and Nifedipine groups alone. Increased congested blood vessels extending into the dental pulp of the teeth were observed. Significant changes in the alveolar bone represented by bone resorption and bone deposition, and the appearance of obvious incremental lines which reflected the effect of both drugs (Figures 7, 8 and 9).

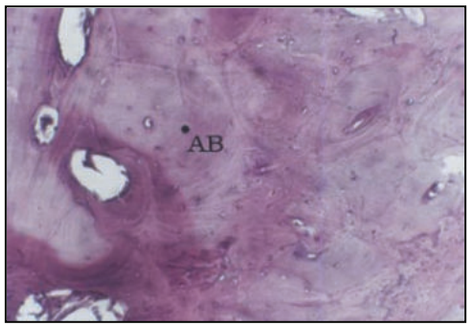

Figure 2. The alveolar bone AB in the control group on day 70. Notice the normal density and cellularity. H&E (× 10).

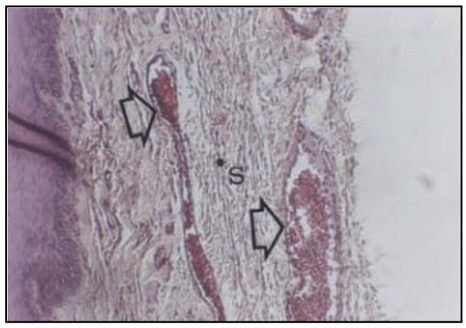

Figure 3. The subepithelial region (S) in Nifedipine group on day 70. Notice the congested blood vessels (arrows) and the condensed collagen Fibre H&E (× 10).

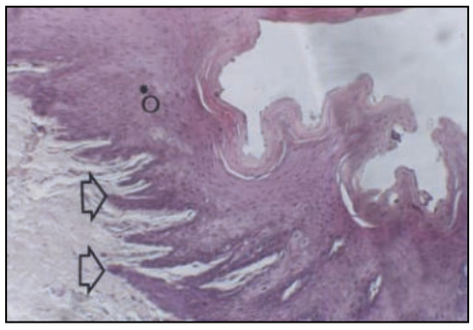

Figure 4. The oral epithelium (O) in CsA group on day 70. Notice the acanthosis and keratosis with the elongation of retepegs (arrows). (H&E) (× 10).

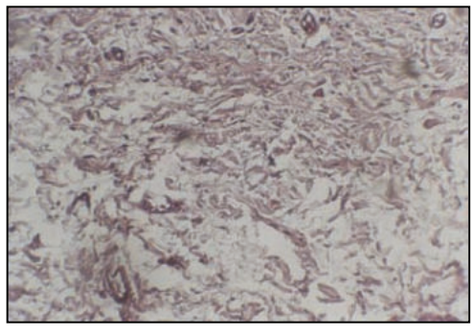

Figure 5. The subepithelial region in CsA group on day 70. Notice the increased amount of collagen fibre and fibroblasts. H&E (× 10).

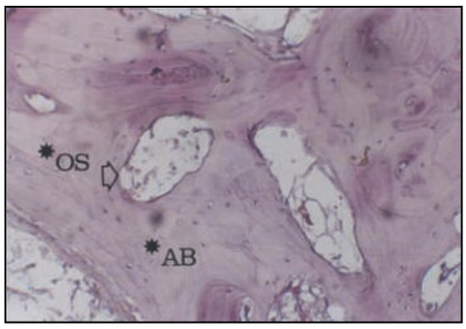

Figure 6. The alveolar bone AB in CsA group on day 70. Notice the new osteiod tissue (OS). H&E (× 10).

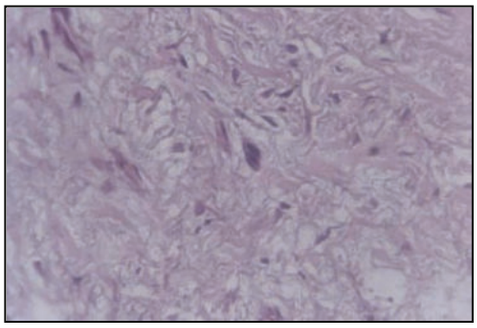

Figure 7. The subepithelial region in the combination group on day 70 showing cellular collagenous fibrous tissue (H&E) (× 40).

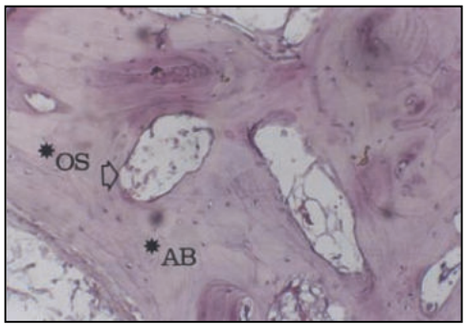

Figure 8. The subepithelial region (S) in the combination group on day 70, showing increased vascularity (arrows). H&E (× 10).

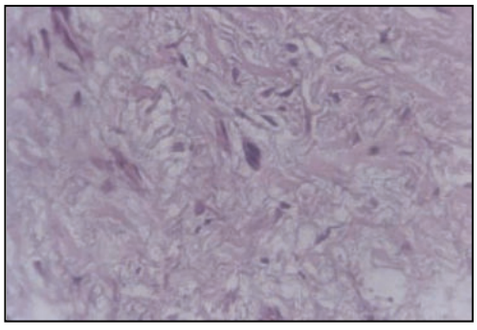

Figure 9. Shows the alveolar bone in the combination group on day 70. Notice the obvious incremental lines and high bone cellularity. H&E (× 40).

Group No. 4 received no drugs and was regarded as a control group: It showed normal non-keratinized stratified squamous epithelium. The subepithelial region showed scattered collagen fibres and fibroblasts. The alveolar bone appeared with normal density and cellularity (Figure 2).

DISCUSSION

This study was done to investigate the effect of CsA and Nifedipine separately and in combination on the periodontium of adult rabbits. In general, sections showed significant histological changes throughout the period of the experiment in the three experimental groups compared with day 0 of the experiment and the control group.

Dosage of the drugs in these experiments was based according to previous studies. The dosage of CsA was 10 mg/Kg of body weight; this dose had been shown to produce sufficient blood levels to induce immune suppression in animal's models as described by Vanden (1995). This dose would maintain the blood drug level between 100 and 400 mg/ml which was considered to be effective in causing gingival enlargement of 100% incidence in the experimental animals (Spolidorio *et al.* 2001).

The dosage of Nifedipine was 10 mg/Kg of body weight. This was dose sufficient to cause gingival enlargement in animal's models as described by Hsien *et al*. (2001). Nifedipine was prepared in a dark room by using dim light since the drug is photosensitive and may lose its activity when exposed to daylight (Katzung 1995).

The increased thickness of the epithelium which was manifested histologically by acanthosis might be due to the administration of the drugs which induced more differentiated epithelial cells. Both drugs increased the mitotic activity of the epithelial cells, especially in the oral epithelium. Other researchers have concluded that, sometimes gingival enlargement could also be attributed

to the increase in the thickness of the oral epithelium (Nurmenniemi *et al*. 2001).

The subepithelial region in the three experimental groups showed an increased number of fibroblasts and collagen fibres at different rates compared to the control group. CsA caused direct influence on the gingival fibroblast by increasing their proliferation and matrix formation (Schincaglia *et al*. 1992). For Nifedipine the most accepted mechanism of action is that the increased numbers of fibroblasts might be due to the inhibition of the lipopolysaccharide that stimulates macrophages induced death of the fibroblasts (Fugimori *et al*. 2001).

CsA, in our study increased alveolar bone resorption and decreased alveolar bone formation in the experimental group that received the drug. It inhibited osteoblast proliferation, cell number, mitogenisis, alkaline phosphate levels and cell attachment in vitro (Fu *et al*. 1999). However, CsA increased bone formation stimulated by parathyroid hormone, interleukin-1 and 1.25 dihydroxy vitamin D have been reported *in vitro* in many studies (Epstien *et al*. 1990).

In Nifedipine groups, no significant changes were noted in the alveolar bone of the maxilla and mandible of the animals. The drug exhibited an inhibitory effect on bone resorption by causing a direct influx of calcium into the cells (Ritchie *et al.* 1994) . Clinically, it has been reported that elderly patients treated for coronary heart disease over two years, Nifedipine caused a temporary increase in bone minerals density (Malinowska *et al*. 1996). In the combination group, subsequent bone resorption and deposition or remodeling caused the obvious appearance of the incremental lines (Poliana *et al*. 2001). Histological investigations showed increased vascularity of the sub-epithelial region and the appearance of many dilated blood vessels filled with blood in the combination group, even in the pulp of the teeth. These changes were more visible compared to the CsA group. The CsA group showed more vascularity than the Nifedipine group. This could be due to an obvious resorption and bone loss in CsA group which would lead to a sequential bone formation induced by resorptive stimuli. It might mask the genuine effect of the drug, as a normal defense mechanism of the body (Fu *et al.* 1999).

Osteogenesis had long been known to be associated with angiogenesis. Implanted endothelial cells seemed to enhance osteogenesis by neo-vascularization (Villanueva & Nimni 1990). Periocytes, surrounding and sharing a common basal membrane with the endothelial cells, were also considered as possible osteoblast progenitor cells (Bosse *et al*. 1994).

The vascularity in the subepithelial region in the Nifedipine treated group appeared to be less compared to that in CsA group. Nifedipine did not affect the bone or sometimes little bone deposition was seen. The combination group showed high vascularity in the subepithelial region due to the additive effects of the two drugs (Darbar *et al*. 1996).

CONCLUSION

Significant changes in the gingiva and the alveolar bone were shown in the three experimental groups compared with the control group. Motable bone resorption with increased marrow spaces filled with fatty tissue was observed in the CsA group compared to non-significant changes in the alveolar bone of the Nifedipine group. Obvious incremental lines were observed in the combination group due to the effect of drugs.

Date of submission: April 2008
Date of acceptance: June 2009

REFERENCES

Bosse, A, Wulf, M & Muller, KM 1994, 'Pericytes and ascular endothelial cells as potential osteoprogenitor cells', *Bone Miner*, vol. 25, p. 30.

Brunet, L *et al.* 1996, 'Gingival enlargement induced by drugs', *Drug-Saf*, vol. 15, no. 3, pp. 219–231.

Darbar UR *et al.* 1996, 'Combined treatment approach to gingival overgrowth due to drug therapy', *J. Clin. Periodontol*., vol. 23, no. 10, pp. 941–944.

Epstien, S, Schlosberg, M & Fallon M 1990, '1, 25- diyhdroxy –vitamin D3 modifies Cyclosporin-induced bone loss', *Calcif. Tissue Int.*, vol. 47, pp. 152–157.

Fu, E *et al*. 2001, 'CsA-induced gingival overgrowth at the newly formed edentulous ridge in rats: a morphological and histometric evaluation', *J. Periodontol*., vol. 72, pp. 889–894.

Fu, E *et al*. 1999, 'Effects of CsA on alveolar bone : an experimental study in rats', *J. Periodontol*., vol. 70, pp. 189–194

Fujimori, Y *et al*. 2001, 'Inhibition by Nifedipine of adherence and activated macrophage induced death of human gingival fibroblasts', *Eur. J. Pharmacol*., vol. 415, no. 1, pp. 95–103.

Henry, PD 1980, 'Comparative pharmacology of calcium antagonists: Nifedipine, Verpamil and diltiazem', *Am. J. Cardiol*., vol. 46, pp. 1047–1058.

Hsien, CC *et al*. 2001, 'Dose Nifedipine aggravates CsA-induced gingival overgrowth? An experiment in rats', *J. Periodontol*., vol. 72, pp. 532–537.

Kataaoka, M *et al*. 2001, 'Nifedipine induces gingival overgrowth in rats through a reduction in collagen phagocytosis by gingival fibroblasts', *Priodontol*., vol. 72, pp. 1078–1083.

Katzung, BG 1995, 'Vasodilatiors and treatment of angina pectoris', in *Basic and clinical pharmacology*; 6th edn, Chap 12, p. 180.

Malinowska, KB *et al*. 1996, 'The influence of calcium channel blocker on calcium p-Mg homeostasis and bone mass in patients with coronary heart disease and hypertension', *Osteoporosis Int.*, vol. 6, no. 1, pp. 184.

Mazariegos, GV *et al*. 2001, 'Conversion from CsA to tacrolimus in pediatric liver transplant recipient', *Paediatr.–Drugs*, vol. 3, no. 9, pp. 661–672.

Nurmenniemi, PK *et al*. 2001, 'Mitotic activity of keratinocytes in Nifedinpe and immunosuppressive medication induced gingival overgrowth', *J. Periodontol.*, vol. 72, no. 2, pp. 167–173.

OValle, F *et al*. 1995; Gingival overgrowth induced by Nifedipine and CsA: clinical and morphometric study with image analysis', *J. Clin. Periodont*., vol. 22, pp. 591–597.

Poliana, MD *et al.* 2001, 'The effect of an immunosuppressive therapy and its withdrawal on bone healing around titanium implants. A histometric study in rabbits', *Periodontol*., vol. 72, pp. 1391–1397.

Ritchie, CK *et al.* 1994, 'Direct effect of calcium channel antagonists on osteoclast function: alterations in bone resorption and intercellular calcium concentrations', *Endocrinol*., vol. 135, pp. 996–1003.

Schincaglia, GP *et al*. 1992, 'CsA increases type 1 procollagen production and mRNA level in human gingival fibroblasts *in vitro*', *J. Oral. Pathol. Med*., vol. 21, pp. 181–185.

Spolidorio, LC *et al*. 2001, 'Morphometric evaluation of gingival overgrowth and regression caused by Cyclosporin in rat', *J. Periodontal. Res*., vol. 36, no. 6, pp. 384–389.

Vaden, SL *et al*. 1995, 'The effect of cyclosporin versus standard care in dogs with naturally occurring glomerulonephritis', *J. Vet. Intern. Med*., vol. 9, pp, 259–266.

ASM Sci. J., **3(1)**, 51–57

Acceleration of Wound Healing by *Orthosiphon stamineus* Leaf Extract in Rats

A.A. Mahmood[1*], M.A. Hapipah[2], S. M. Noor[1], U.R. Kuppusamy[1], I. Salmah[1], M.E. Phipps[1] and H.M. Fouad[3]

The effects of topical application of *Orthosiphon stamineus* leaf extract on the rate of wound healing and histology of the healed wound were assessed. Four groups of adult male Sprague Dawley rats were experimentally wounded in the posterior neck area. A thin layer of blank placebo was applied topically to wounds of Group 1 rats. Wounds of experimental animals (Group 2 and 3) were dressed with placebo containing 5% and 10% *O. stamineus* extract, respectively. A thin layer of Intrasite gel® was applied topically to wounds of Group 4 animals as reference. Macroscopically, wounds dressed with placebo containing 5% (healed on day 14.50 ± 0.43) and 10% (healed on day 13.83 ± 0.21) *O. stamineus* extract each or Intrasite gel® (healed on day 13.13 ± 0.42) significantly accelerated the rate of wound healing compared to wounds dressed with blank placebo. Histological analysis of healed wounds confirmed the results. Wounds dressed with placebo containing 5%, 10% *O.stamineus* or Intrasite gel® showed markedly less scar width at wound enclosure and granulating tissue contained markedly more collagen, proliferating fibroblast with angiogenesis, and no inflammatory cells compared to wounds dressed with blank placebo. In conclusion, placebo containing 5% or 10% *O. stamineus* on extract-dressed wounds significantly accelerated the rate of wound healing in rats.

Key words: *Orthosiphon stamineus*; Sprague Dawley; rats; wound healing; histology; Intrasite gel® topical application

Orthosiphon stamineus, Benth (Lamiaceae) known locally as *Misai kucing* or *Kumis kucing* are among the popular medicinal plants used in traditional medicine for curing various diseases especially those affecting the urinary tract, diabetes mellitus, eruptive fever, epilepsy, gallstone, hepatitis, rheumatism, tonsillitis, hypertension, syphilis, gonorrhea, renal calculus, menstrual disorder and to improve physical strength (Awale *et al*. 2003; Olah *et al.* 2003; Sriplang *et al*. 2007). In Malaysia, the tea prepared from the leaves is taken as beverage to improve health and for treatment of kidney, bladder inflammation, gout and diabetes (Hegnauer 1966; Wanger 1982). *O. stamineus* is effective for alleviating hyperglycemia and improving lipid profile in diabetic rats (Sriplang *et al.* 2007), and possesses antioxidant and hepatoprotective effects (Yam *et al*. 2007). Phytochemical screening of *O. stamineus* extract showed several chemically active constituents, such as terpenoids, polyphenols and sterols (Tezuka *et al*. 2000). The polyphenols have *in vivo* antioxidant activities and have been used as natural antioxidants in food (Fuhrman *et al*. 1995). Polyphenol has been reported to be effective in reducing oxidative stress by inhibiting the formation of lipid peroxidation products in biological systems (Hollman & Katan 1999). There is no data available regarding the wound healing activity of *O. stamineus* leaf extracts. The present study was undertaken to evaluate the rate of wound healing properties of *O. stamineus* extract in experimental rats macroscopically and microscopically.

MATERIALS AND METHODS

Placebo

Blank placebo was obtained from the Department of Pharmacy, Faculty of Medicine, University of Malaya.

Intrasite Gel®

Intrasite gel® was purchased from University Malaya Medicial Centre Pharmacy. Intrasite gel®, is an amorphous hydrogel which gently re-hydrates necrotic tissue, facilitates autolytic debridemen, while being able to loosen and absorb slough and exudates, clearing the way for effective wound healing. It is also designed for wounds that are granulating and epithelialising. It can also be used to provide the optimum moist wound management environment during the later stages of wound closure. It

[1]Department of Molecular Medicine, Faculty of Medicine, University of Malaya, 50603 Kuala Lumpur, Malaysia
[2]Department of Chemistry, Faculty of Science, University of Malaya, 50603 Kuala Lumpur, Malaysia
[3]Department of Oral Medicine and Periodontology, Faculty of Dentistry, University of Malaya, 50603 Kuala Lumpur, Malaysia
* Corresponding author (e-mail: mahmood955@yahoo.com)

is non-adherent and does not harm viable tissue or the skin surrounding the wound. (Intrasite gel® is a trademark for Smith and Nephew Ltd) (Williams 1994).

Lignocaine HCl (2%, 100 mg/5 ml)

The local anesthesia was purchased from the experimental animal house, Faculty of Medicine, University Malaya. One ml of Lignocaine was injected subcutaneous (Delta Veterinary Laboratory PTY LTD, NSW 2011).

Plant Specimen and Preparation of Extraction

Fresh *O. stamineus* leaves were collected from Rawang, State of Selangor and identified by comparison with the voucher specimen deposited at the Herbarium of Rimba Ilmu, Institute of Science Biology, University of Malaya, Kuala Lumpur. The leaves were washed with distilled water, and then dried in the shade for 7–10 days. The dried leaves were ground to a powder before being extracted by maceration in ethanol (100 g/1500 ml, w/v) for two days at room temperature. The solvent was then filtered using a filter funnel and distilled under reduced pressure in an Eyala rotary evaporator (Sigma-Aldrich, USA). The extract was mixed homogeneously with placebo in a concentration of 5% and 10% (w/w) each.

Experimental animals

Sprague Dawley adult male rats were obtained from the experimental animal house, Faculty of Medicine, University of Malaya. The rats were divided randomly into four groups of 6 rats each. The rats that weighed between 180 g – 200 g, were housed separately (one rat per cage). The animals were maintained on standard pellet diet and tap water.

Experimentally Induced Wounds

The animals were anesthetized by diethyl ether. A patch of skin was shaved by electrical shaver, disinfected with 70% alcohol and injected with 1 ml of Lignocaine HCl (2%, 100 mg/5 ml). An area of uniform wound, 1.8 cm in diameter, was excised from the nape of the dorsal neck of all rats with the aid of a round seal as described by Morton & Melone (1972) (Figure 1). An incision of the muscle layer was avoided and tension of skin was kept constant during the procedure.

Topical Application of Vehicles

Wounds of Group 1 rats were dressed topically with a thin layer of blank placebo twice daily. A thin layer of 5% and 10% *O. stamineus* extracts in placebo were applied topically twice daily to the wounds of Groups 2 and 3 experimental animals, respectively. Wounds of Group 4 rats were dressed with a thin layer of Intrasite gel twice daily. The wound was observed daily until a complete wound-healing enclosure occured.

Histological Evaluation of Healed Wounds

The skin specimen from wounds healed areas were fixed in 10% buffered formalin and processed by a paraffin tissue

Figure 1. 1.8 cm diameter excision wound on day 0 before application of vehicle.

processing machine. The healed skin was assessed by taking a 5 µ section, stained with hematoxylin and eosin.

Statistical Analysis

All values are reported as mean ± s.e.m. and the statistical significance of differences among groups was assessed using one-way ANOVA. A value of $p<0.05$ was considered significant.

RESULTS

Wound Healing Activity

Wounds dressed with 5% and 10% *O. stamineus* extracts each or with Intrasite gel® showed considerable signs of dermal healing and significantly ($p<0.05$) healed earlier compared to wounds dressed with blank placebo (Table 1; Figures 2 and 3). There were no significant differences between wounds dressed with 5% or 10% *O. stamineus* extract or Intrasite gel® in terms of rate of wound healing (Table 1). Histologically, wound dressed with *O. stamineus* extracts or Intrasite gel® showed markedly less scar at wound enclosure (Figures 4 and 5) and granulation tissue contained more collagen fibers, fibroblast, proliferating blood capillaries and absence of inflammatory cells compared to wounds dressed with blank placebo which contained less collagen fiber, fibroblast, blood capillaries and more inflammatory cells (Figures 6 and 7).

DISCUSSION

Wound healing may involve regeneration, fibrosis or both. In regeneration, the injured tissue is replaced by the same

Table 1. Time required for wound healing by *O. stamineus* in rats.

Animal groups	No of animals	Type of dressings	Healing time (days) (Mean ± s.e.m)
Group 1	6	Blank placebo	19.83 ± 0.48^{a}
Group 2	6	Placebo containing 5% *O. stamineus*	14.50 ± 0.43^{b}
Group 3	6	Placebo containing 10% *O. stamineus*	13.83 ± 0.31^{b}
Group 4	6	Intrasite gel®	13.33 ± 0.42^{b}

All values were expressed as mean and ± standard error mean. Mean with different superscripts were significantly different (P<0.05)

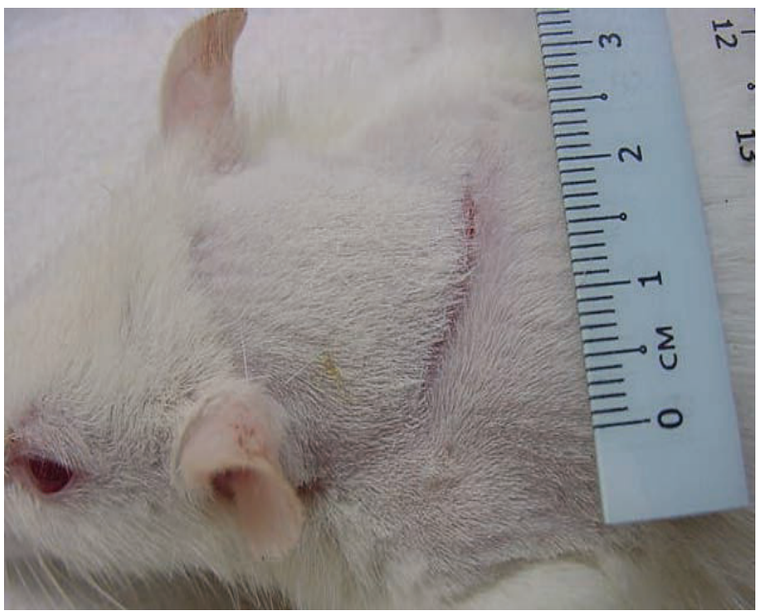

Figure 2. Healing wound dressed with placebo containing 10% *O. stamineus* extract on day 13.

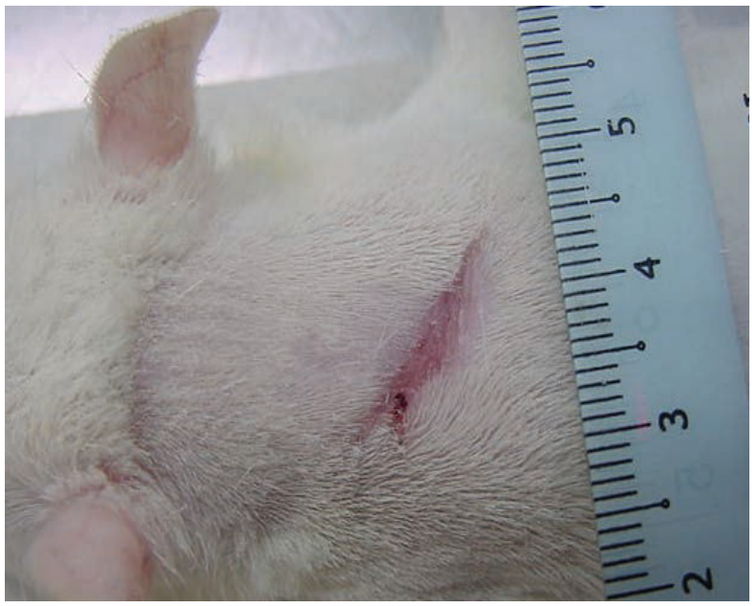

Figure 3. Healing wound dressed with blank placebo on day 19.

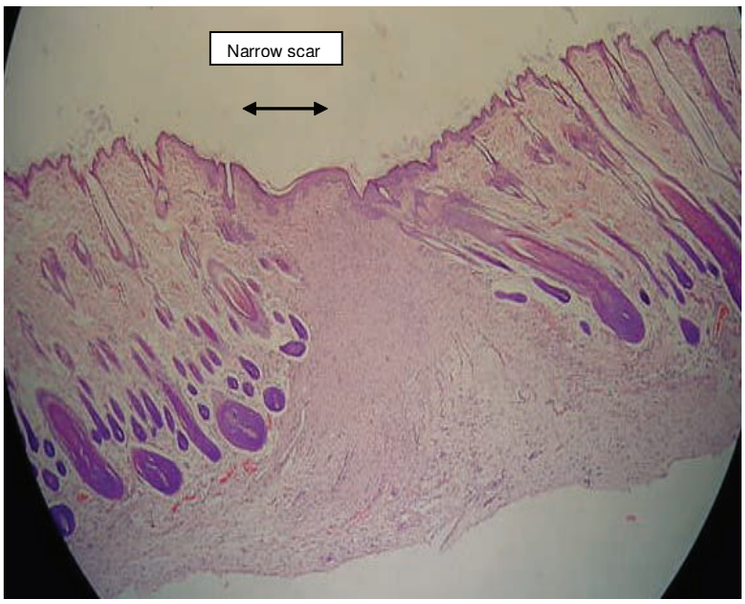

Figure 4. Histological section of healed wound dressed with placebo containing 10% *O. stamineus* showing narrow scar at the wound closure (H & E stain x 10).

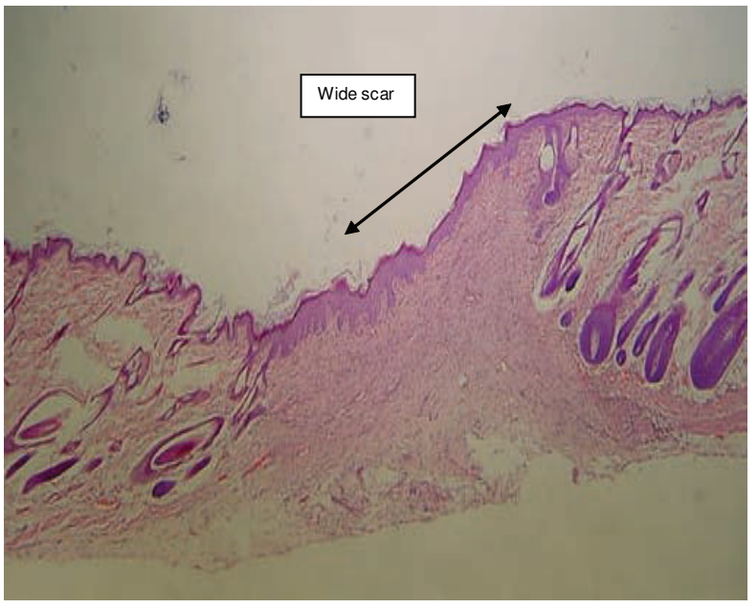

Figure 5. Histological section of healing wound dressed with blank placebo, showing a wide scar at the wound closure (H & E stain × 10).

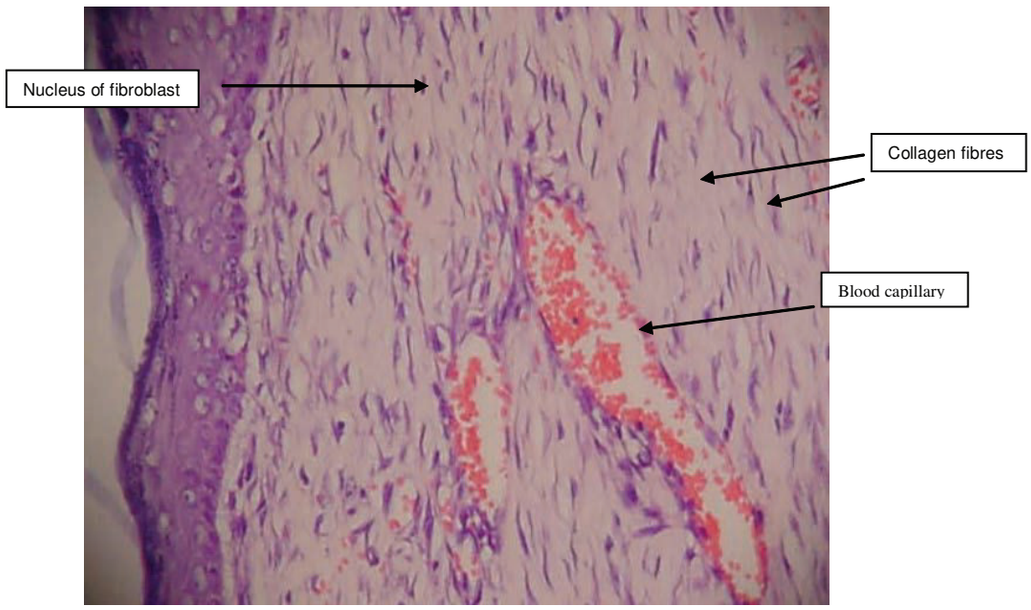

Figure 6. Histological section of healed wound dressed with placebo containing 10% *O. stamineus* extract. Granulation tissue contains more collagen, fibroblast and blood capillaries, and absence of inflammatory cells (H & E stain × 40).

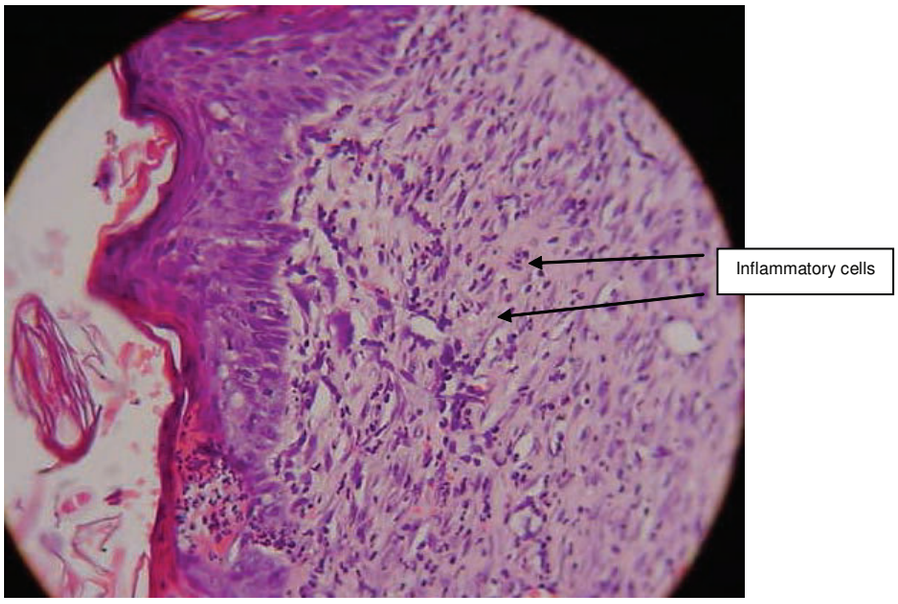

Figure 7. Histological section of healed wound dressed with blank placebo. Granulation tissue contains less collagen, fibroblast blood capillaries and more inflammatory cells (H&E stain × 40).

type of cells. In fibrosis, the wound is repaired with fibrous connective tissue (scar tissue). Epithelia and connective tissue regenerate well. Wound healing has three phases: inflammatory; proliferative and maturational; this depends upon the type and extent of damage, the general state of the host's health and the ability of the tissue to repair. The inflammatory phase is characterized by haemostasis and inflammation, followed by epithelization, angiogenesis and collagen deposition in the proliferative phase. In the maturational phase, the final phase of wound healing, the wound undergoes contraction resulting in a smaller amount of apparent scar tissue. In the present study, topical application of *O. stamineus* extract significantly enhanced the rate of wound healing, and granulation contain more collagen, fibroblast, blood capillaries, and no inflammatory cells. Wound healing effects may be due to up-regulation of human collagen I expression (Bonte *et al*. 1993) and an increase in tensile strength of the wounds (Suguna *et al*. 1996). Enhanced healing activity has been attributed to increased collagen formation and angiogenesis (Trabucchi *et al.* 1986; Shukla *et al.* 1999). Collagen plays a central role in the healing of wounds and it is a principal component of connective tissue and provides a structural framework for the regenerating tissue (Cohen *et al.* 1992). Angiogenesis in granulation tissues improves circulation to the wound site thus providing oxygen and nutrients essential for the healing process (Szabo *et al*. 1995) that include re-epithelization. Stimulated epithelial cell proliferation and angiogenesis are important for the wound healing process (Buntrock *et al*. 1982). Similarly, Habibipour *et al.* (2003) showed that histological analysis of the treated healed wound group contained a large amount of fibroblast proliferation, collagen synthesis and neovascularization which resulted in increased wound tensile strength and accelerated healing wound. Wound healing mechanisms may contribute to stimulate the production of antioxidants in the wound site and provides a favourable environment for tissue healing (Shukla *et al.* 1999). The extract of *O. stamineus* possesses significant antioxidant activity (Olah *et al*. 2003; Akowuah *et al*. 2004; Yam *et al*. 2007). It is likely that the antioxidant property of *O. stamineus* extract could be linked to its wound healing acceleration. Topical applications of compounds with antioxidant properties significantly improves wound healing and protects tissues from oxidative damage (Martin 1996). Yam *et al*. (2007) reported that a protective effect of *O. stamineus* against carbon tetrachloride-induced hepatocellular injury might be attributed to its antioxidant and free radical scavenging property. *O. stamineus* extract are reported to contain flavonoids (Tezuka *et al.* 2000, Olah *et al*. 2003; Yam *et al.* 2007). Flavonoids are known to possess antioxidant activity. It could be conceivable that the *O. stamineus* extract exert their wound healing activity through the flavonoids since flavonoids are reported to improve wound healing and protects tissues from oxidative damage (Saurez *et al*. 1996). In conclusion, the current study revealed that wounds dressed with *O. stamineus* extracts, as topical application on wounds, significantly accelerated the wound healing process and histologically, granulation tissue contained markedly more collagen fibre, fibroblast with proliferating blood capillaries and absence of infilammatory cells.

ACKNOWLEDGMENT

This study was financially supported by the University of Malaya through a grant: 12-02-03-2051 Science Fund RMK-9 Cycle 1/2007.

Date of submission: May 2008
Date of acceptance: June 2009

REFERENCES

Akowuah, AG *et al*. 2004, 'Sinensitin, eupatorin, 3-hydroxy-5, 6, 7, 4-tetremethoxyflavone and rosmatinic acid contents and antioxidative effect of *O. stamineus* from Malaysia', *Food Chemistry*, vol. 87, pp. 569–666.

Awale, S *et al*. 2003, 'Nitric oxide inhibitory isopimarane-type diterpenes from *O. stamineus* of Indonesia', *Journal of Natural Products*, vol. 60, pp. 255–258.

Bonte, F, Dumas, M, Chadgne, C & Meybeck, A 1993, 'Influence of asiatic acid, madecassic acid, and asiaticoside on human collagen I synthesis', *Planta Medica*, vol. 60, pp. 133–135.

Buntrock, P, Jentzsch, KD & Heder, G 1982, 'Stimulation of wound healing. Using brain extract with fibroblast growth factor (FGF) activity. II. Histological and morphometric examination of cells and capillaries', *Experimental Pathology*, vol. 21, no. 1, pp. 62–67.

Cohen, IK, Diegelmann, RF & Lindblad, WJ 1992, '*Wound healing. Biochemical and clinical aspects*', Saunders, Philadelphia.

Fuhrman, B, Lavy, A & Aviram, M 1995, 'Consumption of red wine meal reduces the susceptibility of human plasma and low density lipoprotein to lipid', *American Journal of Clinical Nutrition*, vol. 61, pp. 349–554.

Hegnauer, R 1966, 'Chemotaxonomic der planzen', *Stuggart: Birkhauser Verlag*, vol. 4, pp. 314–316.

Habibipour, S *et al*. 2003, 'Effect of sodium diphenylhydantion on skin wound healing in rats', *Plastic and Reconstructive Surgery*, vol. 112, no. 6, pp. 1620–1627.

Hollman, PC & Katan, MB 1999, 'Dietary flavonoids; intake, health effects and bioavailability', *Food Chemistry Toxicology*, vol. 37, pp. 937–942.

Martin, A 1996, 'The use of antioxidants in healing', *Dermatolic Surgery*, vol. 22, no. 2, pp. 156–160.

Morton, JJ & Molane MH 1972, 'Evaluation of vulnerary activity by an open wound procedure in rats,' *Archives Internationales de Pharmacodynemiie et de Therapie*, vol. 196, no. 1, pp. 117–126.

Olah, NK *et al*. 2003, 'Phytochemical and pharmacological studies on *O. stamineus* Benth (Lamiaceae) hydrochloric extracts', *Journal of Pharmaceutical and Biomedical analysis*, vol. 33, pp. 117–123.

Saurez, J, Herreta, MD & Marhuenda, E 1996, 'Hesperidine and neohesperidine dihydrochalcone on different experimental models of induced gastric ulcer', *Phytotherapy Research*, vol. 10, pp. 616–618.

Shukla, A, Rasik, AM & Dhawan, BN 1999, 'Asiaticoside-induced elevation of antioxidant levels in healing wounds', *Phytotherapy Research*, vol. 13, no. 1, pp. 50–54.

Sriplang, K *et al*. 2007, 'Effects of *O. stamineus* aqueous extract on plasma glucose concentration and lipid profile in normal and streptozotocin-induced diabetic rats', *Journal of Ethnopharnacology*, vol. 109, pp. 510–514.

Szabo, S *et al*. 1995, 'Growth factors: New "endogeneous drug" for ulcer healing', *Scandinavian Journal of Gastroenterology*, vol. 210, pp. 15–18.

Suguna, L, Sivakumar, P & Chandrakasan, G 1996, 'Effects of *Centella asiatica* extract on dermal wound healing in rats', *Indian Journal of Experimental Biology*, vol. 34, pp. 1208–1211.

Tezuka, Y *et al.* S 2000, 'Constituents of the Vietnamese medicinal plant *O. stamineus*', *Chemical Pharmceutical Bulletin*, vol. 48, pp. 1711–1719.

Trabucchi, E *et al*. 1986, 'Topical treatment of experimental skin lesions in rats: macroscopic, microscopic and scanning electron-microscopic evaluation of the healing process', *International Journal of Tissue Reaction*, vol. 8, pp. 533–544.

Wangner, H 1982, 'Parmazietische biologle: drogen und ihre Inhalatsstoffe', 2nd edn, Gustav Fischer Verlag, Stuggart.

Williams, C 1994, 'Intrasite gel: a hydrogel dressing', *British Journal of Nursing*, vol. 3, no. 16, pp. 843–846.

Yam, MF *et al*. 2007, 'Antioxidant and hepatoprotective effects of *O. stamineus* Benth. Standardized extract', *American Journal of Chinese Medicine*, vol. 35, pp. 115–126.

ASM Sci. J., **3(1)**, 59–69

A Low Power 2.4 GHz Variable-gain Low Noise Amplifier for Wireless Applications

L. Lee[1]*, R.M. Sidek[1], S.S. Jamuar[1] and S. Khatun[2]

A 2.4 GHz variable-gain low noise amplifier (VGLNA) intended for use in a Wide-band Code Division Multiple Access receiver was designed in 0.18 um CMOS process for low voltage and low power applications. Rivaling classical designs using voltage mode approach, this design used the current mode approach, utilizing the current mirror principle to obtain a controllable gain range from 8.26 dB to 16.95 dB with good input and output return losses. By varying the current through the widths of transistors and a bias resistor, the VGLNA was capable of exhibiting 8 dB gain tuning range without degrading the noise figure. Therefore, higher gain was possible at lower current and thus at lower power consumption. Total power consumption simulated was 4.63 mW from a 1 V supply and this gave a gain/power quotient of 3.66 dB/mW. Comparing this with available published data, it was observed that this work demonstrated a good gain tuning range and the lowest noise figure with such power consumption.

Key words: current mode; low power applications; noise figure; VGLNA; W-CDMA; amplifier; current mirror

The proliferation of mobile computing has fuelled the demand for portable wireless devices that are of small size, light weight, long battery life and inexpensive (Mohammadi & Salama 2004). Together with the bandwidth and sensitivity limitations, these goals call for circuit and architecture breakthroughs. CMOS technology is by far one of the most important integrated circuit (IC) processing technologies available. Thus the technology can be used for integration of the radio frequency (RF) front-end functions with the digital back-end blocks in a single chip to meet the requirements of having one-chip solution (El-Gamal & Tsang 2002).

The direct conversion receiver (DCR) is a good choice for a Wide-band Code Division Multiple Access (W-CDMA) system because it is well suited for single-chip integration (Razavi 1997). A typical block diagram for a DCR is shown in Figure 1. A DCR includes a pre-select filter, an LNA and a mixer followed by channel-select filters, variable-gain amplifiers and analog to digital converters (ADC). This architecture converts the desired RF signal directly to baseband. There is no need for intermediate frequency (IF) filters, IF amplifiers and the second down-conversion mixers which are necessary for a superheterodyne receiver architecture. Thus, complexity and extra components in the architecture can be reduced.

Based on Figure 1, a low noise amplifier (LNA) is the first circuit in any RF receiver system that handles high dynamic range RF signals and undesirable effects like fading and reflection from an automatic moving object which can saturate or degrade a receiver's performance (Cheng & Jou 2005). Thus, an LNA with gain control can solve these problems, reduce current consumption of the circuit with given linearity and also help to reduce the current consumption of the following blocks such as mixers and filters owing to the reduced linearity requirements (Raja *et al*. 2003). This paper presents the design of a variable-gain low noise amplifier (VGLNA) targeted for 2.4 GHz frequency band. The cascode stage with source-degenerated LNA topology has been connected to a current mirror to give a complete VGLNA design. By using a current mirror, a VGLNA can be designed for high gain with low supply voltage and thus lower power consumption.

VGLNA IN A W-CDMA RECEIVER

Table 1 show the specifications of W-CDMA system which needs to be followed when designing the W-CDMA receiver blocks (Parssinen 2001). As can be seen from the table, the signal bandwidth in a W-CDMA system is adjustable. DCR architecture is suitable for this implementation as the bandwidth of the receiver is determined by the cut-off frequency of the low pass filters in the baseband.

CIRCUIT DESCRIPTIONS

A LNA design in W-CDMA receiver demands good performance with tradeoffs between noise figure (NF),

[1]Department of Electrical and Electronic Engineering, University Putra Malaysia, 43400, Serdang, Malaysia
[2]Department of Computer and Communication System Engineering, University Putra Malaysia, 43400, Serdang, Malaysia
* Corresponding author (e-mail: linilee@gmail.com)

Table 1. W-CDMA specifications (Parssinen 2001).

Receiver frequency bands:	
Base station	1920–1980 MHz
Mobile unit	2110–2170 MHz
Channel spacing	5 MHz, 10 MHz, 20 MHz
Chip rate (signal bandwidth)	3.84, 8.192, 16.384 Mcps
Data rates:	
Outdoors	8-384 kb/s (speech 12.2 kb/s)
Indoors	Up to 2 Mb/s
Modulation scheme	QPSK
Multiple access technique	DS-CDMA
Sensitivity	–117 dBm
Duplexing	Frequency Division Duplexing

gain, input-referred third-order intercept point (IIP3) and power consumption. A good input match is critical when a pre-select filter precedes the LNA, as such filters are often sensitive to the quality of the termination. The low power consumption required on portable systems further complicates the design process. To develop a design strategy that balances gain, input impedance, noise figure and power consumption is a great challenge to designers.

Cascode Stage with Source-degenerated LNA

For the cascode structure, the inductive source degeneration topology was adopted in order to obtain the best NF (Lee 1998). Referring to Figure 2, the inductively degenerated common source (CS) input consists of transconductors, M1 – M2 and gate and source inductors; L_s and L_g, respectively. Both M1 and M2 are in common-source configuration, similar to a cascaded amplifier. The cascaded M2 can help reduce the Miller's effect of M1 as well as improve the reverse isolation effect. The gate width and the bias current of the transistors were chosen to maximize the transconductance while maintaining low power requirement. The inductor Ls had the benefit of simultaneously achieving both input and noise matching.

For simplification of analysis, the input impedance, Z_{in} can be written as:

$$Z_{in} = s(L_s + L_g) + \frac{1}{sC_{gs}} + \left(\frac{g_m}{C_{gs}}\right)L_s \quad (1)$$

where g_m is the device transconductance and C_{gs} is the gate-to-source capacitance. Using this topology, a controllable real term at the input impedance R_{in} can be generated as

$$R_{in} = \left(\frac{g_m}{C_{gs}}\right)L_s \approx \omega_T L_s \quad (2)$$

where ω_T represents the transition frequency. At the frequency of operation, a value of L_s can be chosen in order for the real term to be made equal to 50 Ω. Thus maximum signal is delivered with the gain optimized. For the power matched at resonance, the real part of input impedance needs to be equalled to source resistance.

Noise Optimization

The standard CMOS noise model is shown in Figure 3. The dominant noise source in CMOS devices is channel thermal noise and it is commonly modelled as a shunt current source in the output circuit of the device (Shaeffer & Lee 1997). The channel noise is white with a spectral density given by

$$\frac{\overline{i_d^2}}{\Delta f} = 4kT\gamma g_{do} \quad (3)$$

where $\overline{i_g^2}$ represents the channel thermal noise of the device, g_{do} is the device zero-bias drain conductance, γ is a bias-dependent factor and Δf is the noise bandwidth. The noise figure of the LNA can be computed by analyzing the circuit shown in Figure 4. R_l represents the series resistance of L_g and R_g is the gate resistance of the NMOS. The noise figure contributed by the subsequent stages is neglected as long as the first stage possesses sufficient gain. Overlap capacitance, C_{gd} has also been neglected and this approximation is accepted since this is a cascaded structure.

The transconductance of the input stage needs to be evaluated first in order to evaluate the output noise when the amplifier is driven by a 50 Ω source. At resonance, the transconductance G_m is expressed as:

$$G_m = g_{m1}Q_{in} = \frac{g_{m1}}{\omega_o C_{gs}(R_s + \omega_T L_s)} = \frac{\omega_T}{\omega_o R_s\left(1 + \frac{\omega_T L_s}{R_s}\right)} \quad (4)$$

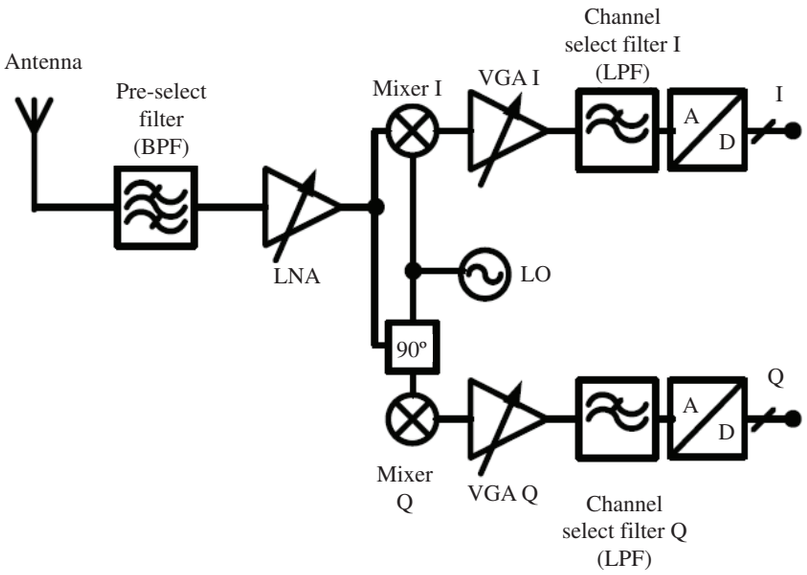

Figure 1. Block diagram of the Direct Conversion Receiver (DCR) architecture.

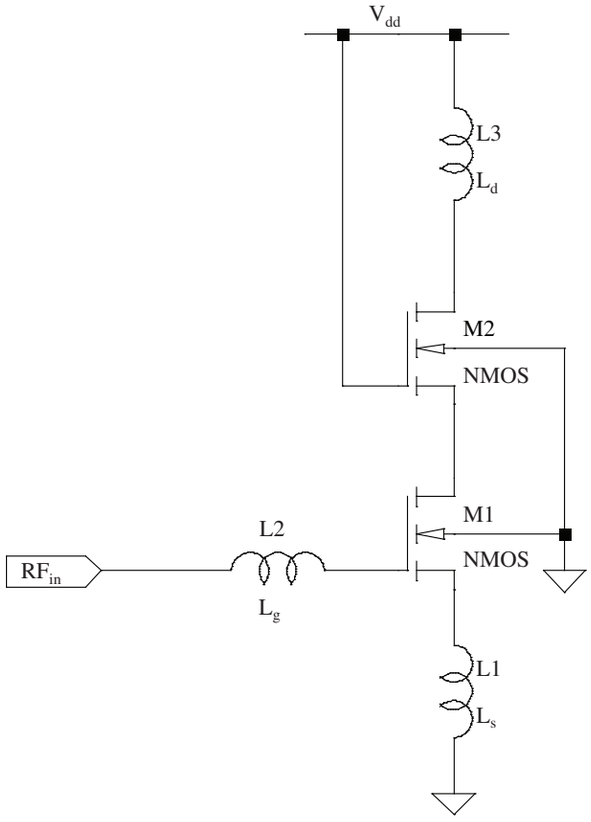

Figure 2. Cascode low noise amplifier (LNA) with inductive source degeneration structure.

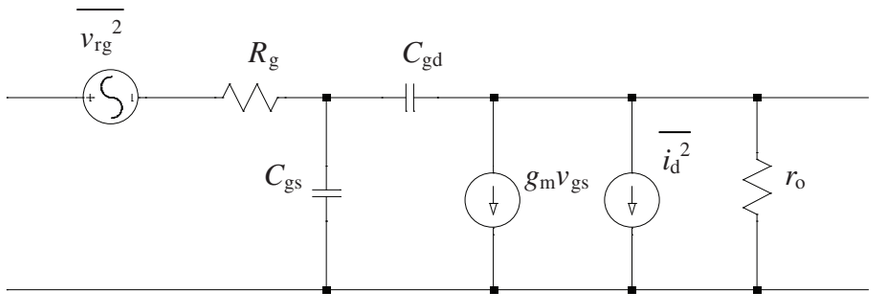

Figure 3: The standard CMOS noise model.

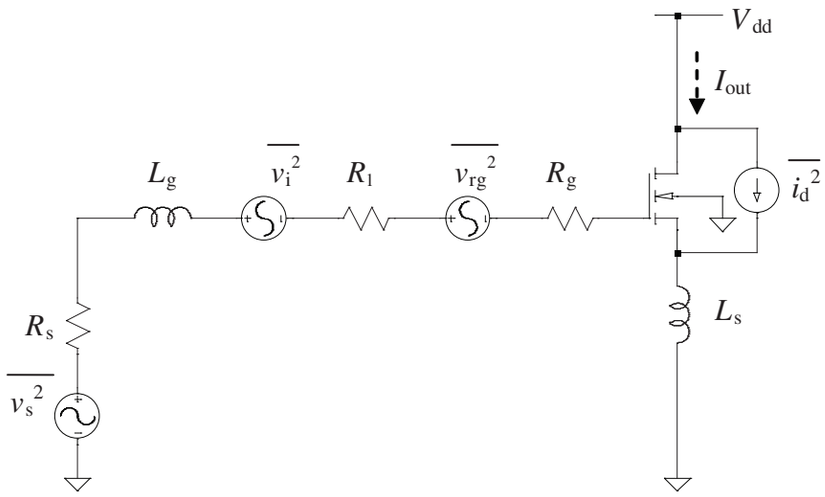

Figure 4: Equivalent circuit for input stage noise calculations of a standard CMOS.

where Q_{in} is the effective Q of the amplifier input circuit, ω_o is the operating frequency and ω_T is the transition frequency. The well-known noise factor is given as:

$$F = \frac{\text{Total output noise power}}{\text{Total output noise due to the source}} \tag{5}$$

Using Equation 4, the output noise power density due to the 50 Ω source is:

$$S_{source}(\omega_o) = S_{src}(\omega_o) G_{m,eff}^2 = \frac{4kTR_s\omega_T^{\ 2}}{\omega_o^2 R_s^2\left(1+\frac{\omega_T L_s}{R_s}\right)^2} \tag{6}$$

In a similar manner, the output noise power density due to R_l and R_g can be expressed as:

$$S_{Rl\_and\_Rg}(\omega_o) = \frac{4kT(R_l+R_g)\omega_T^{\ 2}}{\omega_o^2 R_s^2\left(1+\frac{\omega_T L_s}{R_s}\right)^2} \tag{7}$$

The dominant noise contributor internal to the LNA is the channel current noise of the first MOS device. Thus from Equation 3, the output noise power density arise from this source can be derived as:

$$S_{id}(\omega_o) = \frac{\frac{\overline{i_d^2}}{\Delta f}}{\left(1+\frac{\omega_T L_s}{R_s}\right)^2} = \frac{4kT\gamma g_{do}}{\left(1+\frac{\omega_T L_s}{R_s}\right)^2} \tag{8}$$

Recalling Equation 5, the output noise power is the sum of Equations 6–8. Therefore, substituting these into Equation 5 gives:

$$F = 1 + \frac{R_l}{R_s} + \frac{R_g}{R_s} + \gamma g_{do} R_s \left(\frac{\omega_o}{\omega_T}\right)^2 \tag{9}$$

This Equation 9 for noise factor reveals an important feature of this LNA architecture; the channel thermal noise g_{do} is proportional to the noise factor. So, by reducing g_{do} without modifying ω_T, the noise figure can be improved and power dissipation reduced simultaneously. Thus, desirable result can be achieved by scaling the width of the device while maintaining constant bias voltage and keeping the channel length unchanged. This scaling is consistent with the proposed variable gain stage which would be introduced later (VGLNA Circuit).

A more precise noise model including induced gate current noise has been included in the MOS model as shown in Figure 5. A shunt noise current $\overline{i_g^2}$ and a shunt conductance g_g had been added and the induced noise can be expressed as:

$$\frac{\overline{i_g^2}}{\Delta f} = 4kT\delta g_g \tag{10}$$

where δ is the coefficient of gate noise. The gate noise is partially correlated with drain noise, with a correlation coefficient given by:

$$c = \frac{\overline{i_g i_d^*}}{\sqrt{\overline{i_g^2}\,\overline{i_d^2}}} \approx 0.395j \tag{11}$$

The value 0.395_j is given for long-channel devices. The gate noise can be re-expressed as the sum of two components, the first which is uncorrelated with the drain noise and the second which is correlated with the drain noise respectively, as shown here:

$$\frac{\overline{i_g^2}}{\Delta f} = 4kT\delta g_g \left(1 - |c|^2\right) + 4kT\delta g_g |c|^2 \tag{12}$$

Hence, the output noise power density in Equation 3 would have to be revised to include the induced noise current, resulting in:

$$S_{id,ig\_cor}(\omega_o) = \kappa S_{id}(\omega_o) = \frac{4kT\gamma\kappa g_{do}}{\left(1 + \frac{\omega_T L_s}{R_s}\right)^2} \tag{13}$$

where,

$$\kappa = \frac{\delta\alpha^2}{5\gamma}|c|^2 + \left[1 + |c|Q_L\sqrt{\frac{\delta\alpha^2}{5\gamma}}\right]^2 \tag{14}$$

with,

$$Q_L = \frac{1}{\omega_o R_s C_{gs}} \tag{15}$$

and,

$$\alpha = \frac{g_m}{g_{do}} \tag{16}$$

The uncorrelated portion of gate noise can be written as:

$$S_{ig\_uncor}(\omega_o) = \xi S_{id}(\omega_o) = \frac{4kT\gamma\xi g_{do}}{\left(1 + \frac{\omega_T L_s}{R_s}\right)^2} \tag{17}$$

where,

$$\xi = \frac{\delta\alpha^2}{5\gamma}\left(1 - |c|^2\right)\left(1 + Q_L^2\right) \tag{18}$$

Combining all the noise terms of Equation 8, Equation 13 and Equation 17, the channel current noise contributed by M1 is given as:

$$S_{M1}(\omega_o) = \chi S_{id}(\omega_o) = \frac{4kT\gamma\chi g_{do}}{\left(1 + \frac{\omega_T L_s}{R_s}\right)^2} \tag{19}$$

where,

$$\chi = \kappa + \xi = 1 + 2|c|Q_L\sqrt{\frac{\delta\alpha^2}{5\gamma}} + \frac{\delta\alpha^2}{5\gamma}\left(1 + Q_L^2\right) \tag{20}$$

It follows directly that Equation 9 would have to be re-expressed as:

$$F = 1 + \frac{R_l}{R_s} + \frac{R_g}{R_s} + \gamma\chi g_{do} R_s \left(\frac{\omega_o}{\omega_T}\right)^2 \tag{21}$$

and it can be simplified to:

$$F = 1 + \frac{R_l}{R_s} + \frac{R_g}{R_s} + \frac{\gamma}{\alpha}\frac{\chi}{Q_L}\left(\frac{\omega_o}{\omega_T}\right) \tag{22}$$

in which:

$$g_{do} Q_L = \frac{g_m}{\alpha}\frac{1}{\omega_o R_s C_{gs}} = \frac{\omega_T}{\alpha\omega_o R_s} \tag{23}$$

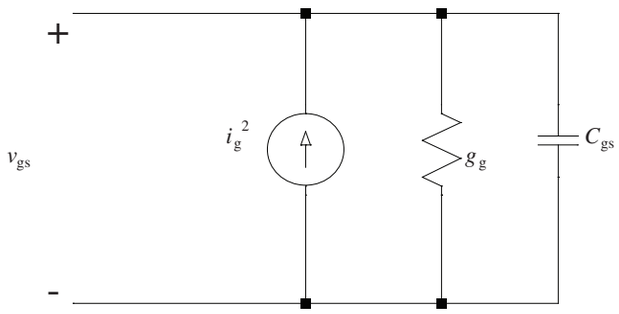

Figure 5. Gate circuit model including induced effects.

Power Constrained Noise Optimization

With the relevance quantities defined, optimization of the noise performance of the amplifier can be done. There are two approaches to this optimization where the first assumes a fixed transconductance, G_m of the amplifier and the second is fixed power consumption. In this paper, the second approach is being used and this approach takes the expression of F in Equation 22 to make it depend on power dissipation (P_D).

Recalling a simple expression for the drain current (Shaeffer & Lee 1997),

$$I_D = \frac{\mu_n C_{ox}}{2}\frac{W}{L}(V_{gs}-V_t)\left[(V_{gs}-V_t)\,\|\,(LE_{sat})\right] = WLC_{ox}\nu_{sat}E_{sat}\frac{\rho^2}{1+\rho} \quad (24)$$

where C_{ox} is the gate oxide capacitance per unit area and E_{sat} is the velocity saturation field strength. Thus, the power dissipation can be written as:

$$P_D = V_{DD}I_D = V_{DD}WLC_{ox}v_{sat}E_{sat}\frac{\rho^2}{1+\rho} \quad (25)$$

with,

$$\rho = \frac{V_{gs}-V_t}{LE_{sat}} = \frac{V_{od}}{LE_{sat}} \quad (26)$$

and,

$$\nu_{sat} = \frac{\mu_n}{2}E_{sat} \quad (27)$$

Differentiating the Equation 24 to determine the transconductance, yields:

$$g_m = \frac{\partial I_d}{\partial V_{gs}} = \mu_n C_{ox}\frac{W}{L}V_{od}\left[\frac{1+\rho/2}{(1+\rho)^2}\right] \quad (28)$$

Substituting Equation 24 into the equation for Q_L in Equation 15 gives:

$$Q_s = \frac{P_o}{P_D}\frac{\rho^2}{1+\rho} \quad (29)$$

where,

$$P_o = \frac{3}{2}\frac{V_{DD}\nu_{sat}E_{sat}}{\omega R_s} \quad (30)$$

Another factor required is ω_T, and this can be evaluated with Equation 28 to be:

$$\omega_T \approx \frac{g_m}{C_{gs}} = \frac{g_m}{\frac{2}{3}WLC_{ox}} = \frac{3}{2}\frac{\alpha\mu_n V_{od}}{L^2} = \frac{3\alpha\rho\nu_{sat}}{L} \quad (31)$$

From Equations 28–29 and 31, substituting them into Equation 22 in terms of the relative gate overdrive, ρ and this gives:

$$F = 1+\frac{\gamma\omega_o L}{3\nu_{sat}}P(\rho,P_D) \quad (32)$$

which the gate resistance and inductor losses have been neglected. Assuming $\rho << 1$, then $P(\rho,P_D)$ can be simplified and the minimum noise figure occurs when:

$$\rho^2 \approx \frac{P_D}{P_o}\sqrt{\frac{\delta}{5\gamma}(1-|c|^2)}\left[1+\sqrt{\frac{7}{4}}\right] \quad (33)$$

Substituting Equation 33 into Equation 29 yields the value of Q_L that leads to the power constrained minimum noise figure as:

$$Q_{\mathrm{L,opt,P_D}} = |c|\sqrt{\frac{5\gamma}{\delta}}\left[1+\sqrt{1+\frac{3}{|c|^2}\left(1+\frac{\delta}{5\gamma}\right)}\right] \approx 3.9 \quad (34)$$

with $\gamma = 2.5$, $\delta = 5.0$, $|c| = 0.395$. From Equations 15 and 31:

$$Q_{\mathrm{L}} = \frac{1}{\omega C_{\mathrm{gs}} R_{\mathrm{s}}} = \frac{1}{\omega\left(\frac{2}{3}WLC_{\mathrm{ox}}\right)R_{\mathrm{s}}} \quad (35)$$

Once Q_{L} has been determined, the expression for the width of the optimum device can be calculated as:

$$W_{\mathrm{opt,P_D}} = \frac{3}{2}\frac{1}{\omega L C_{\mathrm{ox}} R_{\mathrm{s}} Q_{\mathrm{L,opt,P_D}}} \quad (36)$$

Variable Gain Stage with Current Mirror

The proposed variable gain feature of a current mirror in a LNA circuit is shown in Figure 6. In contrast to the conventional gain-controlled LNA (Tsang & El-Gamal 2002; Liao & Chuang 2003; Raja *et al.* 2003, Wang & Lu 2005), this VGLNA employs a current mirror for the function of a variable gain. The current mirror constructed from transistors M3 and M4, is employed with a bias resistor R_{bias} and bias voltage V_{b}. Voltage signal from the drain terminal of M2 or low noise stage is fed into the common source terminal of the transistors, M3 and M4. The current mirror built from M3 and M4 uses the principle that if the gate-source potential of two identical MOS transistors is equalled, the channel currents should be equalled.

The key property of a current mirror is to allow precise copying of the current with no dependence on process and temperature. Thus, the current I_3 is controlled by R_{bias} and V_{b};

$$I_3 = \frac{V_{\mathrm{b}}}{R_{\mathrm{bias}}} \quad (37)$$

with I_4 as the output or 'mirrored' current. With M3 and M4 in saturation, the gain of the VGLNA can be defined as the ratio of I_4 to I_3 and it can be expressed as:

$$A_{\mathrm{i}} = \frac{I_4}{I_3} = \left(\frac{L_3W_4}{W_3L_4}\right)\left(\frac{V_{\mathrm{GS}}-V_{\mathrm{T4}}}{V_{\mathrm{GS}}-V_{\mathrm{T3}}}\right)^2\left[\frac{1+\lambda v_{\mathrm{DS4}}}{1+\lambda v_{\mathrm{DS3}}}\left(\frac{K_4'}{K_3'}\right)\right] \quad (38)$$

where $W_{3,4}$, $L_{3,4}$, $VT_{3,4}$, $v_{\mathrm{DS3,4}}$ and $K'_{3,4}$ represents the width, length, threshold voltage, drain-to-source voltage and the conduction factor of the transistors M3 and M4 respectively, V_{GS} is gate-to-source voltage and λ is channel length modulation. With the components of a current mirror processed on the same integrated circuit, all the physical parameters are identical for both devices. With $v_{\mathrm{DS3}} = v_{\mathrm{DS4}}$, the ratio of I_4 to I_3 is shown to be influenced mainly by the width of the transistors; $W_{3,4}$. Based on Equation 38, the gain of VGLNA is a function that can be easily controlled. If $v_{\mathrm{DS3}} \neq v_{\mathrm{DS4}}$ and the physical parameters are not identical for the devices, there is a minimum deviation from the ideal

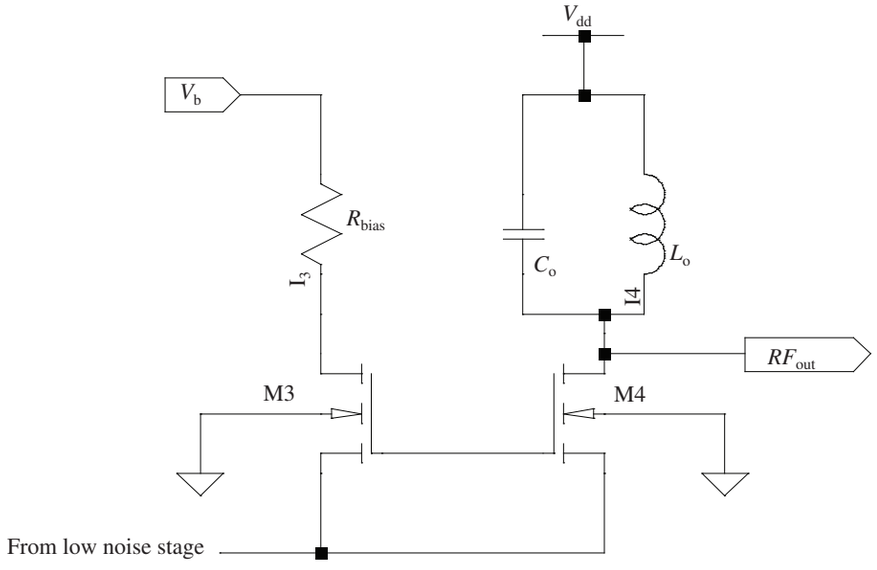

Figure 6. Variable gain stage constructed from a current mirror (M3 and M4) for VGLNA.

current mirror gain. Nevertheless, the design is optimized with consideration for the deviation to appear insignificant. Referring to Equation 38, the length of the transistors are assumed to be equal and as W_3 decreases, I_3 decreases and this gives higher gain. As a result, it is shown that a higher gain is possible at lower current and thus at a lower power dissipation. Therefore a VGLNA which consumes low power consumption can be obtained.

On the implementation side, the various widths of transistors can be implemented by using multiple transistors with different widths or multiple resistors with different values. This would produce multiple currents of I_3 which would influence the gain of the VGLNA.

VGLNA CIRCUIT

The schematic diagram of the proposed VGLNA is shown in Figure 7. The values of the components are as follows: L_g=5.68 nH, L_s=1.4 nH, L_d=5.27 nH, L_o=0.45 nH, C_o=1.15 pF, $W_{1,2}$=225 µm, $W_{3,4}$ ranging from 630 µm to 1056 µm. The coupling capacitors and the biasing circuitries are not shown in the diagram.

SIMULATION RESULTS

The VGLNA was simulated, targeting 2.4 GHz using 0.18 um CMOS process. The VGLNA exhibited gain, S21 centred at 2.4 GHz with a controllable range from 8.27 dB to 16.95 dB and it consumed 4.63 mW from a 1 V supply. The gains of the VGLNA are shown in Figure 8 with two modes. With the current mirror as variable gain stage, the gain over power quotient which was frequently used as a figure of merit for low power design was calculated to be 3.66 dB/mW. Changes at the gain did not degrade the noise performance of the circuit since the circuit was constructed from two different stages. As shown in Figure 9, the noise figure (NF) equalled to 1.05 dB. The input and output reflection coefficients were –27.40 dB and –22.98 dB, respectively, as shown in Figure 10. This showed that the VGLNA was able to provide enough attenuation to the LO leakage. In terms of linearity fulfilment, the input-referred third order intercept point (IIP3) was –1.39 dBm with the gain optimized. This showed that the current mirror introduced for variable gain in the VGLNA design reduced the current consumption of the circuit without sacrificing linearity.

Table 2 showed the summary of this work and comparison with published data of several LNAs designed in CMOS process. It was observed that this work demonstrated the lowest noise figure (NF) with a power consumption of 4.63 mW.

CONCLUSION

This work demonstrated a variable gain low noise amplifier (VGLNA) in a 0.18 um CMOS process which was suitable for use as a first amplifier in Bluetooth application. As the CMOS process keeps progressing to smaller channel

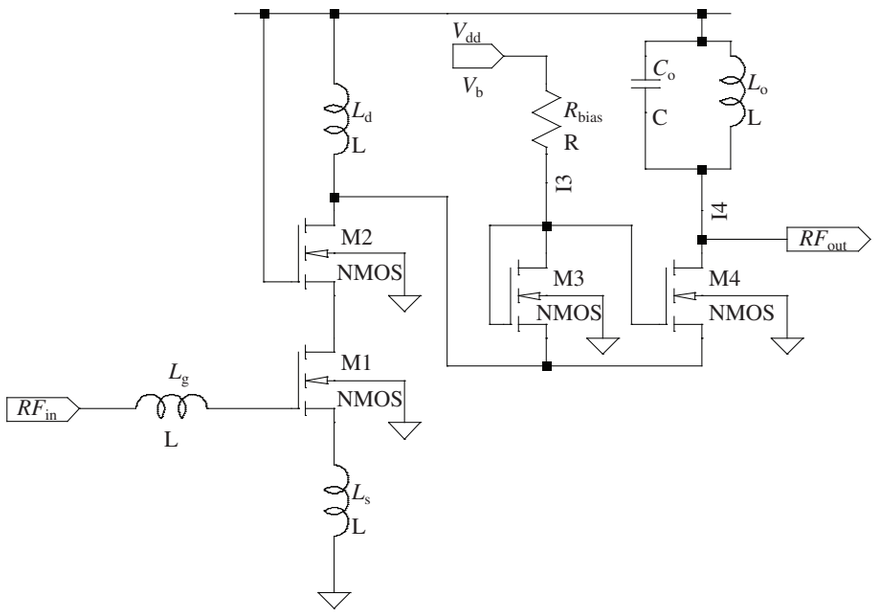

Figure 7. Schematic diagram of the proposed VGLNA.

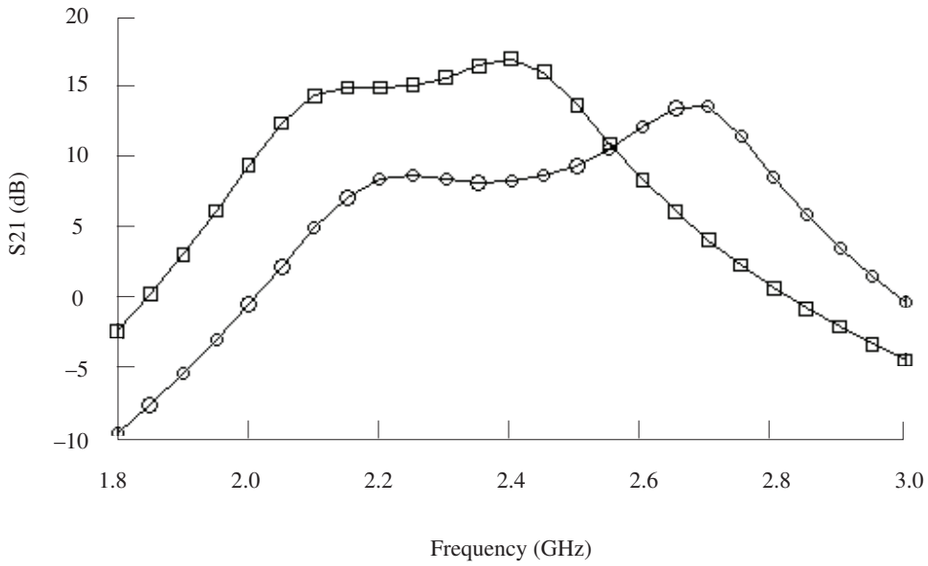

Figure 8. Power gain, S21 of the proposed VGLNA.

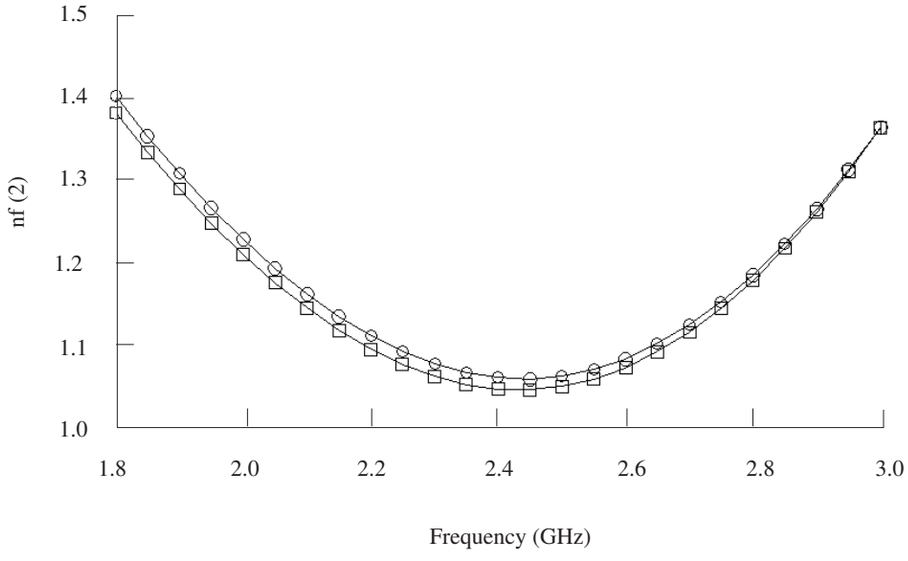

Figure 9. Noise figure of the proposed VGLNA in low and high gain modes.

lengths driven by the digital circuitry, the performance of the circuits would continue to improve as well. Theoretical analysis of the amplifier architecture demonstrated the fundamental role of induced gate noise as well as in designing a power constrained noise optimization design. This VGLNA exhibited 16.95 dB gain, 1.05 dB NF and approximately 8 dB gain tuning range while dissipating 4.63 mW from a 1 V supply. The proposed VGLNA offers a compromise between gain, noise factor and power consumption. Its versatility offers further deployment in circuits and architecture breakthrough especially in the wireless applications.

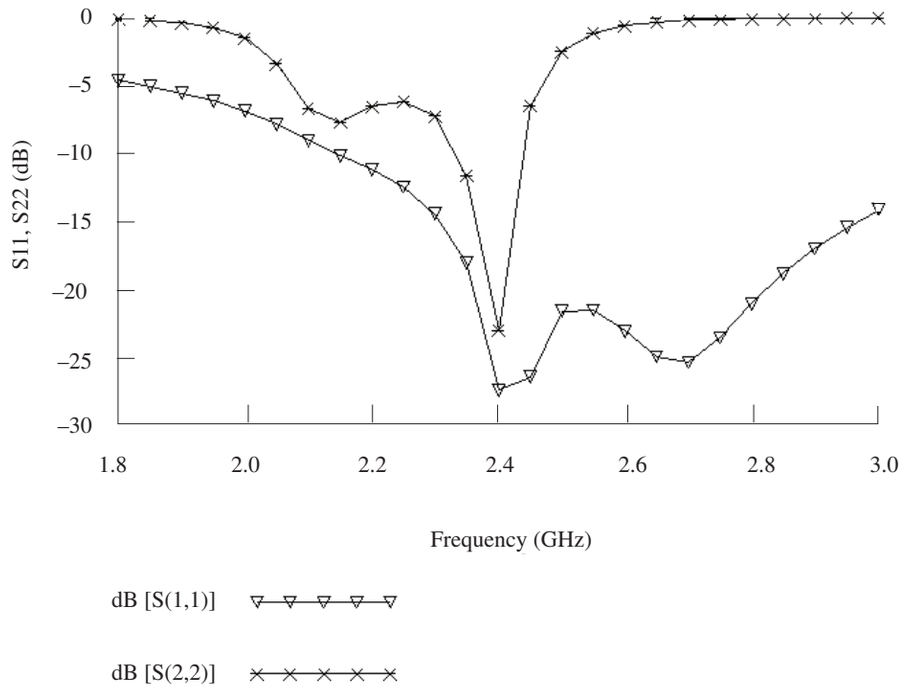

Figure 10. S11 and S22 of the proposed VGLNA.

Table 2. Comparison of proposed VGLNA with VGLNAs published.

Process (um)	Frequency (GHz)	V_{DD} (V)	Gain (dB)	Gain variation (dB)	NF (dB)	P_{dc} (mW)	Gain/P_{dc} (dB/mW)	Reference
0.18	2.40	1.0	16.95	8.0	1.05	4.63	3.66	This work
0.18	5.80	1.0	13.20	10.0	2.50	22.20	0.49	(Tsang & El-Gamal 2002)
0.18	2.40	1.8	15.20	11.0	1.55	4.50	3.38	(Cheng & Jou 2005)
0.18	5.75	1.8	21.00	10.5	4.40	22.20	0.95	(Raja *et al.* 2003)
0.18	5.70	1.0	16.40	8.0	3.50	3.20	5.12	(Wang & Lu 2005)

ACKNOWLEDGEMENTS

This research was supported by Silterra Malaysia Sdn. Bhd and Ministry of Science, Technology and Innovation (MOSTI) of Malaysia through the National Science Fellowship (NSF).

Date of submission: September 2008
Date of acceptance: August 2009

REFERENCES

Allen, PE and Holberg, DR 2002, *CMOS analog circuit design*, Oxford University Press, USA.

Cheng, KH and Jou, CF 2005, 'A novel 2.4 GHz LNA with digital gain control using 0.18/spl um/m CMOS,' in *Asia-Pacific Microwave Conference Proceedings 2005*, vol. 2, pp. 4–7.

Lee, TH 1998, *The design of CMOS radio frequency integrated circuit*, Cambridge University Press, Cambridge.

Liao, CH and Chuang, HR 2003, 'A 5.7-GHz 0.18-um CMOS gain-controlled differential LNA with current reuse for WLAN receiver,' *IEEE Microwave and Wireless Components Letter*, vol. 13, pp. 526–528.

Mohammadi, B & Salama, CAT 2004, 'A 5.8 GHz CMOS LNA for WLAN applications,' in *IEEE Radio Frequency Integrated Circuits (RFIC) Symposium, June 2004*, pp. 113–116.

Parssinen, A 2001, *Direct conversion receiver in wide-band systems*, Kluwer Academic Publishers, USA.

Raja, MK, Boon, TTC, Kumar, KN & Wong, SJ 2003, 'A fully integrated variable gain 5.75-GHz LNA with on chip active Balun for WLAN,' in *IEEE Radio Frequency Integrated Circuits Symposium*, pp. 439–442.

Razavi, B 1997, 'Design considerations for direct-conversion receivers,' *IEEE Transactions on Circuits and Systems II*, vol. 44, pp. 428–435.

Shaeffer, DK & Lee, TH 1997, 'A 1.5-V, 1.5-GHz CMOS low noise amplifier,' *IEEE Journal of Solid-State Circuits*, vol. 32, pp. 745–759.

Tsang TKK & El-Gamal, MN 2002, 'Gain controllable very low voltage sub-1 V 5.8 GHz CMOS LNA,' in *IEEE International Symposium on Circuits and Systems*, vol. 4, pp. 795–798.

Wang, YS & Lu, LH 2005, '5.7 GHz low power variable-gain LNA in 0.18 um CMOS,' *Electronics Letters*, vol. 41, pp. 66–68.

ASM Sci. J., **3(1)**, 71–76

Evaluation of Closed Vessel Microwave Digestion of Fish Muscle with Various Solvent Combinations Using Fractional Factorial Design

K.H. Low[1]*, S.M. Zain[1], M.R. Abas[1] and M. Ali Mohd[2]

Fractional factorial design was utilized to evaluate the effect of combinations of nitric acid, hydrogen peroxide, hydrochloric acid and water for microwave digestion of fish muscle. Upon digestion, copper, iron and zinc were determined by flame atomic absorption spectroscopy. H_2O_2 and HCl volumes were found to be the most significant parameters which resulted in good metal recoveries. This is especially so for the effect of HCl on Fe recovery. The results indicated that the combination of 4 mL 65% HNO_3, 2 mL 30% H_2O_2 and 2 mL 30% HCl gave the most satisfactory percentage recovery. There was good agreement between measured and certified values for all metals with respect to the DORM-3 fish protein.

Key words: AAS; chemometric, fish muscle; metal; microwave digestion; fractional factorial design; HNO_3

Elemental analysis of metals is usually necessary in order to study human health, environmental, geochemical and industrial issues (Vandercasteele & Block 1993). The effects of these elements on human health are of great interest nowadays, especially for consumable aquatic products because once toxic metals reach human beings they may produce chronic and acute illnesses (Reis & Almeida 2008).

Uluozlu *et al*. 2007 reported that metals could be possibly classified as potentially toxic (arsenic, cadmium, lead, mercury, etc.), probably essential (cobalt, nickel, vanadium) and essential (copper, iron, manganese, zinc). The toxic elements can be very harmful even at low concentrations if ingested over a long period of time. On the other hand, essential metals could produce toxic effects if their intake was excessive (Celik & Oehlenschlager 2007). As a result, it is not surprising that numerous studies have been carried out on metal accumulation in different fish species, as fish forms a major part of human diet (Türkmen 2005).

Quantification of metals in organic matter like fish is most often accomplished via atomic absorption spectroscopy (AAS). This generally requires destruction of the sample matrix to produce a solution of the analyte for analysis. The decomposition of the sample is a critical step as it will definitely have crucial effects on the final results. Therefore it has to be assured that there is total decomposition of the sample, with no significant loss of the metals throughout the process. There is a wide range of sample decomposition methods for aquatic products that have been published, such as dry ashing, wet ashing with different mixtures of reagents or conventional heating procedures, microwave dissolution and acid bomb digestion (Reis *et al.* 2008; Hseu 2004; Tüzen 2003 & Sures *et al*. 1995). These methods generally show both good accuracy and precision. However, the conventional wet and dry ashing digestion procedures are, to a certain extent rather time consuming.

The most commonly used method nowadays is microwave digestion which has been the method of choice that has offered many advantages over conventional digestion procedures in both time and recovery aspects. At present, a large number of methods are recommended for the preparation of aquatic samples via microwave assisted digestion with the addition of other reagents besides nitric acid (HNO_3) prior to digestion of aquatic products (Hamilton *et al*. 2007; Mendil & Uluözlü 2007; Manutsewee *et al.* 2007; Retief *et al.* 2006; Scancar *et al*. 2004). The addition of other reagents with HNO_3 prior to digestion may permit more complete oxidation of organic sample matter, address specific decomposition of required chemicals, or address specific elemental stability and solubility problems (*EPA Method 3052, 1996*). Microwave extraction using diluted acids in a closed high-pressure vessel at temperatures above the boiling point of these acids is a simple alternative sample preparation and its use is growing. Diluted mineral acid solutions can absorb microwave energy more intensely owing to their water content. These features reduce acid consumption, contamination, and preparation time (Soylak *et al.* 2007). However, these may well cause limitation to the technique or increase the complexity of analysis.

[1] Environmental Research Group, Department of Chemistry, Faculty of Science, University of Malaya, 50603 Kuala Lumpur
[2] Department of Pharmacology, Faculty of Medicine, University of Malaya, 50603 Kuala Lumpur
* Corresponding author (e-mail: lowkayin@um.edu.my)

Therefore, a number of factors should be considered in order to carry out microwave assisted acid digestion for desired targets.

There are several methods that can be applied for studying the main effects of addition of other reagents to HNO_3 prior to microwave digestion. However, traditional univariate approaches that study each variable separately are rather time-consuming and not economical compared to the more encouraged chemometric tools which allow more than one variable to be studied simultaneously (Jalbani *et al*. 2006). Furthermore, multivariate approaches make possible the understanding of circumstances that are not explainable in a traditional manner, for example, the interaction between factors that influence analytical responses (Cerutti *et al*. 2004).

This paper describes the use of fractional factorial design for the preliminary evaluation of the effect and significance of adding other reagents with HNO_3 prior to microwave digestion. In this design, a subset of a full factorial design was selected in a way that still rendered the possibility of estimating the desired main effects and some interactions from a limited number of experiments.

EXPERIMENTAL

Instrumentation

A GBC 933AA flame atomic absorption spectrometer (FAAS) equipped with a D_2 lamp for background correction was used for the analysis. Copper (Cu), iron (Fe) and zinc (Zn) hollow cathode lamps were run under operational conditions suggested by the manufacturer. These conditions are shown in Table 1. All measurements were performed using an air-acetylene flame with optimized flow rates.

The microwave digestions were carried out in a CEM MarXpress Microwave Accelerated Reaction System (CEM Corporation, Matthews, NC, USA). In this study, 0.50 g of sample were weighed into 55 ml self-regulating pressure control PFA® polymer digestion vessels equipped with TFM® vent plugs and PFA® Teflon® liners. Digestion was performed in temperature-controlled mode using HNO_3 with the addition of other reagents as designed (Tables 2 and 3). Microwave power was 800 W and temperature was programmed to ramp till 200ºC in 15 min and to hold for 15 min. Replicates and sample blank were also included in the same digestion circle.

Reagents and Standard Materials

All chemicals used in this work were of analytical grade. Deionized (DI) water was obtained from ELGA® *PURELAB® UHQ II* system (>18 MΩ cm^{-1} resistance). 65% HNO_3, 30% HCl and 30% H_2O_2 solution were of Suprapur® quality from Merck (Darmstadt, Germany). All the apparatus were cleaned by overnight soaking in 10% HNO_3, then soaked and rinsed with DI water consequently prior to use.

Cu, Fe and Zn calibration solutions were prepared by appropriate dilution of 1000 mgL^{-1} CertiPUR® standard solutions (Merck) with 0.5 $molL^{-1}$ HNO_3 solution. Verification was carried out using certified fish protein reference material for trace metals (DORM-3) from National Research Council Canada (Ottawa, Ontario, Canada), which had been vacuum dried and sieved through 297 µm screen, blended and amber bottled.

Experimental Design

The chemometric study was conducted using a two-level fractional factorial design (FFD) including centre samples. In FFD, the experiment number (N) is calculated by the expression $N = 2^{k-f}$, where k is the number of variables and $f = 1$ indicates the degree of fractionality of 1. The chosen variables were the volume of 65% HNO_3, 30% H_2O_2, 30% HCl and DI water. Maximum and minimum levels of each factor (Table 2) were established according to the data based on the *EPA Method 3052, 1996* guideline. For instance, the addition of 30% H_2O_2 in catalytic amounts (0.1 ml to 2 ml) may aid in the complete oxidation of the organic sample constituents whilst the addition of 2 mL HCl can be appropriate for stabilization of iron in solution and the addition of 0 to 5 ml DI water may improve the solubility of metals and prevent temperature spikes due to exothermic reaction as reported.

Table 3 shows the experimental design matrix, using Cu, Fe and Zn recoveries (taking into account reagent blanks that had undergone particular designed conditions) as analytical responses, All the experiments were carried out in random order and in triplicate, using 0.50 g of DORM-3. The experimental data were processed using CAMO® Unscrambler® V. 9.7 and Microsoft® Excel® 2003. Recovery values were considered as input responses and subjected to analysis of variance (ANOVA). Both the possible experimental errors and non-linearities were estimated from centre samples and replicates, as shown in Table 4. Factor effects were considered significant when the calculated *p*-values are lower than 0.05 (95% confidence interval).

RESULTS AND DISCUSSION

The mean analytical results obtained for DORM-3 in each of the microwave digestion methods studied are shown in Table 3. Recovery ranged between 77% and 119% with relative standard deviation (RSD) lower than 5% ($n = 3$) in almost all cases. It could be noticed that the first experiment using solely HNO_3 was sufficient for satisfactory recoveries

Table 1. FAAS instrumental parameters.

Elements	Wavelength (nm)	Slit width (nm)	Lamp current (mA)	Calibration range (mgL^{-1})	Calibration slope (mgL^{-1})	R^2
Cu	324.7	0.5	3.0	0.10–0.50	0.153	0.999
Fe	248.3	0.2	8.0	1.00–9.00	0.088	0.999
Zn	213.9	0.5	3.0	0.50–1.50	0.688	0.994

Table 2. Factors and levels used in factorial design.

Variable	Symbol	Low Level (–)	Central (0)	High Level (+)
Volume of 60% HNO_3	A	4.00 ml	7.00 ml	10.00 ml
Volume of 30% H_2O_2	B	0.00 ml	1.00 ml	2.00 ml
Volume of 30% HCl	C	0.00 ml	1.00 ml	2.00 ml
Volume of DI H_2O	D	0.00 ml	2.50 ml	5.00 ml

Table 3. Design matrix and the results of the two-level fractional factorial design.

Experiment No. (*n*)	HNO_3 (A)	H_2O_2 (B)	HCl (C)	H_2O (D)	Recovery % Cu	Fe	Zn
1	–	–	–	–	101.7	88.4	94.4
2	+	–	–	+	96.3	76.5	88.2
3	–	+	–	+	89.6	80.9	92.1
4	+	+	–	–	88.2	79.1	86.7
5	–	–	+	+	92.7	90.4	90.2
6	+	–	+	–	98.2	78.0	90.5
7	–	+	+	–	98.1	97.4	103.4
8	+	+	+	+	119.2	87.1	110.3
9	0	0	0	0	107.3	85.8	106.1

All the experiments were run in triplicates.

of Cu and Zn in fish tissue (Pérez *et al*. 2001). However, the percent recovery of Fe could probably be enhanced by adding small amount of other reagents. Therefore, it was essential to study the effect of added reagent on Cu, Fe, and Zn recoveries in order to figure out the optimum condition. For this, Design of Experiment (DoE) was the method of choice.

Since full factorial designs require many more experiments and it is not necessary to perform all combinations to study the main effect, fractional factorial design will definitely be a more economical alternative (Momen *et al*. 2007). This is due to the fact that the number of experiments can be reduced to half compared to the full factorial design method if the degree of fractionality *f* is equal to 1.

However, the price to pay for performing fewer experiments is the problem of confounding, which means that some effects cannot be studied independently of each other. For instance, AB = CD (Table 4) means that the interaction between HNO_3 and H_2O_2 was mixed up with interaction between HCl and H_2O. Nevertheless, the main effects confounded with three-variable interactions (for example, A = BCD) are negligible and can be disregarded since those interactions are unlikely to be significant (Esbensen 2004).

Table 4 shows the results of estimated effect on metal recovery. Based on the results, as the volume of HNO_3 was increased from 4 ml to 10 ml, there was a general rise of 4% in the recovery of Cu but a decrease in Fe recovery (about 9% in average), and no significant main effect on Zn

Table 4. Estimates of effect on metal recovery based on fractional factorial design.

Variable	Cu			Fe			Zn		
Multiple correlation	0.962			0.929			0.965		
R-Square	0.926			0.863			0.931		
Curvature	$p = 4.929\times10^{-3}$			p = 0.373			$p = 5.705\times10^{-3}$		
	Effect	F-ratio	*p*	Effect	F-ratio	*p*	Effect	F-ratio	*p*
HNO_3 (A = BCD)	4.338	106.002	0.0093	–9.132	198.169	0.0050	–1.113	3.591	0.1986
H_2O_2 (B = ACD)	2.180	26.778	0.0354	2.815	18.826	0.0492	7.309	154.729	0.0064
HCl (C = ABD)	7.533	319.608	0.0031	6.993	116.231	0.0085	8.317	200.364	0.0050
H_2O (D = ABC)	3.506	69.236	0.0141	–1.996	9.464	0.0914	1.455	6.130	0.1317
AB = CD	4.259	102.151	0.0096	3.058	22.219	0.0422	1.852	9.930	0.0877
AC = BD	8.942	451.315	0.0022	–2.239	11.917	0.0746	4.685	63.573	0.0154
AD = BC	11.097	693.534	0.0014	5.244	65.360	0.0150	9.211	245.763	0.0040

recovery. Therefore we believe that using 10 ml 70% HNO_3 solely, as indicated by the CEM MarXpress Microwave manufacturer for animal tissue digestion, would be adequate for the determination of Cu and Zn, but not for Fe.

Although the main effect of HNO_3 on Zn recovery was negligible, its interaction effects might be significant (Table 4). Additions of 2 ml of HCl and/or H_2O_2 to HNO_3 resulted in significant recoveries of Fe, Cu and Zn for microwave digestion (*p*-values < 0.05 for both HCl and H_2O_2 main effects). These effects were reported by Bermejo-Barrera *et al.* (2000) as well. It is quite clear that adding 30% H_2O_2 to HNO_3 could aid in complete fish muscle digestion (especially organic based Zn), because H_2O_2 not only increases the oxidation power of HNO_3 during digestion, but at the same time it increases the pressure in the closed vessel which enhances the attack on organic material present in the sample (Krachler *et al*. 2002). However, mixtures of HNO_3 and H_2O_2 alone cannot dissolve all the digested materials that are present in the sample completely (Sapkota *et al*. 2005), thus leading to relatively lower recoveries (as in Table 3: Experiment No. 3 and 4). Addition of HCl aids the stabilization of Fe ions (*EPA Method 3051A, 2007*) due to the solubility of the iron oxide and iron itself in diluted HCl solution. The addition of H_2O showed no significant main effect on both Fe and Zn recoveries, but was likely to be significant on Cu recovery (Effect = 3.506, *p*-value < 0.05).

Based on the results as tabulated in Table 4, there seemed to be a strong non-linear relationship between Cu and Zn recoveries and the factors/interactions under the diagnosis of centre samples (*p*-value for curvature test <0.05). The small *p*-value indicates lack of fit of a linear model which does not describe the true shape of the response surface adequately. In both cases, quadratic relationships needed to be considered if further optimization took place. On the other hand, the Fe recovery model (Table 5) established from four main factors and 3 second order interactions showed significant linear relationship. From the results, it could be seen that both HCl and HNO_3 volumes are the most significant (*p*-value = 0.0000) variables that contribute to Fe recovery. This indicated that appropriate HNO_2:HCl ratio is a key factor for optimum Fe recovery.

Based on the observations in Table 3, the most optimum microwave digestion condition was achieved by Experiment 7 which resulted in the most satisfactory metal recoveries (Table 6).

CONCLUSION

Fractional factorial design with effect analysis demonstrated better recoveries upon addition of H_2O_2 and HCl to HNO_3 prior to microwave digestion. Addition of HCl was appropriate in order to optimize the Fe recovery in fish protein matrix. An optimal combination of 4 ml 65% HNO_3, 2 ml 30% H_2O_2 and 2 ml 30% HCl gave the most satisfactory percentage recovery of the metals.

Table 5. Analysis of variance of Fe linear model.

Fe	SS	DF	MS	F-ratio	*p*-value	B-coefficients	Std. error
Model	1.12×10^3	7	159.484	16.299	0.0000		
Error	185.916	19	9.785				
Adjusted total	1.30×10^3	26	50.089				
Variable							
Intercept	1.85×10^4	1	1.85×10^4	1.89×10^3	0.0000	84.838	1.951
HNO_3(A = BCD)	500.319	1	500.319	51.131	0.0000	–1.522	0.213
H_2O_2(B = ACD)	47.529	1	47.529	4.857	0.0401	1.407	0.639
HCl(C = ABD)	293.449	1	293.449	29.99	0.0000	3.497	0.639
H_2O(D = ABC)	23.894	1	23.894	2.442	0.1346	–0.399	0.255
AB = CD	56.097	1	56.097	5.733	0.0271	1.411	0.589
AC = BD	30.088	1	30.088	3.075	0.0956	–1.034	0.589
AD = BC	165.014	1	165.014	16.864	0.0006	2.42	0.589
Model check							
Main	865.191	4	216.298				
Interaction	251.198	3	83.733	8.557	0.0008		
Lack of fit							
Lack of fit	3.277	1	3.277	0.323	0.5769		
Pure error	182.639	18	10.147				
Total error	185.916	19	9.785				

$R = 0.926$, $R^2 = 0.857$; SS: sum of squares; DF: degrees of freedom; MS: mean squares.

Table 6. Analytical performance of experiment no. 7.

Elements	DORM-3 Certified value (mg/kg)	Found value (mg/kg)	RSD (%)	Recovery (%)
Cu	15.5 ± 0.63	15.2 ± 0.3	1.6	98 ± 2
Fe	347 ± 20	338 ± 11	3.2	98 ± 3
Zn	51.3 ± 3.1	53.2 ± 0.1	0.1	103.6 ± 0.1

All the experiments were run in triplicates, indicated with mean ± standard deviation.

ACKNOWLEDGEMENT

The authors acknowledge the financial support (SF107/2007A, PS147/2007B and 16-02-03-6020) of the University of Malaya and the Ministry of Science, Technology and Innovation, Malaysia.

Date of submission: February 2009
Date of acceptance: September 2009

REFERENCES

Bermejo-Barrera, P *et al*. 2000, 'Optimization of a microwave-pseudo-digestion procedure by experimental designs for the determination of trace elements in seafood products by atomic absorption spectrometry', *Spectrochimica Acta Part B*, vol. 55, pp. 1351–1371.

Celik, U & Oehlenschlager, J 2007, 'High contents of cadmium, lead, zinc and copper in popular fishery products sold in Turkish supermarkets', *Food Control*, vol. 18, pp. 258–261.

Cerutti, S *et al*. 2004, 'Factorial design for multivariate optimization of an on-line preconcentration system for platinum determination by ultrasonic nebulization coupled to inductively coupled plasma optical emission spectrometry', *Talanta*, vol. 63, pp. 1077–1082.

EPA Method 3051A, 2007, *Microwave assist acid digestion of sediments, sludges, soils and oils*, United States Environmental Protection Agency, US.

EPA Method 3052, 1996, *Microwave assist acid digestion of siliceous and organically based matrices*, United States Environmental Protection Agency, US.

Esbensen, KH 2004, '*Multivariate data analysis – in practice*, 5th edn, Camo Process, AS, Norway.

Hamilton, MA *et al.* 2007, 'Determination and comparison of heavy metals in selected seafood, water, vegetation and sediments by inductively coupled plasma-optical emission spectrometry from an industrialized and pristine waterway in Southwest Louisiana', *Microchemical Journal*, vol. 88, no. 1, pp. 52–55.

Hseu, ZY 2004, 'Evaluating heavy metal contents in nine composts using four digestion methods', *Bioresource Technology*, vol. 95, no. 1, pp. 53–59.

Jalbani, M *et al*. 2006, 'Application of factorial design in optimization of ultrasonic-assisted extraction of aluminum in juices and soft drinks', *Talanta*, vol. 70, pp. 307–314.

Krachler, M *et al.* 2002, 'Analytical procedures for the determination of selected trace elements in peat and plant samples by inductively coupled plasma mass spectrometry', *Spectrochimica Acta Part B*, 2002, vol. 57, pp. 1277–1289.

Manutsewee, N *et al.* 2007, 'Determination of Cd, Cu, and Zn in fish and mussel by AAS after ultrasound-assisted acid leaching extraction', *Food Chemistry*, vol. 101, no.2, pp. 817–824.

Mendil, D & Uluözlü, ÖD 2007, 'Determination of trace metal levels in sediment and five fish species from lakes in Tokat, Turkey', *Food Chemistry*, vol. 101, no. 2, pp. 739–745.

Momen, AA *et al.* 2007, 'Use of fractional factorial design for optimization of digestion procedures followed by multi-element determination of essential and non-essential elements in nuts using ICP-OES technique', *Talanta*, vol. 71, pp. 443–451.

Pérez CB *et al.* 2001, 'Determination of trace metals in fish species of the Ria de Aveiro (Portugal) by electrothermal atomic absorption spectrometry', *Food Chemistry*, vol. 75, no. 1, pp. 93–100.

Reis, PA & Almeida CMR 2008, 'Matrix importance in animal material pre-treatment for metal determination', *Food Chemistry*, vol. 107, no. 3 pp. 1294–1299.

Reis, PA *et al.* 2008, 'A fast and simple methodology for determination of yttrium as an inert marker in digestibility studies', *Food Chemistry*, vol. 108, no. 3, pp. 1094–1098.

Retief, N-R *et al.* 2006, 'The use of cestode parasites from the largemouth yellowfish, Labeobarbus kimberleyensis (Gilchrist and Thompson, 1913) in the Vaal Dam, South Africa as indicators of heavy metal bioaccumulation', *Physics and Chemistry of the Earth, Parts A/B/C*, vol. 31, no. 15–16, pp. 840–847.

Sapkota, A *et al.* 2005, 'Analytical procedures for the determination of selected major (Al, Ca, Fe, K, Mg, Na, and Ti) and trace (Li, Mn, Sr, and Zn) elements in peat and plant samples using inductively coupled plasma-optical emission spectrometry', *Analytica Chimica Acta*, vol. 540 no. 2, pp. 247–256.

Scancar, J, Stibilj, V & Milacic, R 2004, 'Determination of aluminium in Slovenian foodstuffs and its leachability from aluminium-cookware', *Food Chemistry*, vol. 85, no. 1, pp. 151–157.

Soylak, M *et al.* 2007, 'Optimization of microwave assisted digestion procedure for the determination of zinc, copper and nickel in tea samples employing flame atomic absorption spectrometry', *Journal of Hazardous Materials*, vol. 149, pp. 264–268.

Sures, B, Taraschewski, H & Haug, C 1995, 'Determination of trace metals (Cd, Pb) in fish by electrothermal atomic absorption spectrometry after microwave digestion', *Analytica Chimica Acta*, vol. 311, no. 2, pp. 135–139.

Türkmen, A *et al.* 2005, 'Heavy metals in three commercially valuable fish species from Iskenderun Bay, Northern East Mediterranean Sea, Turkey', *Food Chemistry*, vol. 91, no. 1, pp. 167–175.

Tüzen, M 2003, 'Determination of heavy metals in fish samples of the middle Black Sea (Turkey) by graphite furnace atomic absorption spectrometry', *Food Chemistry*, vol. 80, no. 1, pp. 119–123.

Uluozlu, OD *et al.* 2007, 'Trace metal content in nine species of fish from the Black and Aegean Seas, Turkey', *Food Chemistry*, vol. 104, no. 2, pp. 835–840.

Vandercasteele, C & Block, CB (eds) 1993, *Modern methods for trace element determination*, John Wiley & Sons, Chichester, UK.

ASM Sci. J., **3(1)**, 77–90

Performance Analysis of a Commodity-class Linux Cluster for Computational Chemistry Applications

N.Y.M. Omar[1], N.A. Rahman[1] and S.M. Zain[1]*

Computational chemistry is a discipline that concerns the computing of physical and chemical properties of atoms and molecules using the fundamentals of quantum mechanics. The expense of computational chemistry calculations is significant and limited by available computational capabilities. The use of high-performance computing clusters alleviate such calculations. However, as high-performance computing (HPC) clusters have always required a balance between four major factors: raw computing power, memory size, I/O capacity, and communication capacity. In this paper, we present the results of standard HPC benchmarks in order to help assess the performance characteristics of the various hardware and software components of a home-built commodity-class Linux cluster. We optimized a range of TCP/MPICH parameters and achieved a maximum MPICH bandwidth of 666 Mbps. The bandwidth and latency of GA put/get operations were better than the corresponding MPICH send/receive ones. We also examined the NFS, PVFS2, and Lustre parallel filesystems and Lustre provided the best read/write bandwidths with more than 90% of those of the local filesystem.

Key words: high-performance parallel computing; gigabit ethernet; parallel I/O; NWChem; GAMESS-UK; Computational chemistry; MPICH; Linux cluster; Lustre parallel filesystems

Computational chemistry problems have insatiable appetite for computer resources and typically take several days or even weeks for a single processor to produce a final result. Cluster computing solutions from commercial vendors are very expensive and are often beyond the capabilities of small to medium-sized research groups. On the other hand, commodity clusters, including Beowulf clusters, are constructed using commodity off-the-shelf computers and hardware, and freely available, open source software. They thus have been used in diverse fields to help provide a cost-effective solution (i.e. a good price/performance ratio) and to handle large problem sizes beyond the capability of a single computer (Sloan 2005).

The high-performance cluster components are generally broken down into multiple categories: the cluster nodes (head node and compute nodes), cluster network, operating system, cluster middleware and cluster parallel applications (Cisco Systems Inc. 2004).

The installation and configuration of cluster's middleware can be simplified by installing cluster management software such as OSCAR and NPACI Rocks. NPACI Rocks is an open source Linux cluster distribution with hundreds of researchers around the world using it to deploy their own computational clusters. It is designed to make clusters easy to deploy, manage, maintain, upgrade and scale. The Rocks package utilizes open source components and is available as a free download.

The North West Chemistry (NWChem) (Kendall *et al.* 2000; Aprà *et al.* 2005) represents a typical parallel cluster application. It is an open source computational chemistry package developed by the Molecular Sciences Software group of the Environmental Molecular Sciences Laboratory (EMSL) at the Pacific Northwest National Laboratory (PNNL). It is designed to run on high-performance parallel computing systems. The package includes (1) high-performance parallel-programming tools and ParSoft libraries such as global arrays (GA), aggregate remote memory copy interface (ARMCI), theoretical chemistry group message-passing (TCGMSG), parallel IO (ParIO), memory allocator (MA), parallel linear algebra (PeIGS), and run time data base (RTDB), (2) chemistry based objects and application programming interfaces (APIs) such as integral API, geometry and basis set objects, symmetry API, property module, and Python) and (3) NWChem modules that spans the range of computational chemistry methods such as Hartree-Fock (HF) or self consistent field (SCF), multiconfiguration SCF (MCSCF), density functional theory (DFT), pseudopotential plane-wave (PSPW), coupled cluster singles and doubles (CCSD), second-order Møller-Plesset (MP2), configuration interaction (CI), molecular mechanics, and molecular dynamics.

GAMESS-UK (GAMESS-UK 2005) is another computational chemistry package that has the capability to run on parallel machines. It uses a number of the high-

[1]Department of Chemistry, University of Malaya, 50603 Kuala Lumpur, Malaysia
* Corresponding author (e-mail: smzain@um.edu.my)

performance parallel-programming tools and libraries as used by the NWChem package. In contrast to NWChem, both SCF and DFT modules are parallelized in a replicated data fashion, with each node maintaining a copy of all data structures present in the serial version.

In order to achieve better computing speed and performance, we have built a commodity-class cluster with 8 Pentium® PCs already available at our department. In addition, this cluster can act as a prototype system and future implementations of Linux clusters at our department can benefit from the benchmarks and suggestions made in this article. We present performance evaluations of the CPU, memory, disk and network. We also consider the effects of some possible configuration and software choices on the computational performance, communications bandwidth and latency, and I/O performance. We emphasize on the tools that are provided by the NWChem and GAMESS-UK computational chemistry packages as well as on the software packages that can improve the performance of these two programs. It is hoped that the outcome of this study will be of assistance to computational chemists willing to design and build a commodity-class cluster.

Cluster Software and Hardware

Our test system for the measurements is a Linux cluster running the NPACI Rocks 4.1 clustering toolkit (using CentOS 4.2 Linux operating system). It consists of one head node (frontend) and seven compute nodes. The frontend node is a Intel® Pentium® IV 2.6 GHz processor with 800 MHz front side bus (FSB), 512 KB level 2 (L2) cache, 3 GB of PC3200 DDR400 SDRAM (dual-channel architecture), and 80 GB 7200 RPM EIDE hard disk. The compute nodes are Intel® Pentium® IV 2.4 GHz processors with 533 MHz FSB, 512 KB L2 cache, 2 GB of PC3200 DDR400 SDRAM (single-channel architecture), and 40 GB 7200 RPM EIDE hard disk. All nodes have integrated Intel Gigabit Ethernet adapters that are connected by 8-port Gigabit Ethernet layer 2 switches using category 6 unshielded twisted pair (UTP) copper cables. The nodes are interconnected using the star topology. The frontend node has one extra fast Ethernet network interface card (NIC) connecting it to the external, public network.

Benchmark Results and Analysis

The performance of a computer is a function of many interrelated quantities. These include the application, the algorithm, the size of the problem, the high-level language, the implementation, the human level of effort used to optimize the program, the compiler's ability to optimize, the age of the compiler, the operating system, the architecture of the computer, and the hardware characteristics (Dongarra *et al*. 2003).

There are three main reasons to run benchmarks. First, if any changes are made to the cluster, a benchmark will provide a baseline to see if performance is really any different. Second, benchmarks are useful when comparing systems or cluster configurations and thus can offer a reasonable basis for selecting between alternatives. Finally, benchmarks can be helpful with planning, such as making better estimates of the impact of scaling the cluster (Sloan 2005).

In this section, we describe the performance of the various components (hardware and software) of our test system based on the results obtained from available benchmarks. All the software packages used are open source and are thus freely available (except the Intel® Compilers for Linux that were obtained under the non-commercial license and the GAMESS-UK package that obtained under the academic parallel license). Compatibility of the various software packages with each other, and with the Linux kernel and hardware were checked prior to installing any package.

Scheme 1 depicts the layered structure of the components of our cluster which will be discussed in the sections to follow.

Compilers, Processor and Memory Performance

We tested the NWChem and GAMESS-UK codes generated by the GNU Compiler Collection (GCC version 3.4.4) and Intel Compilers (version 9.1). The default optimization flags in the makefile were used. Several computational chemistry methods (HF, DFT and MP2) using various basis sets were examined. The Intel compilers generated more optimized code and performance gains of 7%–30% with respect to GCC were obtained.

Since scientific applications such as NWChem and GAMESS-UK are floating-point intensive, we concentrated on the processor's double-precision floating point performance. The High Performance Linpack (HPL) benchmark (Netlib 2006a) measures the floating point execution rate for solving a dense system of linear equations in double precision (64-bit) arithmetic on distributed-memory computers. The HPL benchmark depends on the Basic Linear Algebra Subprograms (BLAS) library for much of the computation. Thus, to get good performance on the HPL benchmark, a high-performance implementation of the BLAS must be available. Optimized BLAS libraries are available for a variety of computer architectures. In the current study, we tested three implementations of the BLAS library, namely, The ATLAS (Automatically Tuned Linear Algebra Software) (version 3.6-0) (ATLAS, 2006), Goto BLAS (version 1.07) (Goto, 2006), and Intel Math Kernel Library (Intel MKL) (version 8.1.014) (Intel MKL, 2006). ATLAS library is installed as part of a standard NPACI Rocks installation. However, both Goto BLAS and Intel MKL libraries need to be manually installed.

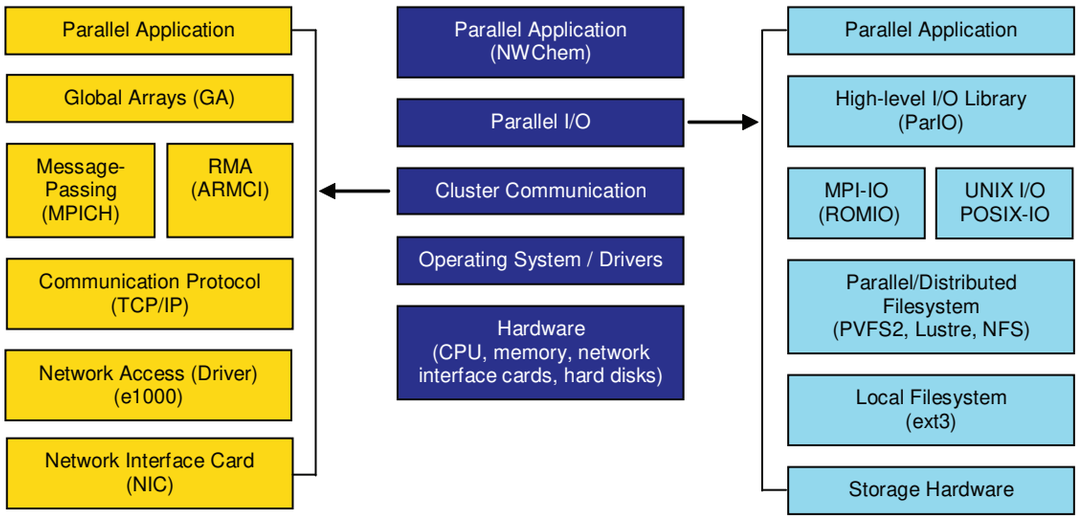

Scheme 1: Layered structure of the test cluster.

We used the HPL benchmark that is distributed with the HPC Challenge Benchmark (version 1.0.0) (HPCC 2006). The executable binary was generated from Intel Compilers (version 9.1). Regarding some of the tunable parameters in the HPL input file (Kandadai 2003; Netlib 2006b), we chose a problem size (N) of 34500 in order to fit 80% of the total amount of memory, that is:

$$N = \sqrt{\frac{No.\ of\ machines \times Memory\ per\ node\ (byte)}{8}} \times 0.80$$

a block size (NB) of 80, and a process grid P × Q of 1 × 7.

Table 1 shows the performance data obtained on our test system using the three optimized BLAS libraries. The data was obtained after the network had been tuned as described in Network performance, below. The performance numbers are also given as percentages of the theoretical peak performance in order to determine system efficiency. The theoretical peak performance of the Pentium® IV processor running at 2.4 GHz is 4.8 Gflop/s. For our testing system (7 compute nodes), this would give a theoretical peak performance of 33.6 Gflop/s. It can be seen from the table that Intel MKL had the best performance followed by Goto BLAS and then by ATLAS.

The NWChem and GAMESS-UK programs rely on the BLAS library for performing linear algebra operations. Both programs have their own BLAS. We ran some tests to see how this could be compared to the three BLAS libraries mentioned above. Table 2 shows the CPU times (in seconds). As can be seen, all BLAS libraries had comparable performance to the program's own BLAS. The most noticeable observation was the improved performance using the Goto BLAS library when runing DFT calculations.

The memory bandwidth might have an influence on the performance of scientific applications, and it depends on the memory subsystem design (Mucci 2004; Ladman 2005). We used the MPI version of STREAM that is part of the HPC Challenge Benchmark (version 1.0.0) (HPCC 2006). The average performance (per node) of the copy, scale, add, and triad operations were 1.76 GB/s, 1.13 GB/s, 1.33 GB/s, and 1.33 GB/s, respectively (theoretical memory bandwidth is 3.2 GB/s). As observed, the copy test was faster than the other tests implying the cost for floating-point arithmetic operation(s).

Network Performance

In any cluster, the network is often the greatest determinant of parallel application speed and cluster efficiency. Parallel high-performance computing applications have wide variation in communication patterns and impose diverse requirements on the network subsystem (Kim & Lilja 1998; Baker 2000).

Communication performance is affected by a number of factors including processor speed, I/O speed, PCI and memory bus architecture, network adaptors, device drivers, and protocol stack processing. The two chief characteristics establishing the operational properties of a network are bandwidth and latency (Baker 2000). The communication performance at the application level depends on the collaboration of all components in the communication system, and inefficiencies can occur at many levels between

Table 1. HPL benchmark results using different BLAS libraries.

BLAS library	No. of processors	Problem size (N)	Block size (NB)	Processor performance (Gflop/s)	Theoretical (Gflop/s)	Performance	%
ATLAS	7	34500	80	1×7	33.6	19.2	57
Goto BLAS	7	34500	80	1×7	33.6	23.7	71
Intel® MKL	7	34500	80	1×7	33.6	24.1	72

Table 2. CPU times in seconds for NWChem and GAMESS-UK calculations using different BLAS libraries.

Program/BLAS	Method		
	HF*	DFT§	MP2$
NWChem			
NWChem-BLAS	1445	118	183
ATLAS	1454	132	182
Goto BLAS	1453	80	179
Intel® MKL	1452	121	179
GAMESS-UK			
GAMESS-UK-BLAS	1194	1943	455
Goto BLAS	1158	1795	455
Intel® MKL	1172	1928	447

* For NWChem: calculation on arecoline using the 6-311G basis set. For GAMESS-UK: calculation on cyclosporin usin the 6-31G basis set.

§ For NWChem: calculation on pyrrole using the 6-311G** basis set. For GAMESS-UK: calculation on cyclosporin using the 6-31G basis set.

$ For NWChem: calculation on propane using the 6-311G** basis set. For GAMESS-UK: calculation on C_2H_4S using the cc-pVTZ basis set.

the application and hardware layers (Turner & Chen 2002; Nguyen & Le 2003; Feng & Hurwitz 2005) (Scheme 1).

Gigabit Ethernet (GigE) with the TCP/IP protocol is a popular interconnection technology when cost is considered as an important design requirement. A number of TCP parameters need to be optimized in order to tune the TCP/IP protocol for GigE (Farrell & Ong 2000, 2003; Feng *et al.* 2003, 2005; Hurwitz & Feng 2003; Majumder & Rixner 2004; Sokolowski & Grosu 2004). For optimizing the performance, we modified several drivers (the Linux base driver for the Intel GigE adapter; e1000) and TCP/MPICH parameters as outlined below. Detailed descriptions about these parameters and their impact can be found in references (Ubik & Cimbal 2003; Ciliendo 2005; Intel® 2005; Jones 2006; Linux TCP Tuning 2006).

1. Allow the driver to buffer more incoming packets and to queue more transmits by increasing the R x Descriptors and T x Descriptors values to 4096.
2. Turning off interrupt coalescence (IC) by setting the InterruptThrottleRate value to zero.

   To make the changes in 1 and 2 permanent, one can edit the /etc/modprobe.conf file and add the following line:
   options e1000 InterruptThrottleRate = 0 R x Descriptors = 4096 T x Descriptors = 4096
3. Turn on TCP segmentation offload (TSO). This can be done by running 'ethtool -K eth0 tso on' command.
4. Enable Jumbo frames by increasing the Maximum Transmission Unit (MTU) to 8160-byte. An 8160-byte MTU allows an entire packet to fit in a single 8192-byte block (Feng *et al.* 2003). To make the change permanent, the following entry is added to the /etc/sysconfig/network-scripts/ifcfg-eth0 file:
   MTU=8160
5. Increase the maximum TCP buffer size (maximum receive/send window size) to 8 MB. To make the

changes permanent, one can edit the /etc/sysctl.conf file and add the following two lines:

net.core.rmem_max = 8388608

net.core.wmem_max = 8388608

6. Increase the socket buffer sizes (memory reserved for TCP receive/send) to 8 MB. To make the changes permanent, one can edit the /etc/sysctl.conf file and add the following two lines:

   net.ipv4.tcp_rmem = 4096 87380 8388608

   net.ipv4.tcp_wmem = 4096 16384 8388608

7. Increase the amount of allowed unprocessed packets to 1000 to avoid loosing (dropping) packets at the receiver side. This can be done by adding the following line to the /etc/sysctl.conf file:

   net.core.netdev_max_backlog = 1000

8. Clear TCP cache between connections by adding the following line to the /etc/sysctl.conf file:

   net.ipv4.tcp_no_metrics_save = 1

9. Increase the P4_SOCKBUFSIZE to 512 KB. This value must be less than the maximum TCP buffer size. To set it, the following entry can be added to the ~/.bashrc file:

   export P4_SOCKBUFSIZE = 512000

10. Stop the IPTables (Firewall) by running '/etc/init.d/iptables stop' command.

We now outline the performance results obtained on our test system. The benchmark used to test the communication performance was NetPIPE (version 3.6.2) (NetPIPE 2006). Different socket buffer sizes (128 KB to 16 MB) against different sizes of MTU (1500, 3000, 4500, 6000, 7500, 9000 and 8160) were tested. The best value for socket buffer size was found to be 8 MB. Figure 1 shows the obtained throughput (bandwidth) for MTU sizes of 1500, 8160 and 9000 at this socket buffer size. The non-standard 8160-byte MTU yielded the best peak throughput (816 Mbps) compared to 754 Mbps for 9000-byte MTU and 626 Mbps for the conventional 1500-byte MTU. The enhanced throughput in the case of Jumbo frames was apparent for messages larger than 128 KB. For messages in the range of 2 KB to 128 KB, the conventional 1500-byte MTU showed better performance, while for messages smaller than 2 KB all MTU sizes exhibited the same performance. Turning on interrupt coalescence (IC) increased the peak throughput for the 1500-byte MTU from 626 Mbps to 796 Mbps but no influence of IC on the 8160-byte MTU was observed. However, turning on interrupt coalescence would increase the latency for shorter messages.

Figures 2 to 4 illustrate the latency for different message size ranges. It can be seen that (1) for messages less than 2 KB, all MTU sizes showed comparable latencies, (2) for messages in the range of 2 KB – 128 KB, the 1500-byte MTU had lower latency, and (3) for messages greater than 128 KB, the 8160-byte gave lower latencies. To see the effect of IC on latency, Figures 2 to 4 show the case for 8160-byte MTU with and without IC. Disabling interrupt coalescence significantly reduced the latency from 62.5 µs (the latency for 8-byte message) to 46.5 µs. For messages larger than 12 KB, the effect was not apparent and both cases showed comparable latencies.

To estimate the CPU load, the output of 'cat /proc/loadavg' command was read before and after each run. At the server side, the load averages for 1500-byte and 8160-byte MTU were 0.27 and 0.16, respectively. At the client side, they were 0.11 and 0.05, respectively. This gave us the conclusion that the use of Jumbo frames reduced the load on the system probably through less CPU utilization.

From the above discussion, it can be deduced that if the application communicates with message sizes in the range of 2 KB to 128 KB, the 1500-byte MTU was a better choice since it had better throughput performance and lower latency at that range of message sizes. In general, the 8160-byte MTU gave the best throughput for larger message sizes, and turning off interrupt coalescence reduced the latency of smaller ones. Thus, the 8160-byte MTU in conjunction with disabling interrupt coalescence was used throughout this study.

The message-passing interface (MPI) over GigE uses TCP as its transport; similarly, MPI-based applications use MPI as their transport (Gupta *et al.* 2005; Sloan 2005). Our system used MPICH1 (version 1.2.7p1), configured with the ch_p4 device, as the MPI implementation (MPICH 2006). MPICH 1.2.7p1 is installed as part of a standard NPACI Rocks installation. MPICH 1.2.7p1 has some limits that do not fully utilize today's computing power, and thus source modifications, reconfiguration, and recompiling the source code are needed. We followed the modifications recommended by He (2006). These include (1) changing the upper limit for P4_GLOBMEMSIZE from 256 MB to 1.5 GB, (2) changing the upper limit for P4_SOCKBUFSIZE from 16 KB to 1 MB, and (3) changing the maximum size of single message from 256 MB to 1 GB. Linux kernel 2.6 has a default maximum segment size (SHMMAX) of 32 MB, a default maximum number of segments of 4096, and a default maximum shared memory of 8 GB. Shared memory segments are not only resources for the MPICH implementation, but also resources for the system. In NPACI Rocks, the maximum segment size for a compute node is

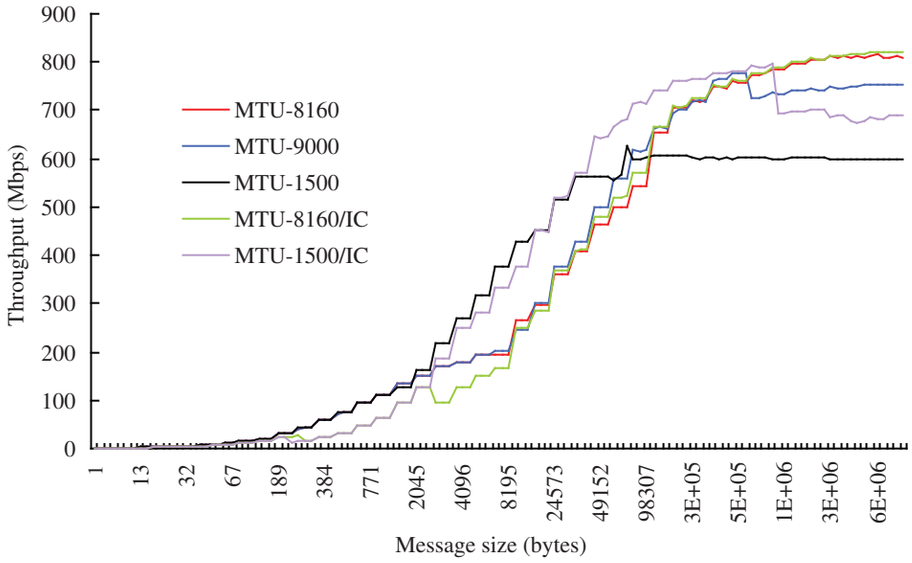

Figure 1. Bandwidths for MTU 1500, 8160, and 9000 with and without interrupt coalescence (IC) at 8 MB socket buffer size.

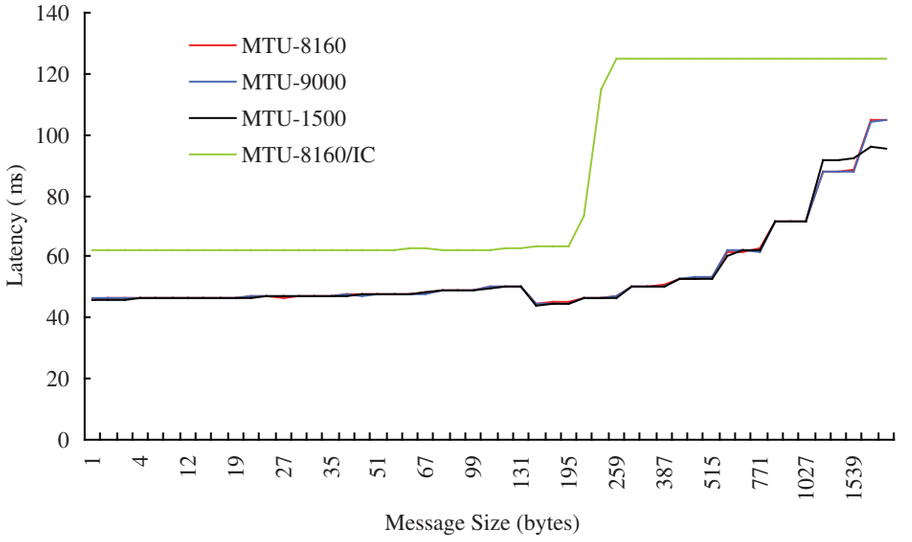

Figure 2. Latencies for MTU 1500, 8160, and 9000 for message sizes less than 2 KB.

set by default to ¾ the available physical memory (1.5 GB on our test system). The values of the two environment variables P4_GLOBMEMSIZE and P4_SOCKBUFSIZE can be set during run-time by adding entries to the ~/.bashrc file but not exceeding the upper limits mentioned above. We used the GNU GCC compilers (version 3.4.4) and Intel compilers (version 9.1) to compile the MPICH library. There was no clear performance difference between the two compilers.

The primary optimization parameter that is important to maximizing the performance of MPICH is the P4_SOCKBUFSIZE environment variable. Varying this variable from 64 KB to 1 MB, the best result was obtained at 512 KB with peak throughput performance of 666 Mbps (Figure 5). Figure 5 shows that MPICH suffers a 5%–20% loss as compared to raw TCP performance. The latency increased from 46.5 µs for raw TCP to 52 µs for MPICH. Turning off IPTables reduced the latency for MPICH from 52 µs to 49 µs.

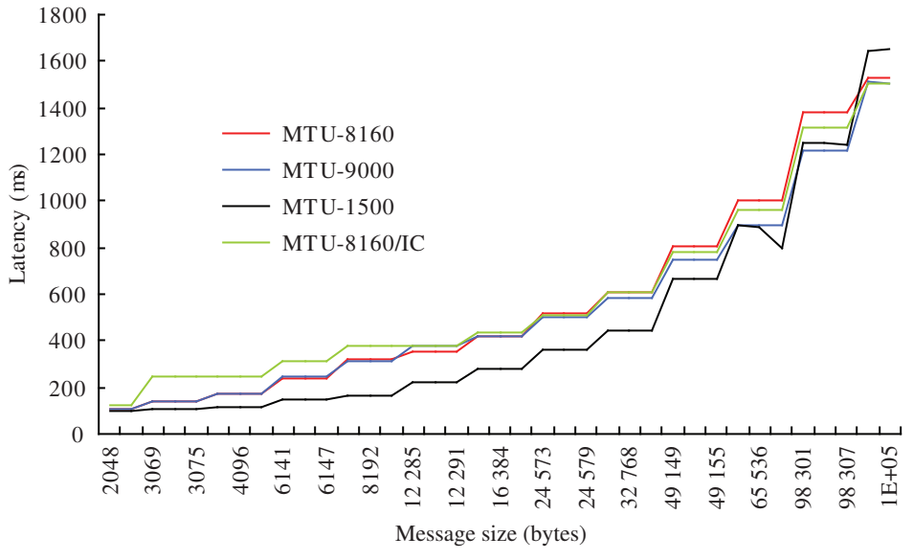

Figure 3. Latencies for MTU 1500, 8160, and 9000 for message sizes in the range of 2 KB to 128 KB.

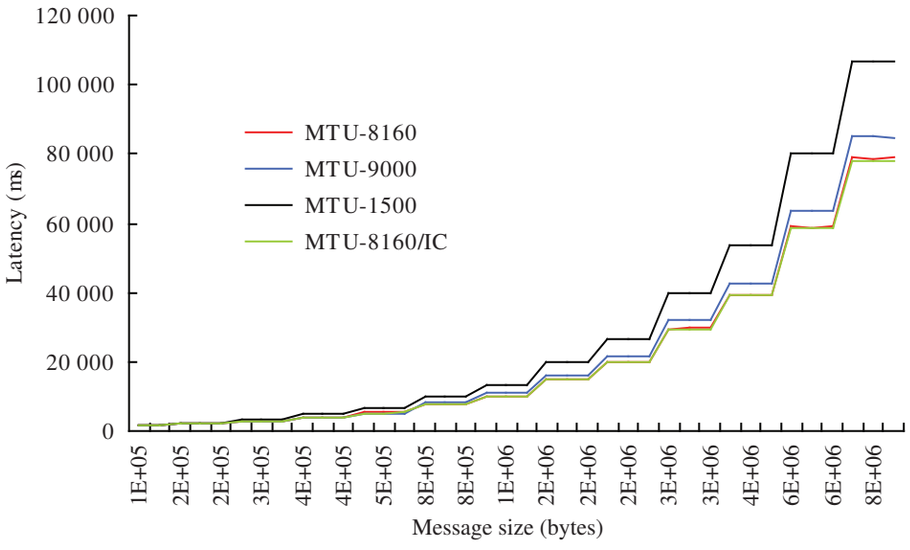

Figure 4. Latencies for MTU 1500, 8160, and 9000 for message sizes greater than 128 KB.

The Theoretical Chemistry Group Message-Passing (TCGMSG) provides an interface between applications (e.g. NWChem and GAMESS-UK) and either TCP or an underlying message-passing library like MPI. TCGMSG-MPI is a TCGMSG interface implementation on top of MPI, and the library is distributed with the Global Arrays package (Global Arrays 2006). In the current study, the overhead introduced by using the TCGMSG layer on top of MPICH was very minor. The TCGMSG-MPICH curve (Figure 5) falls to within 1% of the MPICH curve and the latency was increased by less than 1 µs. This is not surprising since TCGMSG was only a thin layer on top of MPICH.

For some parallel applications, the use of Remote Memory Access (RMA) operations (i.e. one-sided communication operations) offers several advantages over message passing in terms of simplicity of use, applicability,

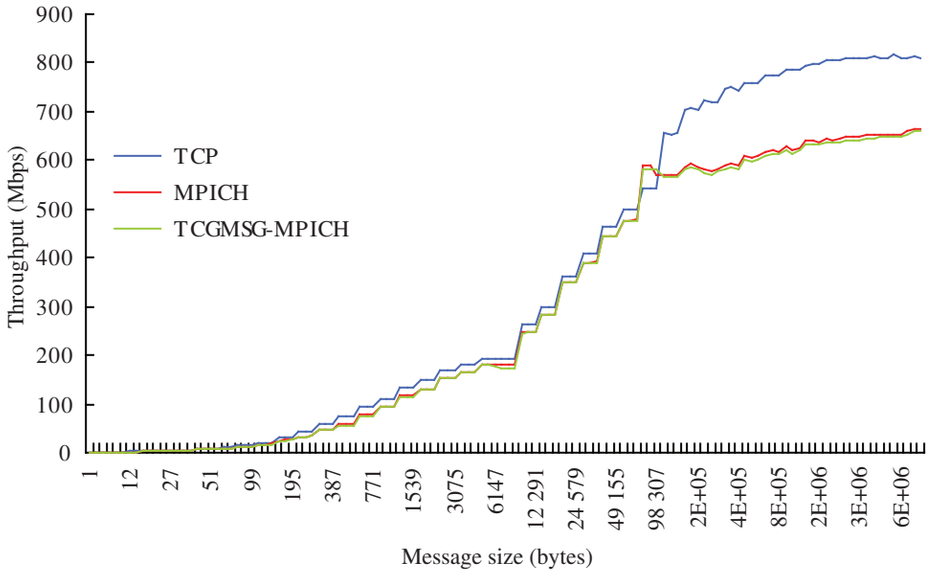

Figure 5. Bandwidths for raw TCP, MPICH, and TCGMSG-MPICH.

and performance. Both programs NWChem and GAMESS-UK make use of the Global Arrays (GA) library (Nieplocha *et al.* 1994, 1996, 2002a; Steinke 2000; Guiang *et al.* 2002). All RMA operations in GA are facilitated by the Aggregate Remote Memory Copy Interface (ARMCI) library (Nieplocha & Carpenter 1999; Nieplocha *et al*. 2000, 2001, 2002b; Tipparaju *et al.* 2004; Krishnan & Nieplocha 2005) included in the GA package.

Figure 6 shows the performance of MPICH, ARMCI and GA. For ARMCI, the curve represents the average of remote put and get operations to transfer both contiguous and non-contiguous (strided) data. For GA, the curve represents the average of remote put and get operations to transfer both 1-D and 2-D array sections. The MPICH results were obtained using the multi-PingPong benchmark available from the Intel MPI Benchmarks (IMB) suite (version 2.3) (Intel IMB, 2006). The GA (version 4.0.1) and ARMCI (version 1.1) were used in the tests. The benchmarks used to generate the results are available within the GA package.

In the case of both contiguous and non-contiguous (strided) data transfers, the ARMCI put and get operations outperformed the corresponding MPI send/receive operations (Figure 6). GA's communication interfaces form a thin wrapper around ARMCI interfaces. As can be seen in Figure 6, the GA curve falls to within 1%–20% of the ARMCI curve. Table 3 shows the latency numbers for the MPI send/receive, the ARMCI remote put/get, and the GA remote put/get operations. The wide gap between the put and get operations may be attributed to the fact that the put operation only signals that the data has been copied out of the calling process' local memory and may occur before data is actually transferred to the remote process, while the get operation is not complete until the remote data has been written to the calling process' local memory.

Disk Storage and Parallel I/O Performance

In out-of-core parallel computations, disk storage is treated as another level in the memory hierarchy, below CPU registers, caches (level 1, level 2, and level 3), local memory, and remote memories. Each level of this hierarchy owns a larger memory capacity and is slower than the higher levels.

Computational chemistry algorithms may be generally classified as a combination of in-core, conventional or direct method, and sequential or parallel operation (Nieplocha *et al.* 1998; Hawick *et al.* 2000). The size of storage space required depends on the computational chemistry method being used, the basis set(s) used, the use of symmetry or not, and the number of atoms in the simulation.

Most scientific applications need to perform I/O for a number of reasons such as reading initial data, writing the results, checkpointing, out-of-core data sets, and scratch files for temporary storage. Types of parallel I/O operations in computational chemistry applications include collective and non-collective I/O operations (Nieplocha *et al.* 1998).

The two main requirements for I/O-intensive applications are I/O speed and storage capacity. I/O performance

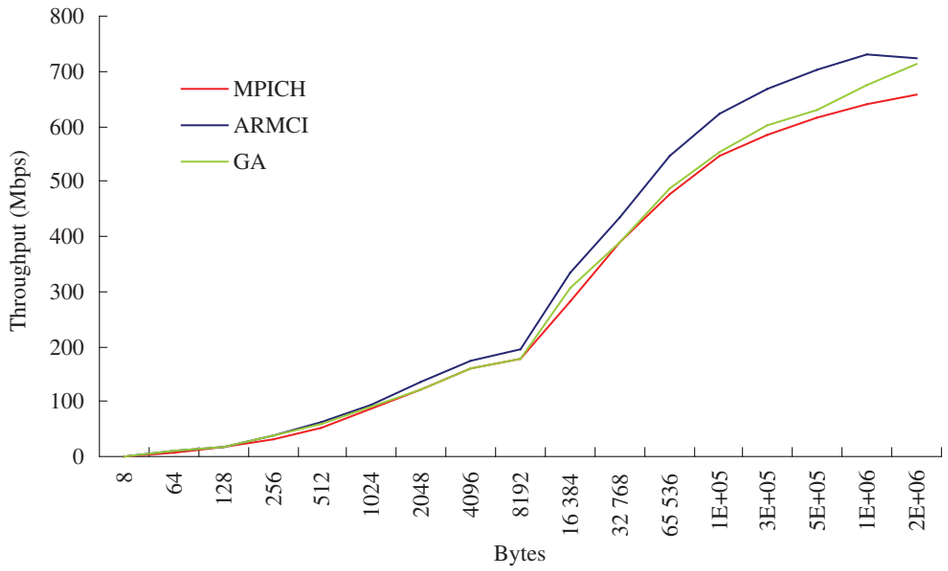

Figure 6. Bandwidths for MPICH, ARMCI, and GA libraries.

Table 3. Latency numbers for MPICH, ARMCI, and GA operations.

Interface	Latency (μs)	
MPI	56.6	
	put	get
ARMCI	1.4	50.1
GA	2.1	55.3

has lagged behind the computation and communication performance of high-performance computing clusters. The use of parallel filesystems can help solve this problem by typically striping files across multiple I/O nodes thus aggregating the moderate I/O capabilities of each node to make up a very fast disk (Thakur *et al.* 1998).

Applications can access files located in (parallel) filesystems by using an interface such as UNIX/POSIX I/O (Vilayannur *et al.* 2004; Ching *et al*. 2007), MPI-IO (e.g., ROMIO (Thakur *et al*. 1999)), or high-level libraries (e.g., ParIO (Nieplocha *et al.* 1998)). Both programs, NWChem and GAMESS-UK, utilize the ParIO library.

There are three issues to consider for hard disks: interface type (EIDE, SATA, SCSI), disk latency which is a function of rotational speed, and disk capacity. We ran IOZone (IOZone 2006) in order to determine the baseline for our storage hardware with its local filesystem 'third extended filesystem' (ext3). The hardware performance analysis was done by writing a 4 GB file, that was twice the amount of the available RAM in order to avoid any caching effects. Disk read and write speeds were 55 MB/s and 49 MB/s, respectively.

The performance of a parallel filesystem depends on the interconnecting physical network, the type of storage, the amount of storage, the interconnecting storage, the operating system, the parallel filesystem itself, and the application utilizing the filesystem (Leggett *et al.* 2006). The performance of three different parallel filesystems (NFS, PVFS2, and Lustre) was examined using the 'common_file' benchmark that is part of the PRIOmark benchmarks collection (version 0.9.1) (Krietemeyer *et al.* 2005a,b; IPACS, 2006). All performance tests were run after the network had been optimized (Network Performance).

NFS (Network File System) is automatically installed with a standard NPACI Rocks installation where the frontend node is designated as the NFS server. The frontend node exports a directory from a partition to all compute nodes. The partition's local filesystem type is ext3. By default, the NFS is mounted with the async option.

PVFS2 (Parallel Virtual File System 2) is an open source, stable, and scalable parallel filesystem that can be run on Linux clusters and on various computer architectures (e.g., x86, IA-64) (PVFS, 2006). PVFS2 is not included with the NPACI Rocks version that we ran on our system. We installed PVFS2 version 1.5.1 which was a relatively easy process. One major problem was the incompatibility of this PVFS2 version with the 'Berkeley DB' database version 4.2.52 that comes with NPACI Rocks 4.1. This was solved by building PVFS2 against a newly built Berkeley DB (version 4.3.29) (BDB 2006). We partitioned our test cluster so that the first compute node acted as the metadata server while the remaining compute nodes acted as I/O nodes. PVFS2 aggregated the storage space created on the servers into one globally accessible namespace that the clients mounted. The underlying local filesystem was ext3.

Performance tuning of PVFS2 (Leggett *et al.* 2006) is done by (1) mounting the ext3 filesystem with the noatime and data=writeback options in the '/etc/fstab' file, (2) providing the --enable–epoll option to the configure script at compile time in order to provide better performance for TCP/IP sockets, (3) providing the --enable-fast option to the configure script at compile time in order to disable many of the debugging routines, and (4) setting TroveSyncData option to no in the '/etc/pvfs2-fs.conf' file in order to disable the server from issuing a sync call after each data update (The sync call forces all unwritten data to be written to disk). This is analogous to mounting the NFS with the async option. We note here that setting this option to no can lead to data loss if an I/O server is terminated unexpectedly.

Lustre is an open source, scalable, secure, robust, and highly-available parallel filesystem for Linux clusters (Lustre 2006). We tested Lustre version 1.5.95. This version of Lustre does not require the Linux kernel of the client node to be patched. However, Lustre kernel patches need to be applied to the source of the kernel running in the server node. This can be facilitated by using the Quilt package (a patch management tool) provided by Cluster File Systems (CFS). CFS also provides pre-patched, Lustre-enabled Linux kernels as well as Lustre RPMs. These RPMs are only available for SMP machines. Hence, for our test system that comprised only uniprocessor nodes, we had to build the Linux kernel after applying the Lustre kernel patches using Quilt, and then build Lustre from the available source code. We partitioned our test cluster so that the first compute node acted as the MDT (Metadata Target)/MGS (Management Configuration Server) while the remaining compute nodes acted as OSTs (Object Storage Targets). A single partition in each compute node was allocated for use by Lustre filesystem.

Lustre offers several tuning variables to adjust behaviour according to network conditions and cluster size (Lustre Manual 2006; Lustre Wiki 2006a). We chose to change the /proc/fs/lustre/osc/<object name>/max_dirty_mb value from the default of 32 to 128, and the /proc/fs/lustre/osc/<object name>/max_rpcs_in_flight value from the default of 8 to 32. These can be changed while the server is running using the "lctl" utility. In addition, running the command "echo 0 > /proc/sys/portals/debug" for all clients and servers turns off the Lustre debugging completely and enhances the performance (Lustre Wiki 2006b). Furthermore, the number of OSTs to stripe a single file across can be set to a single OST, all OSTs, or any number in between. The choice depends on the application that utilizes the Lustre filesystem (Lustre Manual 2006). The changes can be done using the "lfs" tool.

Our system used the MPICH version 1.2.7p1 with ROMIO version 2005-06-09. It was compiled with support for NFS, PVFS2, and general support for all UNIX like filesystems (UFS). ROMIO's 'UFS' works fine with Lustre. We ran the 'common_file' benchmark for 7 processes. Each MPI process had its own data block in a common file. The file size was set to 4 GB and the size of the IO-request was set to 64 KB. The IO-request size of 64 KB was chosen as to resemble that for the NWChem code (Kandaswamy *et al.* 1997; Smirni & Reed 1997). Both POSIX I/O and MPI-IO interfaces were tested. Access patterns tested were 'write', 'read/write', and 'random read/write'. All measurements used the collective and noncollective blocking (synchronous) MPI-IO access methods 'individual file pointer' (i.e., allowing every process to work on its own part of the file thus having its own file pointer) and 'explicit offset' (i.e. a process specifies the position of any operation within the file).

As shown in Figure 7, Lustre (with striping across all OSTs) outperformed NFS and PVFS2 using the POSIX I/O interface. For the MPI-IO interface, Lustre provided the best bandwidth for noncollective operations, whereas PVFS2 slightly outperformed Lustre for collective operations.

We tested both direct and semi-direct algorithms for the HF and MP2 methods as implemented by the NWChem code using the three parallel filesystems (NFS, PVFS2, and Lustre) as well as the local filesystem. From Table 4 we observe that (1) Lustre with striping the file across all available OSTs outperforms Lustre without striping, (2) the effect of striping size for Lustre is very minimal, (3) Lustre outperforms NFS and PVFS2 at all file size ranges, (4) the best performance for these methods is achieved when writing/reading the integral file to local filesystem (a parallel filesystem is still needed for shared files such as checkpointing files), (5) Lustre achieves a great percentage of the local filesystem (> 90%) and its performance is consistent at all file size ranges, (6) PVFS2 performance is poor compared to NFS. However, one can see that PVFS2 is matching up with NFS as the file size gets larger and closer to the size of the available memory on the node (Linux

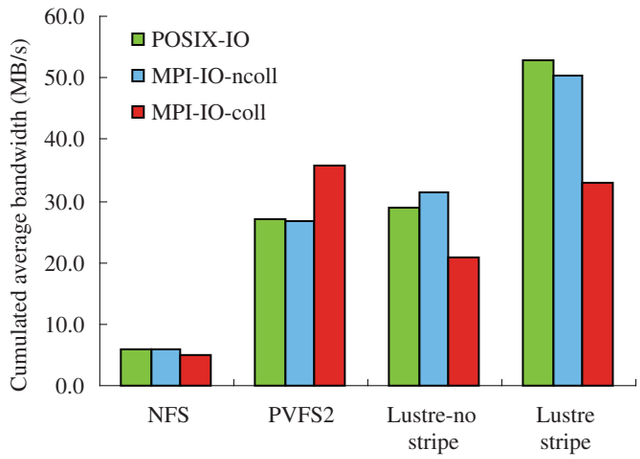

Figure 7. Bandwidths for NFS, PVFS2, and Lustre using the POSIX IO and MPI-IO interfaces. Shown is the average of access patterns 'write', 'read/write', and 'random read/write'. In the case of MPI-IO, this include access methods 'individual file pointer' and 'explicit offset'.

Table 4. Wall times (in seconds) for NWChem direct and semi-direct algorithms using different filesystems.

Method	Filesystem				
	NFS	PVFS2	Lustre-no stripe	Lustre-stripe	Local[$]
dMP2-propane-6-311G**	520	1865	701	460	415
MP2-propane-6-311G** (8 MB)	427 [83]	–	–	386 [92]	356
dHF-morphine-6-31G** (2.2 GB)	–	–	–	807	799
HF-morphine-6-31G** (2.2 GB)	–	–	1666	1200 [93]	1120
dHF-morphine-6-31G* (1.6 GB)	–	–	–	653	–
HF-morphine-6-31G* (1.6 GB)	4509 [19]	4639 [19]	–	936 [93]	872
dHF-atropine-6-31G* (1.2 GB)	–	–	–	853	–
HF-atropine-6-31G* (1.2 GB)	5364 [21]	6655 [17]	–	1216 [91]	1108
dHF-arecoline-6-311G** (600 MB)	–	–	–	571	–
HF-arecoline-6-311G** (600 MB)	2570 [26]	4042 [17]	902	716§ [94]	673
dHF-arecoline-6-311G* (275 MB)	–	–	–	400	–
HF-arecoline-6-311G* (275 MB)	–	–	–	469	–
dHF-arecoline-6-311G (100 MB)	–	–	–	258	–
-arecoline-6-311G (100 MB)‡	395 [60]	–	–	243 [97]	235

[$] Files that need to be shared (e.g., the run-time database file that is similar to the GAMESS-UK dumpfile and is needed for checkpointing) were read from/written to Lustre filesystem.
‡ Integral file size per compute node.
§ Three stripe sizes were compared: 0.5, 1, and 2 MB. No difference was observed.
[ ] Percentage of raw local filesystem.
Note: the 'd' before the method name denotes 'direct'

allocates all free memory for disk cache). The reason for this is that PVFS2 does not cache file data on the client node and is not affected by any buffering/caching effects since data is always transferred over the network (Vilayannur *et al.* 2004). We note here that NFS is not recommended for writing such large files because of the increased overhead on the frontend node which may affect some running programs (e.g. the Ganglia monitoring tool), and (7) for our test cluster, the direct algorithm (i.e. recomputing the integrals for each iteration) outperforms the semi-direct algorithm for runs that involve writing/reading an integral file larger than 100 MB per each compute node.

CONCLUSION

A critical issue in the design of a computer cluster is understanding the applications that it will be supporting. The application's requirements for computing power, memory, I/O and communication must be balanced. Benchmarks, though not real applications, capture essential measurable characteristics that reflect real applications.

In the current work, a commodity class Linux cluster was built and tested to act as a prototype for future implementations of Linux clusters at our department for chemistry applications. The performance analysis of the CPU, memory, disk and network was achieved using open source benchmarks. Various TCP/MPICH parameters were optimized and a maximum bandwidth of 666 Mbps for MPICH was achieved. The GA put/get operations outperformed the corresponding MPICH send/receive operations in terms of both bandwidth and latency. Three different parallel filesystems (NFS, PVFS2, and Lustre) were examined. In most cases, Lustre provided the best performance achieving greater than 90% of the local filesystem read/write bandwidths.

ACKNOWLEDGEMENTS

This project is supported by the Malaysian Academy of Science through SAGA Grant No. 66-02-03-0037. NWChem Version 4.7, as developed and distributed by Pacific Northwest National Laboratory, P. O. Box 999, Richland, Washington 99352 USA, and funded by the U. S. Department of Energy, was used to obtain some of the results presented in this paper.

Date of submission: December 2008
Date of acceptance: September 2009

REFERENCES

Aprà, E *et al*. 2005, *Computational chemistry package for parallel computers, version 4.7*, Pacific Northwest National Laboratory, Richland, Washington 99352-0999, USA.

High performance computational chemistry: an overview of NWchem a distributed parallel application, Kendall, RA *et al*. 2000, AT Computer Phys. Comm., vol. 128, pp. 260–283.

ATLAS, <http://math-atlas.sourceforge.net>.

Baker, M (Ed) 2000, *Cluster computing white paper*. http://arxiv.org/ftp/cs/papers/0004/0004014.pdf>.

BDB, <http://sleepycat2.inetu.net/products/bdb.html>.

Ching, A *et al.* 2007, 'High-performance techniques for parallel I/O', in *Handbook of parallel computing: models, algorithms, and applications*, CRC Press, 2007. <http://www.ece.northwestern.edu/~aching/paper_download/2007handbook.pdf>.

Ciliendo, E 2005, 'Tuning Red Hat Enterprise Linux on IBM xSeries servers', IBM Redpaper, IBM Corp., <http://www.redbooks.ibm.com/redpapers/pdfs/redp3861.pdf>.

Cisco Systems Inc. 2004, 'Cluster computing', <http://www.cisco.com/application/pdf/en/us/guest/netsol/ns500/c654/cdccont_0900aecd80281846.pdf>.

Dongarra, JJ *et al.* 2003, 'The LINPACK benchmark: past, present and future', *Concurrency and Computation: Practice and Experience,* vol. 15, pp. 803–820.

Farrell, PA & Ong, H 2000, 'Communication performance over a gigabit Ethernet network', in *Proceedings of the 19th IEEE International Performance, Computing, and Communications Conference 2000 (IPCCC '00)*, pp. 181–189, <http://ieeexplore.ieee.org/iel5/6712/17967/00830317.pdf>.

Farrell, PA & Ong, H 2003, 'Factors involved in the performance of computations on Beowulf clusters', *Electronic Transactions on Numerical Analysis*, vol. 15, pp. 211–224.

Feng, W *et al.* 2005, 'Performance characterization of a 10-Gigabit Ethernet TOE', in *Proceedings of the 13th Symposium on High Performance Interconnects 2005 (HOTI'05)*, pp. 58–63, IEEE Computer Society Press, <http://ieeexplore.ieee.org/iel5/10367/32970/01544578.pdf?isnumber=&arnumber=1544578>.

Feng, W-c & Hurwitz, JG 2005, 'Analyzing MPI performance over 10-Gigabit Ethernet', *Journal of Parallel and Distributed Computing*, vol. 65, pp. 1253–1260.

Feng, W-C *et al.* 2003, 'Optimizing 10-Gigabit Ethernet for networks of workstations, clusters, and grids: a case study', in *Proceedings of the ACM/IEEE SC2003 Conference, 2003 (SC'03)*, <http://ieeexplore.ieee.org/iel5/10619/33528/01592953.pdf?isnumber=&arnumber=1592953>.

GAMESS-UK is a package of ab initio programs. See: <http://www.cfs.dl.ac.uk/gamess-uk/index.shtml> Guest, MF *et al.* 2005, 'The GAMESS-UK electronic structure package: algorithms, developments and applications', *Molecular Physics*, vol. 103, no. 6–8, pp. 719–747.

Global Arrays, <http://www.emsl.pnl.gov/docs/global>.

Goto, <http://www.tacc.utexas.edu/~kgoto>.

Guiang, CS, Purkayastha, A & Milfeld, KF 2002, 'Remote memory operations on Linux clusters: expressiveness and efficiency

of current implementations', <http://www.tacc.utexas.edu/publications/remotememoryoperations.pdf>.

Gupta, R *et al.* 2005, *Considering middleware options in high-performance computing clusters*, Dell Power Solutions, Dell Inc., 2005, <http://www.dell.com/downloads/global/power/ps1q05-20040177-Gupta-OE.pdf>.

Hawick, KA *et al.* 2000, *Commodity cluster computing for computational chemistry*, DHPC Technical Report 2000 (DHPC-073). <http://www.dhpc.adelaide.edu.au/reports/073/html/>.

He, X 2006, *Installing and using MPICH, MPICH-GM, and MPICH-MX on Linux systems*, IBM Redbooks Paper, IBM Corp., 2006, <http://www.redbooks.ibm.com/redpapers/pdfs/redp4183.pdf>.

HPCC, <http://icl.cs.utk.edu/hpcc>.

Hurwitz, J & Feng, W-C 2003, 'Initial end-to-end performance evaluation of 10-gigabit Ethernet', in *Proceedings of the 11th Symposium on High Performance Interconnects 2003 (HOTI'03)*, pp. 116–121, IEEE Computer Society Press. <http://ieeexplore.ieee.org/iel5/8712/27585/01231487.pdf?isnumber=&arnumber=1231487>.

Intel 2005, *Linux Base driver for the Intel® PRO/1000 family of adapters*, 2005. <http://downloadmirror.intel.com/df-support/4833/ENG/e1000.txt>.

Intel IMB, <http://www.intel.com/cd/software/products/asmo-na/eng/219848.htm>.

Intel MKL, <http://www.intel.com/cd/software/products/asmo-na/eng/307757.htm>.

IOZone, <http://www.iozone.org/>.

IPACS, <http://www.ipacs-benchmark.org/index.php?s=download&unterseite=bench>.

Jones, MT 2006, *Boost socket performance on Linux*, <http://www-128.ibm.com/developerworks/linux/library/l-hisock.html>.

Kandadai, SN 2003, *Tuning tips for HPL on IBM xSeries Linux clusters,* IBM Redbooks Paper, IBM Corp. <http://www.redbooks.ibm.com/redpapers/pdfs/redp3722.pdf>.

Kandaswamy, MA *et al.* 1997, 'Optimization and evaluation of Hartree-Fock application's I/O with PASSION', in *Proceedings of the ACM/IEEE SC97 Conference 1997 (SC'97)*, IEEE Computer Society Press, <http://ieeexplore.ieee.org/iel5/10614/33523/01592612.pdf?arnumber=1592612>.

Kendall, RA *et al.* 2000, 'High performance computational chemistry: An overview of NWChem a distributed parallel application', *Computer Physics Communications*, vol. 128, pp. 260–283.

Kim, JS & Lilja, DJ 1998, 'Characterization of communication patterns in message-passing parallel scientific application programs', in *Proceedings of the Workshop on Communication, Architecture, and Applications for Network-based Parallel Computing*, *International Symposium on High Performance Computer Architecture 1998*, pp. 202–216. <http://www.arctic.umn.edu/papers/comm-char.pdf>.

Krietemeyer, M *et al.* 2005a, 'The PRIOmark parallel I/O benchmark*, International Conference on Parallel and Distributed Computing and Networks 2005*, <http://www.ipacs-benchmark.org/download/marketing/IPACS_PRIOmark_0205.pdf>.

Krietemeyer, M *et al.* 2005b, 'Environment for I/O performance measurement of distributed and local secondary storage', in *Proceedings of the 2005 International Conference on Parallel Processing Workshops (ICPPW'05)*, pp. 501–508, IEEE Computer Society Press. <http://ieeexplore.ieee.org/iel5/9965/32020/01488735.pdf>.

Krishnan, M & Nieplocha, J 2005, 'Optimizing performance on Linux clusters using advanced communication protocols: how 10+ Teraflops was achieved on a 8.6 Teraflops Linpack-rated Linux cluster', in *Proceedings of the 6th International Conference on Linux Clusters, The HPC Revolution 2005*, <http://www.linuxclustersinstitute.org/Linux-HPC-Revolution/Archive/PDF05/24-Krishnan_M.pdf>.

Landman, J 2005, 'Performance comparison of AMD multi-core systems and single-core systems on chemistry and informatics applications, scalable Informatics', <http://eugen.leitl.org/Dual_Core_Performance.pdf>.

Leggett, T, Latham, R & Ross, R 2006, *TeraGrid PVFS2 best practices*, TG-11 Informational Data Working Group 2006. <http://www.teragridforum.org/mediawiki/index.php?title=TG-11>.

Linux TCP Tuning 2006, Linux TCP tuning, <http://www-didc.lbl.gov/TCP-tuning/linux.html>.

Linux TCP Tuning 2006, 'How to achieve gigabit speeds with Linux', <http://datatag.web.cern.ch/datatag/howto/tcp.html>.

Linux TCP Tuning 2006, 'Enabling high performance data transfers', <http://ncne.nlanr.net/networking/projects/tcptune>.

Lustre Manual, <https://mail.clusterfs.com/wikis/attachments/LustreManual.html>.

Lustre Wiki (a) <https://mail.clusterfs.com/wikis/lustre/MountConf>.

Lustre Wiki (b) <https://mail.clusterfs.com/wikis/lustre/LustreDebugging>.

Lustre, <http://www.lustre.org>.

Majumder, S & Rixner, S 2004, 'Comparing Ethernet and Myrinet for MPI Communication', in *Proceedings of the Workshop on Languages, Compilers, and Run-time Support for Scalable Systems 2004 (LCR)*, <http://www.cs.rice.edu/CS/Architecture/docs/majumder-lcr04.pdf>.

MPICH, <http://www-unix.mcs.anl.gov/mpi/mpich>.

Mucci, PJ 2004, 'Memory bandwidth and the performance of scientific applications: a study of the AMD Opteron™ processor', *Advanced Micro Devices*, <http://whitepapers.techrepublic.com.com/whitepaper.aspx?docid=117213>.

Netlib(a), <http://www.netlib.org/benchmark/hpl>.

Netlib(b), <http://www.netlib.org/benchmark/hpl/faqs.html>.

NetPIPE, <http://www.scl.ameslab.gov/netpipe>.

Nguyen, KN, & Le, TT 2003, 'Evaluation and comparison performance of various MPI implementations on an OSCAR Linux cluster', in *Proceedings of the International Conference on Information Technology: Computers and Communications 2003 (ITCC.03)*, pp. 310–314, IEEE Computer Society Press, <http://ieeexplore.ieee.org/iel5/8532/26947/01197546.pdf>.

Nieplocha, J, & Carpenter, B 1999, 'ARMCI: a portable remote memory copy library for distributed array libraries and compiler run-time systems', in *Proceedings of the 3rd Workshop on Runtime Systems for Parallel Programming 1999 (RTSPP)*, <http://ipdps.cc.gatech.edu/1999/rtspp/nieploch.pdf>.

Nieplocha, J, Harrison, R & Littlefield, R 1994, 'Global arrays: a portable "shared-memory" programming model for distributed memory computers', in *Proceedings of Supercomputing'94*, p. 340–349, IEEE Computer Society Press, <http://www.emsl.pnl.gov/docs/global/papers/super94.pdf>.

Nieplocha, J, Harrison, R & Littlefield, R 1996, 'Global Arrays: a nonuniform memory access programming model for high-performance computers', *The Journal of Supercomputing,* vol. 10, pp. 169–189.

Nieplocha, J, Foster, I & Kendall, RA 1998, 'ChemIO: high performance parallel I/O for computational chemistry applications', *International Journal of High Performance Computing Applications,* vol. 12, pp. 345–363.

Nieplocha, J, Ju, J & Straatsma, TP 2000, 'A multiprotocol communication support for the global address space programming model on the IBM SP', in *Proceedings of the 6th International Euro-Par Conference on Parallel Processing 2000*, eds, A. Bode *et al*. Lecture Notes in Computer Science 1900 (2000), pp. 718-728, <http://www.springerlink.com/content/jkyfwjplmwrrmwaj/fulltext.pdf>.

Nieplocha, J, Ju, J & Apra, E 2001, 'One-sided communication on the Myrinet-based SMP clusters using the GM message-passing library', in *Proceedings of the 15th International Parallel and Distributed Processing Symposium 2001 (IPDPS'01)*, pp. 1707-1716, IEEE Computer Society Press, <http://ieeexplore.ieee.org/iel5/7373/20001/00925158.pdf>.

Nieplocha, J *et al.* 2002a, 'Combining distributed and shared memory models: approach and evolution of the Global Arrays Toolkit', <http://www.emsl.pnl.gov/docs/global/papers/jarek.pdf>.

Nieplocha, J *et al.* 2002b, 'Protocols and strategies for optimizing performance of remote memory operations on clusters', in *Proceedings of the 16th International Parallel and Distributed Processing Symposium 2002 (IPDPS'02)*, IEEE Computer Society Press, pp. 164–173, <http://ieeexplore.ieee.org/iel5/7926/21854/01016563.pdf>.

Sokolowski, PJ & Grosu, D 'Performance considerations for network switch fabrics on Linux clusters', in *Proceedings of the 16th IASTED International Conference on Parallel and Distributed Computing and Systems 2004 (PDCS 2004)*, pp. 150–156, <https://www.grid.wayne.edu/WSU_Campus_Grid/Publications/papers/IASTED_PDCS_2004_Final.pdf>.

PVFS, <http://www.pvfs.org>.

Sloan, JD 2005, *High performance Linux clusters with OSCAR, Rocks, openMosix, and MPI*, O'Reilly, Sebastopol, CA.

Smirni, E, & Reed, DA 1997, 'Workload characterization of input/output intensive parallel applications', in *Proceedings of the 9th International Conference on Modeling Techniques and Tools for Computer Performance Evaluation 1997*, <http://citeseer.ist.psu.edu/cache/papers/cs/577/http:zSzzSzvibes.cs.uiuc.eduzSzPublicationszSzPaperszSzTools97.pdf/reed97workload.pdf>.

Steinke, T 2000, 'Tools for parallel quantum chemistry software, modern methods and algorithms of quantum chemistry', in *Proceedings*, 2nd edn, ed, J Grotendorst, John von Neumann Institute for Computing, Jülich, *NIC Series*, vol. 3, pp. 67–96, 2000, <http://www.fz-juelich.de/nic-series/Volume3/steinke.pdf>.

Thakur, R, Lusk, E & Gropp, W 1998, 'I/O in parallel applications: the weakest link', *the International Journal of High Performance Computing Applications,* vol. 12, pp. 389–395.

Thakur, R, Gropp, W & Lusk, E 1999, 'On implementing MPI-IO portably and with high performance', in *Proceedings of the 6th Workshop on I/O in Parallel and Distributed Systems 1999*, ACM Press, pp. 23–32, <http://citeseer.ist.psu.edu/cache/papers/cs/4162/ftp:zSzzSzinfo.mcs.anl.govzSzpubzSztech_reportszSzreportszSzP732.pdf/thakur99implementing.pdf>.

Tipparaju, V *et al.* 2004, 'Host-assisted zero-copy remote memory access communication on InfiniBand', in *Proceedings of the 18th International Parallel and Distributed Processing Symposium 2004 (IPDPS'04)*, IEEE Computer Society Press, pp. 31–40, <http://ieeexplore.ieee.org/iel5/9132/28950/01302943.pdf?isnumber=&arnumber=1302943>.

Turner, D & Chen, X 2002, 'Protocol-dependent message-passing performance on Linux clusters', in *Proceedings of the IEEE International Conference on Cluster Computing 2002 (CLUSTER'02),* IEEE Computer Society Press, pp. 187–194, <http://ieeexplore.ieee.org/iel5/8231/25385/01137746.pdf?isnumber=&arnumber=1137746>.

Ubik, S & Cimbal, P 2003, 'Achieving reliable high performance in LFNs', in *Terena Networking Conference 2003 (TNC),* <http://www.terena.nl/events/archive/tnc2003/programme/papers/p4b2.pdf>.

Vilayannur, M *et al.* 2004, 'On the performance of the POSIX I/O interface to PVFS', in *Proceedings of the 12th Euromicro Conference on Parallel, Distributed and Network-Based Processing 2004 (EUROMICRO-PDP'04)*, IEEE Computer Society Press, pp. 332-339, <http://ieeexplore.ieee.org/iel5/8971/28471/01271463.pdf?isnumber=&arnumber=1271463>.

Nipah Virus Encephalitis — A Review

C.T. Tan[1]*, K.B. Chua[2] and K.T. Wong[3]

The Nipah virus was first discovered in 1999, following a severe outbreak of viral encephalitis among pig farm workers in Malaysia. The virus was thought to have spread from *Pteropus* bats to pigs, then from infected pigs to humans by close contact. Mortality of the disease was high at about 40%. The main necropsy finding was disseminated microinfarction associated with vasculitis and direct neuronal involvement. Relapsed encephalitis was seen in approximately 10% of those who survived the initial illness. Since its first recorded emergence in peninsular Malaysia, 10 outbreaks of Nipah virus encephalitis have been reported in Bangladesh and West Bengal in India. The outbreaks occurred from January to May, with *Pteropus giganteus* as the reservoir of the virus. In Bangladesh, evidence indicated that the virus transmitted directly from bats to human, with human to human transmission as an important mode of spread. The mortality of the illness was higher in Bangladesh which stood at around 70%. This was likely to be due to genetic variation of the virus.

From September 1998 to June 1999, there was an outbreak of a new viral encephalitis in several pig farming villages (Chua *et al*. 1999; Chua *et al*. 2000), mainly in the suburbs of Ipoh in the north, and Sungai Nipah and Bukit Pelanduk areas in central peninsular Malaysia. The outbreak subsequently spread to 11 abattoir workers in Singapore (Paton *et al*. 1999). In Malaysia, more than 265 patients were reported to have been infected, with more than 105 mortalities (Chua *et al*. 2000; Paton *et al*. 1999). If asymptomatic and mild infections were included, it was estimated that more than 350 people were infected (Wong *et al*. 2002). As the outbreak involved pig farm workers, the outbreak was initially thought to be due to the Japanese encephalitis virus. Isolation of a new paramyxovirus from the cerebrospinal fluid of several patients strongly indicated that this novel virus was the etiologic agent (Chua *et al*. 1999; Chua *et al*. 2000). The virus was subsequently named Nipah virus after Kampung Sungai Nipah because one of the early isolates was from a patient who resided in this village. Molecular amplification and partial sequencing of the viral phosphoprotein gene quickly established Nipah virus as a new paramyxovirus closely related to Hendra virus (Chua *et al*. 2000; Harcourt *et al*. 2000). Hendra virus was also a novel virus first isolated in 1994, that caused acute respiratory disease in horses and has so far been reported to infect six patients in Australia (Selvey *et al*. 1995; O'Sullivan 1997; Field 2009).

Since its first recorded emergence, seven outbreaks occurred in Bangladesh from 2001 to 2007 (Hossain *et al.* 2008; International Centre for Diarrheal Disease Research 2007), with two further outbreaks in February 2008. An outbreak in neighbouring Siliguri, West Bengal, India occurred in 2001 (Chadha *et al*. 2006), indicating that the Nipah virus may prove to be an important cause of fatal encephalitis over a wide geographical area. This is a review of the Nipah virus encephalitis with a new update of information about the disease found in the Indian subcontinent.

The Nipah Virus

Nipah virus shares many common characteristic features with other members of the *Paramyxoviridae* family, such as cytoplasmic inclusions of viral nucleocapsids and similar viral morphogenesis at the plasma membrane consisting of budding, pleomorphic enveloped viral particles filled with masses of nucleocapsids (Goldsmith *et al.* 2003; Hyatt *et al*. 2001). In negatively-stained preparations, viral nucleocapsids exhibit the typical 'herringbone' appearance characteristic for paramyxoviruses (Goldsmith *et al.* 2003; Chow *et al*. 2000).

The complete genome of the virus comprises of 18 246 nucleotides, that is 12 nucleotides longer than that of the Hendra virus. However, both the Nipah virus and Hendra virus have notably longer genomes than other members of the *Paramyxovirinae* subfamily that average about 15 500 nucleotides. The Nipah and Hendra virus are also very closely related with respect to their genomic end sequences, gene start and stop signals, P gene-editing signals and deduced amino acid sequences of all their respective proteins (Chan *et al*. 2001). A new genus, named *Henipavirus* (Hendra + Nipah), has been established to accommodate these two phylogenetically closely related viruses (Wong *et al*. 2000 & 2001).

[1] Department of Medicine, Faculty of Medicine, University of Malaya, 50603 Kuala Lumpur, Malaysia
[2] Department of Medical Microbiology, Faculty of Medicine, University of Malaya, 50603 Kuala Lumpur, Malaysia
(Current address: National Public Health Laboratory, Ministry of Health, Malaysia)
[3] Department of Pathology, Faculty of Medicine, University of Malaya, 50603 Kuala Lumpur, Malaysia
* Corresponding author (e-mail: chongtin.tan@gmail.com)

Epidemiology

Fruitbats of Pteropid species were thought to be the reservoir that transmitted the virus to the pigs in the Malaysian outbreak (Mohd 2001). Close contact with infected pigs and even infected dogs was thought to be responsible for viral transmission to humans via respiratory droplet nuclei (Parashar *et al*. 2000; Tan *et al*. 1999; Chew *et al.* 2000). Transmission to health-care workers was thought to be generally low (Mounts *et al*. 2001), although a nurse who previously cared for Nipah virus encephalitis patients subsequently seroconverted and her MRI brain scans showed typical multiple, discrete high signal lesions. She was asymptomatic (Tan *et al*. 2001). The isolation of Nipah virus from patients' respiratory secretions and urine indicates that human-to-human transmission is possible (Chua *et al.* 2001).

In the Bangladesh outbreaks, the mode of transmission from bats to human was still unclear. Contact with sick cows and pigs were speculated to be the mode of transmission in the 2001 outbreak in Meherpur, and the 2003 outbreak in Naogaon districts (Hsu *et al.* 2004). Human to human transmission was thought to be an important mode in the 2004 outbreak in Faridpur (Gurley *et al.* 2007), as well as the 2001 and 2003 outbreaks in Bangladesh. Viral transmission in a healthcare setting in the 2001 outbreak in Siliguri, India also suggested human-to-human spread (Chadha *et al.* 2006). In the 2005 outbreak in Tangail, Bangladesh, drinking contaminated raw date palm sap was significantly associated with encephalitis (Luby *et al.* 2006). Thus unlike the Malaysian outbreak, in most outbreaks in Bangladesh, it appeared that viral transmission from bats to humans occurred without involvement of intermediate animal hosts, and human-to-human spread was an important mode of transmission in Bangladesh and India

The Bat as Reservoir Host

There is now good evidence that the reservoir hosts of Nipah virus in Malaysia are the Pteropid fruitbats (*Pteropus vampyrus* and *Pteropus hypomelanus*) (Mohd *et al.* 2001). In Tioman Island, off the east coast of peninsular Malaysia, Nipah virus has been isolated from the urine of roosting bats (Chua *et al.* 2002). However, early attempts to isolate virus or amplify viral sequences from tissue of bats caught in peninsular Malaysia around the outbreak epicenters in the suburbs of Ipoh and other parts of peninsular Maalysia were unsuccessful (Mohd *et al.* 2001). Serum neutralizing antibodies were found in 4% – 31% of bat species, including those from Tioman Island (Mohd *et al.* 2001). Contaminated fruits partially-eaten by bats that dropped into pig-sties were hypothesized to contain enough virus to infect the pigs that consumed these fruits (Chua *et al.* 2002). Infected pigs were the main role amplifying hosts and the close proximity of pigs in most Malaysian farms probably contributed significantly to pig-to-pig transmission.

Field studies in Malaysia showed a complex interplay of multiple factors such as reduction of wildlife habitat due to deforestation, prolonged El Nino-related drought, severe haze from anthropogenic forest fires, mixed agro-pig farming practices and poor design of pig-sties that led to virus spillover from bats to pigs as early as 1997, and subsequently from pigs to humans (Chua *et al.* 2002).

Pteropus giganteus, being the only Pteropus species in Bangladesh, is widely distributed throughout the country (Bates & Harrison 1997). Following the Naogoan outbreak, it was shown that two out of ten bats had antibodies against the Nipah virus, thus these bats are also likely to be reservoir hosts for Nipah virus in the Bengal region (Hsu *et al.* 2004). All the previous outbreaks have occurred between January and May and this may be related to a seasonal increase in virus shedding among bats or to bat attraction to seasonal agricultural foods (e.g. date palm juice) available, bringing bats into closer proximity with humans (Luby *et al.* 2006).

Clinical Manifestations

More than half of the 94 patients with symptomatic Nipah virus infection treated in University of Malaya Medical Centre had infected family members indicating a disease of high infection rate (Goh *et al.* 2000). The ratio of symptomatic to subclinical infection was estimated to be 3:1 (Tan *et al.* 1999).

The incubation period was estimated to be of less than two weeks in 92% of the patients (Goh *et al.* 2000). The clinical manifestation was that of acute encephalitis characterized by fever, headache, vomiting and reduced level of consciousness (Chua *et al.* 1999; Paton *et al.* 1999; Goh *et al.* 2000; Lee *et al.* 1999). Distinctive clinical features were areflexia, hypotonia, tachycardia, hypertension, and segmental myoclonus in 32% of the patients. Myoclonus was characterized by focal, rhythmic jerking of diaphragmatic and anterior neck muscles (Goh *et al.* 2000).

Respiratory tract involvement with cough was seen in 14% of the patients (Chong *et al.* 2000). Paton *et al* reported that three of their 11 patients from Singapore had atypical pneumonia with abnormal chest X-rays. There were some patients who had no clinical presentation of central nervous system (CNS) infection but had seroconverted and showed other systemic symptoms. Of the 94 patients admitted to University Malaya Medical Centre, 91 had acute encephalitis and three had non-CNS infection (Goh *et al.* 2000).

The overall mortality from acute Nipah virus encephalitis was 40% (Chua *et al.* 2000). Severe brain stem involvement as suggested by the presence of tachycardia, hypertension and abnormal doll's-eye reflex appeared to be associated with poor prognosis (Goh *et al.* 2000; Chong *et al.* 2000). Presence of virus in the cerebrospinal fluid, which indicated

high viral replication in the CNS, was also associated with high mortality (Chua *et al.* 2000). Concomitant diabetes mellitus, but not the level of exposure to sick animals, was also related to higher mortality, probably due to immunoparesis (Chong *et al.* 2001).

Though most of the known outbreaks involved mainly adults, two outbreaks in Bangladesh (Naogoan 2003; Rajbari 2004) occurred primarily among younger patients with a median age of 12 years (Hossain *et al.* 2008). This was likely to be related to the mode of transmission of the infection. Climbing trees was found to be an important risk factor in the Rajbari outbreak which might have exposed the children to bats (Montgomery *et al*. 2008). The clinical features of Bangladeshi and Indian patients which manifested mainly as acute fatal encephalitis with fever, coma, seizure and short incubation periods were reported to be similar to that of Malaysian patients (Hossain *et al.* 2008). However, there was no report of segmental myoclonus among the Bangladeshi and Indian patients which was a prominent feature among Malaysian patients (Goh *et al.* 2000). The prominent lung changes found in Bangladesh but not in Malaysian patients were consistent with acute respiratory distress syndrome (Hossain *et al.* 2008). This is likely to be directly related to the human-to-human spread of the disease in Bangladesh (Gurley *et al.* 2007). Distance to health care facilities and changes in virulence may account for the higher mortality in Bangladesh and India (about 70%) compared to 40% in the Malaysian outbreak (Chua *et al.* 2000; Hossain *et al.* 2008; Chadha *et al.* 2006).

Laboratory, Radiologic and other Diagnostic Investigations

In the Malaysian outbreak, the cerebrospinal fluid (CSF) examination was abnormal in 75% of the patients with elevated levels of protein and/or white cell counts. Glucose levels were within normal limits (Goh *et al.* 2000; Chong *et al.* 2000). These features were non-specific and might be found in many primary viral encephalitis.

Anti-Nipah virus IgM and IgG antibody detection in serum and CSF were critical to diagnosis of infection. The anti-Nipah virus IgM antibody test utilized a subtractive IgM-capture enzyme-linked immunosorbent assay (ELISA) format while anti-Nipah virus IgG antibodies were detected by an indirect IgG ELISA assay (Chua *et al.* 1999). The ELISA tests are useful as a screening test (Daniels , Ksizek & Eaton 2001). The rate of positive IgM was 60%–71% by day 4 and 100% by day 12 of illness. For IgG, it was 7%–29% by day 1–10 and 100% by day 25–26 of illness (Ramasundram *et al.* 1999).

Brain magnetic resonance (MR) imaging proved to be a useful diagnostic aid for acute encephalitis (Ahmad *et al.* 2000) due to Nipah virus. Typically, the brain MR showed multiple, disseminated, small discrete hyperintense lesions best seen in the FLAIR sequence mainly in subcortical and deep white matter, and occasionally in the cortex. The lesions which measured about 2 mm – 7 mm were likely to correspond to the micro-infarctions noted in post-mortem tissue. Similar changes were also seen in 16% of asymptomatic patients, indicating that subclinical involvement of the CNS may not be uncommon (Tan *et al.* 2000).

The most common electro-encephalographic abnormality was continuous diffuse, symmetrical slowing with or without focal discharges. The degree of slowing correlated with the severity of disease. Independent bitemporal periodic complexes was common among those deeply comatosed and was associated with 100% mortality (Chew *et al.* 1999).

Reports from Bangladesh showed that half of the patients had normal CSF (Hossain *et al.* 2008; Quddus *et al.* 2004). One report of brain MRI findings from Bangladesh showed confluent high signal lesions in both gray and white matter in three patients with acute encephalitis (Quddus *et al.* 2004). This appears to be different from Malaysian patients where disseminated multiple discrete high-signal-intensity lesions were the universal finding (Ahmad *et al.* 2000). Whether or not this is related to the fact that the Nipah virus isolated in Bangladesh was not identical (only 92% homology) to the Malaysian isolates, is unknown (Harcourt *et al.* 2005).

Treatment

Ribavirin, a very broad-spectrum anti-viral agent, was tried on an empirical basis on Nipah virus infected patients during the outbreak in Malaysia. In an open-label trial of 140 patients with 54 patients as control (patients who refused treatment or otherwise not given the drug), there were 45 deaths (32%) in the ribavirin group versus 29 deaths (54%) in the control arm. This represented a reduction in mortality of 36%. Although this trial was disadvantaged by the use of historical controls, it does indicate that ribavirin may be useful in the treatment of acute Nipah virus encephalitis. There was no apparent serious side effects encountered in this study (Chong *et al.* 2001).

Pathology and Pathogenesis of Acute Nipah Virus Infection

Pathological studies of 31 fatal acute encephalitis cases from Malaysia demonstrated that direct damage to tissues occurred by two concurrent mechanisms. The first was ischaemic damage/micro-infarction and the second was direct viral cytolysis of parenchymal cells (Chua *et al.* 1999; Chua *et al.* 2000; Wong *et al.* 2002).

The ischaemic damage/micro-infarction followed infection of blood vessels in the major organs, including the

brain, lung and kidney. The earliest evidence of infection seemed to be the formation of multinucleated syncytium in the endothelium of the blood vessel. More commonly, vascular infection/damage took the form of endothelial ulceration with varying degrees of inflammation and fibrinoid necrosis. The inflammatory cells consisted of neutrophils, macrophages and other cells found within the vascular wall. Vasculitis which was frequently associated with thrombosis and vascular occlusion, resulted in ischaemia and/or micro-infarction. Staining by immunohistochemistry often demonstrated the presence of viral antigen within endothelium, endothelial syncytium and tunica media. These findings confirmed that Nipah virus was able to infect blood vessels directly.

In the central nervous system, the meninges whose gray and white matter showed widespread vascular lesions was the most severely affected organ. The vasculitic vessels, with or without thrombosis, were often found adjacent to micro-infarcts. The surviving neurons in these areas might reveal paramyxoviral-type inclusions, confirmed to have Nipah viral antigens by immunohistochemistry. Parenchymal inflammation consisting of perivascular cuffing and neuronophagia could be seen particularly in patients that died after more than a week of illness.

Outside the central nervous system, with the exception perhaps of the liver, vasculitis and parenchymal lesions could be found in all the major organs, including the lung, kidney and heart. After the central nervous system, the most severely affected organ was the lung in which focal fibrinoid necrosis of the lung parenchyma associated with vasculitis was encountered. In addition, there was inflammation associated with multinucleated giant cells in the alveolar spaces. Pathologic changes in the kidney were characterized mainly be vasculitis and glomerular lesions consisting of microthrombi, scattered inflammatory cells and occasionally multinucleated syncytial cells. Occasionally, in the lymphoid organs such as lymph node and spleen, multinucleated syncytial cells could be found. Viral antigen was detected in affected tissue.

Relapsed and Late-onset Nipah Encephalitis

Most unexpectedly, a small number of Malaysian patients suffered a second or even a third neurologic episode following what appeared to be complete recovery (Tan *et al.* 2002; Chong & Tan *et al.* 2003). These relapsed Nipah virus encephalitis patients constitute 9% of the total number of survivors (Chong & Tan *et al.* 2003). In addition, about 5% who were either asymptomatic or only had mild non-encephalitic illness initially, also developed similar neurologic episodes (late-onset Nipah encephalitis) for the first time several months later. Clinical, radiologic and pathological findings indicated that essentially relapsed and late-onset Nipah virus encephalitis was the same disease process that was distinct from the original infection of acute Nipah virus encephalitis. The common clinical features were fever, headache, seizures and focal neurological signs. It was associated with 18% mortality. MR imaging typically showed patchy areas of confluent cortical lesions (Tan *et al.* 2002). There was reduction in the frequency of relapsed and late-onset Nipah virus encephalitis with progression of time, with the relapsed or late-onset encephalitis manifesting up to 53 months after the initial infection (Chong & Tan *et al.* 2003). Based on brain MR findings alone, it appeared that the Bangladeshi patients with acute encephalitis had findings that were more typical of relapsed/late onset encephalitis. These findings might be explained by the possibility that acute encephalitis in these patients was followed very soon by relapsed/late onset encephalitis without any intervening recovery.

Necropsy showed focal, 'confluent' encephalitis in which the demonstration of neuronal viral antigen in brains indicated that relapsed and late-onset Nipah encephalitis were due to a recurrent infection rather than post infectious demyelination as described following other viral infections (Chong *et al.* 2001). Relapsed Nipah virus encephalitis is probably analogous to the single human case of Hendra virus meningo-encephalitis in which 13 months following initial infection the patient developed fatal meningo-encephalitis (O'Sullivan *et al.* 1997). Hendra virus antigen was demonstrated in the brain tissues. Nonetheless in both relapsed Nipah virus encephalitis as well as Hendra virus encephalitis, the respective viruses have not been isolated thus far (O'Sullivan *et al.* 1997; Tan *et al.* 2002).

As for the patients from Bangladesh, a study on the 22 survivors of Nipah virus encephalitis showed that four developed new neurological symptoms months to years after the acute illness. Three patients had extraocular motor palsies, and one had cervical dystonia (Sejvar *et al.* 2007). However, none of the surviving Bangladesh patients had acute catastrophic relapse encephalitis, as seen among some of the Malaysian patients.

Development of Vaccine

There was an early sentiment to develop a Nipah virus vaccine for livestock to prevent the re-emergence of the virus. An early candidate recombinant vaccinia virus vector-carrier vaccine carrying Nipah virus fusion (F) and attachment (G) proteins has been developed which was found to have a protective effect on hamsters against a lethal challenge of the Nipah virus (Guillaume *et al.* 2004). Related candidate Nipah virus vaccines have also been developed which were found to induce production of neutralizing antibodies (Weingart *et al.* 2006; Mungall *et al.* 2006). However, as was normally the case for other zoonotic diseases from wildlife, good surveillance and culling of the infected domestic animal population may be the most cost-effective and rapid measure for controlling the spread of the disease. In addition, necessary measures could be

taken to prevent the re-emergence of the virus with a better understanding of wild animal reservoirs, factors for its spillover to domestic animals and subsequently to humans. Hence, it is probably more logical to develop a simpler, more sensitive and specific laboratory test which does not require biosafety level 3 facilities for rapid diagnosis and surveillance. However, wildlife vaccination has played an important role in controlling rabies in some countries.

Distribution of Pteropus Bats and Implication of Future Outbreaks

The distribution of fruit bats of the Pteropid species is widespread; extending from Madagascar, India, Bangladesh, Myanmar, Thailand and the Indochina region to the Philippines, and south to include all of western Indonesia as far as Timor, Sumba and Suva including Australia (Medway *et al.* 1978). Antibodies against the Nipah virus in serum has been found in at least 10 genera and 23 species of bats in a large part of Asia and Africa — a region that stretches from Australia and southern China, and from Indonesia to as far west as Ghana (Chong *et al.* 2009). Countries in the region need to strengthen their surveillance programme and laboratory diagnostic capabilities for the possible re-emergence of Nipah virus and other possible exotic viruses, such as Menangle virus, Tioman virus, Pulau virus and Melaka virus from these fruit bats (Chua *et al.* 2007).

CONCLUSION

From the original outbreak in Malaysia with the infection spreading from bats to pigs to human, Nipah virus has appeared in unexpected places, causing repeated outbreaks in Bangladesh and India without requiring a pig intermediate, and with human-to-human infection.

Date of submission: September 2007
Date of acceptance: August 2009

REFERENCES

Ahmad SS *et al*. 2000, 'Magnetic resonance imaging features of Nipah encephalitis', *American Journal of Roentgenology*, vol. 175, pp. 437–442.

Bates, PJJ & Harrison, D 1997, 'Bats of the Indian subcontinent', Sevenoaks (UK): Harrison Zoological Museum.

Chadha, MS *et al.* 2006, 'Nipah virus-associated encephalitis outbreak, Seliguli, India', *Emerging Infectious Diseases*, vol. 12, pp. 235–240.

Chan, YP *et al*. 2001, 'Complete nucleotide sequences of Nipah virus isolates from Malaysia', *Journal of General Virology*, vol. 82, pp. 2151–2155.

Chew, NK *et al*. 1999, 'Electroencephalography in acute Nipah encephalitis', *Neurological Journal of Southeast Asia*, vol. 4, pp. 45–51.

Chew, MHL *et al*. 2000, 'Risk factors for Nipah virus infection among abattoir workers in Singapore', *Journal of Infectious Diseases*, vol. 181, pp. 1760–1763.

Chua, KB *et al*. 1999, 'Fatal encephalitis due to Nipah virus among pig-farmers in Malaysia', *Lancet*, vol. 354, pp.1257–1259.

Chua, KB *et al*. 2000a, 'Nipah virus: a recently emergent deadly paramyxovirus', *Science*, vol. 288, pp. 1432–1435.

Chua, KB *et al*. 2000b, 'High mortality in Nipah encephalitis is associated with presence of virus in cerebrospinal fluid', *Annals of Neurology*, vol. 48, pp. 802–805.

Chua, KB *et al*. 2001, 'The presence of Nipah virus in respiratory secretions and urine of patients during an outbreak of Nipah virus encephalitis in Malaysia', *Journal of Infection*, vol. 42, pp. 40–43.

Chua, KB *et al*. 2002, 'Isolation of Nipah virus from Malaysian flying-foxes', *Microbes and Infection*, vol. 4, pp. 145–151.

Chua, KB, Chua, BH & Wang, CW 2002a, 'Anthropogenic deforestation, El Nino and the emergence of Nipah virus in Malaysia', *Malaysian Journal of Pathology*, vol. 24, pp. 15–21.

Chua, KB *et al.* 2007, 'A previously unknown reovirus of bat origin is associated with an acute respiratory disease in humans', in *Proceedings of National Academy of Science*, vol. 104, pp. 11424–11429.

Chong, HT *et al*. 2000, 'Nipah encephalitis outbreak in Malaysia, clinical features in patients from Seremban', *Neurological Journal of Southeast Asia*, vol. 5, pp. 61–67.

Chong, HT *et al*. 2001, 'Occupational exposure, age, diabetes mellitus and outcome of acute Nipah encephalitis', *Neurological Journal of Southeast Asia*, vol. 6, pp. 7–11.

Chong, HT *et al.* 2001, 'Treatment of acute Nipah encephalitis with Ribavirin', *Annals of Neurology*, vol. 49, pp. 810–813.

Chong, HT & Tan, CT 2003, 'Relapsed and late-onset Nipah encephalitis, a report of three cases', *Neurology Asia*, vol. 8, pp. 109–112.

Chong, HT, Abdullah, S & Tan, CT 2009, 'Nipah virus and bats', *Neurology Asia*, vol. 14, no. 1, pp. 73–76.

Chow, VT *et al*. 2000, 'Diagnosis of Nipah virus encephalitis by electron microscopy of cerebrospinal fluid', *Journal of Clinical Virology*, vol. 19, no. 3, pp. 143–147.

Daniels, P *et al.* 2001, 'Laboratory diagnosis of Nipah and Hendra infections', *Microbes and Infection*, vol. 3, pp. 289–295.

Field, H 2009, 'Hendra virus infection risks', *Neurology Asia 2009*, vol. 14, no. 1, pp. 77–78.

Guillaume, V *et al*. 2004, 'Nipah virus: vaccination and passive protection studies in a hamster model', *Journal of Virology*, vol. 78, no. 2, pp. 834–840.

Goldsmith, CS *et al*. 2003, 'Elucidation of Nipah virus morphogenesis and replication using ultrastructural and molecular approaches', *Virus Research*, vol. 93, pp. 89–98.

Goh, KJ *et al*. 2000, 'Clinical features of Nipah virus encephalitis among pig farmers in Malaysia', *New England Journal of Medicine*, vol. 342, pp. 1229–1235.

Gurley, ES *et al.* 2007, 'Person-to-person transmission of Nipah virus in a Bangladeshi community', *Emerging Infectious Diseases*, vol. 13, no. 7, pp. 1031–1036.

Harcourt, B *et al*. 2000, 'Molecular characterization of Nipah virus, a newly emergent paramyxovirus', *Virology*, vol. 271, pp. 334–349.

Harcourt, BH *et al.* 2005, 'Genetic characterization of Nipah virus, Bangladesh, 2004', *Emerging Infectious Diseases*, vol. 11, pp. 1594–1597.

Hossain, MJ *et al*. 2008, 'Clinical presentation of Nipah virus infection in Bangladesh', *Clinical Infectious Diseases*, vol. 46, pp. 977–984.

Hsu, VP *et al.* 2004, 'Nipah virus encephalitis reemergence, Bangladesh', *Emerging Infectious Diseases*, vol. 10, no. 12, pp. 2082–2087.

Hyatt, AD *et al.* 2001, 'Ultrastructure of Hendra virus and Nipah virus within cultured cells and host animals', *Microbes and Infection*, vol. 3, no. 4, pp. 297–306.

International Centre for Diarrheal Disease Research, Bangladesh 2003, 'Outbreak of encephalitis due to Nipah/Hendra-like viruses, western Bangladesh', *Health and Science Bulletin*, vol. 1, no. 5, pp. 1–6.

International Centre for Diarrheal Disease Research, Bangladesh 2007, 'Person-to-person transmission of Nipah infection in Bangladesh, 2007', *Health and Science Bulletin*, vol. 5, no. 4, pp. 1–6.

Lee, KE *et al*. 1999, 'The neurological manifestations of Nipah virus encephalitis, a novel paramyxovirus', *Annals of Neurology*, vol. 46, pp. 428–432.

Luby, SP *et al.* 2006, 'Foodborne transmission of Nipah virus, Bangladesh', *Emerging Infectious Diseases*, vol. 12, pp. 1888–1894.

Medway, L 1978, 'The Wild Mammals of Malaya (Peninsular Malaysia) and Singapore', Kuala Lumpur: Oxford University Press.

Mohd YJ *et al.* 2001, 'Nipah virus infection in bats (order Chiroptera) in Peninsular Malaysia', *Emerging Infectious Diseases*, vol. 7, pp. 439–441.

Mungall, BA *et al.* 2006, 'Feline model of acute Nipah virus infection and protection with a soluble glycoprotein-based subunit vaccine', *Journal of Virology*, vol. 80, pp. 12293–12302.

Mounts, AW *et al*. 2001, 'A cohort study of health-care workers to assess nosocomial transmissibility of Nipah virus, Malaysia, 1999', *Journal of Infectious Diseases*, vol.183, pp. 810–813.

Montgomery, JM *et al*. 2008, 'Risk factors for Nipah virus encephalitis in Bangladesh: results of a matched case-control study', *Emerging Infectious Diseases*, vol. 14, pp. 1526–1532.

O'Sullivan, JD *et al*. 1997, 'Fatal encephalitis due to novel paramyxovirus transmitted from horses', *Lancet*, vol. 349, pp. 93–95.

Parashar, UD *et al.* 2000, 'Case-control study of risk factors for human infection with the new zoonotic paramyxovirus, Nipah virus, during a 1998–1999 outbreak of severe encephalitis in Malaysia', *Journal of Infectious Diseases*, vol. 181, pp. 1755–1759.

Paton, N *et al.* 1999, 'Outbreak of Nipah-virus infection among abattoir workers in Singapore', *Lancet*, vol. 354, pp. 1253–1256.

Ramasundrum, V *et al.* 1999, 'Presence of CSF IgM do not have protective effect in Nipah encephalitis', *Neurological Journal of Southeast Asia*, vol. 4, pp. 73–76.

Selvey, L *et al*. 1995, 'Infection of humans and horses by a newly described morbillivirus', *Medical Journal of Australia*, vol. 162, pp. 642–645.

Sejvar, JJ *et al*. 2007, 'Long-term neurological and functional outcome in Nipah virus infection', *Annals of Neurology*, vol. 62, pp. 235–242.

Tan, KS, Tan, CT & Goh, KJ 1999, 'Epidemiological aspects of Nipah virus infection', *Neurological Journal of Southeast Asia*, vol. 4, pp. 77–81.

Tan, KS *et al.* 2000, 'Patients with asymptomatic Nipah virus infection may have abnormal cerebral MR imaging', *Neurological Journal of Southeast Asia*, vol. 5, pp. 69–73.

Tan, CT & Tan, KS 2001, 'Nosocomial transmissibility of Nipah virus', *Journal of Infectious Diseases*, vol. 184, pp. 1367.

Tan, CT *et al.* 2002, 'Relapsed and late-onset Nipah encephalitis', *Annals of Neurology*, vol. 51, pp.703–706.

Wang, LF *et al*. 2000, 'The exceptionally large genome of Hendra virus: support for creation of a new genus within the family Paramyxoviridae', *Journal of Virology*, vol. 74, pp. 9972–9979.

Wang, LF *et al*. 2001, 'Molecular biology of Hendra and Nipah viruses', *Microbes and Infection*, vol. 3, pp. 279–287.

Weingartl, HM *et al.* 2006, 'Recombinant Nipah virus vaccines protect pigs against challenge', *Journal of Virology*, vol. 80, pp. 7929–7938.

Wong, KT *et al*. 2002a, 'Nipah virus infection, an emerging paramyxoviral zoonosis', *Springer Semin Immunopathol*, vol. 24, pp. 215–228.

Wong, KT *et al*. 2002b, 'Nipah virus infection: Pathology and pathogenesis of an emerging paramyxoviral zoonosis', *American Journal of Pathology*, vol. 161, pp. 2153–2167.

Quddus, R *et al*. 2004, 'A report of 4 patients with Nipah encephalitis from Rajbari district, Bangladesh in the January 2004 outbreak', *Neurology Asia*, vol. 9, pp. 33–37.

MAHATHIR SCIENCE AWARD 2010

Invitation for Nominations

The Academy of Sciences Malaysia (ASM) is a body set up with a mission that encompasses pursuit, encouragement and enhancement of excellence in the fields of science, engineering and technology for the development of the nation and the benefit of mankind. The Academy has instituted the Mahathir Science Award (formerly known as ASM Award for Scientific Excellence in honour of Tun Dr Mahathir Mohamad) in recognition of scientists/ institutions who have contributed to cutting-edge tropical research that have had an impact on society.

This Award is Malaysia's most prestigious Science Award for tropical research launched in honour of Tun Dr Mahathir Mohamad who promoted and pursued with great spirit and determination his convictions in science and scientific research in advancing the progress of mankind and nations. Tun Dr Mahathir was the major force and the man who put into place much of the enabling mechanisms for a scientific milieu in our country.

This Award will be given to researchers who have made internationally recognised breakthroughs in pioneering tropical research in the fields of Tropical Medicine, Tropical Agriculture, Tropical Architecture and Engineering, and Tropical Natural Resources.

One Award will be conferred in 2010 covering any of the above four fields. The Award carries a cash prize of RM100 000, a gold medal and a certificate.

NOMINATION CRITERIA

- Awards will be given to researchers who have made internationally recognised breakthroughs in pioneering tropical research that have brought greater positive impacts on the well-being of society.
- Nominations can be made by individuals or institutions.
- A recipient could be an individual or an institution.

Nomination forms may be downloaded from the Academy's website:
www.akademisains.gov.my

Closing date: 31 March 2010

For more information, please contact:
Academy of Sciences Malaysia
902-4, Jalan Tun Ismail, 50480 Kuala Lumpur
Tel : 603-2694 9898; Fax : 603-2694 5858
E-mail: seetha@akademisains.gov.my
admin@akademisains.gov.my

22nd Pacific Science Congress

Asia Pacific Science in the New Millenium: Meeting the Challenges of Climate Change and Globalisation

13 –17 June 2011, Kuala Lumpur, Malaysia

The Congress will provide an inter-disciplinary platform for scientists from the region to discuss and review common concerns and priorities; bring together scientists from remote states; and serve as a catalyst for scientific and scholarly collaboration and to announce and establish new research initiatives. The Pacific Science Association (PSA) focuses on countries bordering the Pacific Ocean and the islands of the Pacific basin. PSA is a regional, non-governmental, and a scholarly organization that seeks to advance S&T in support of sustainable development in the Asia Pacific.

Sub-themes will include topics on:

- Impact on Large Marine Ecosystems
- Impact on Water & Food Systems
- Impact on Biodiversity & Ecosystem Services
- Ecological Economics
- Urbanization and the Health Challenge
- Energy for Sustainable Development
- Forces of Nature: Reducing Vulnerability to Hazards
- Monitoring and Assessment.

Schedule and Programme:

Both plenary and parallel sessions, invited lectures, poster sessions, with at least one session open to the public and an optional post-congress field excursion will be planned. Various symposia will also be organized around the sub-themes.

Enquiries:

Congress Secretariat
22nd Pacific Science Congress
c/o Academy of Sciences Malaysia
902-4, Jalan Tun Ismail
50480 Kuala Lumpur
Malaysia

Tel : (603) 2694 9898
Fax : (603) 2694 5858

e-mail: nasa@akademisains.gov.my; fardy@akademisains.gov.my
Website: www.akademisains.gov.my

ASM Publications

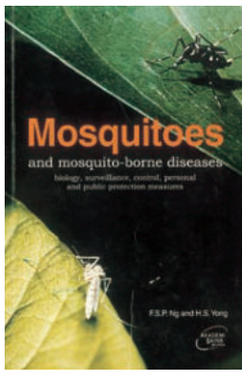

Mosquitoes and Mosquito-borne Diseases: Biology, Surveillance, Control, Personal and Public Protection Measures

F.S.P. Ng and *H.S. Yong (Editors)*
(2000)

ISBN 983-9445-05-7
Price: RM60.00 / USD20.00

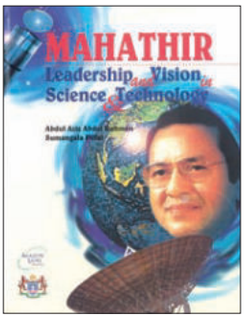

Mahathir: Leadership and Vision in Science and Technology

Abdul Aziz Abdul Rahman and *Sumangala Pillai*
(1996)

ISBN 983-9319-09-4
Price: RM100.00 / USD30.00

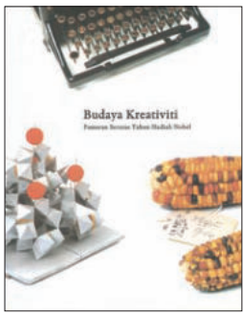

Budaya Kreativiti: Pameran Seratus Tahun Hadiah Nobel

Ulf Larsson (Editor)
(2004)

ISBN 983-9445-09-X
Price: RM50.00 / USD15.00

CD Kompilasi *Estidotmy*

Edisi 1 – 82, 2002–08
Price: RM35.00

Mahathir: Kepimpinan dan Wawasan dalam Sains dan Teknologi

Abdul Aziz Abdul Rahman
dan *Sumangala Pillai*
(1996)

ISBN 983-9319-09-4
Price: RM100.00 / USD30.00

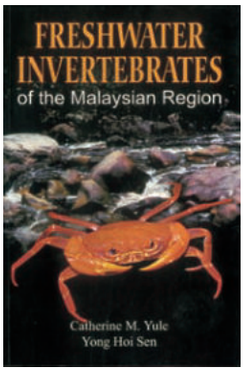

Freshwater Invertebrates of the Malaysian Region

Catherine M. Yule and *Yong Hoi Sen*
(2004)

ISBN 983-41936-0-2
Price: RM180.00 / USD52.00

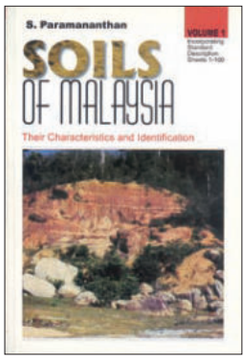

Soils of Malaysia: Their Characteristics and Identification (Vol. 1)

S. Paramananthan
(2000)

ISBN 983-9445-06-5
Price: RM100.00 / USD30.00

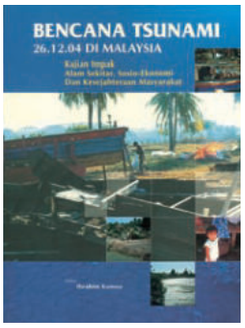

Bencana Tsunami 26.12.04 di Malaysia: Kajian Impak Alam Sekitar, Sosio-Ekonomi dan Kesejahteraan Masyarakat

Ibrahim Komoo (Editor)
(2005)

ISBN 983-9444-62-X
Price: RM100.00 / USD30.00

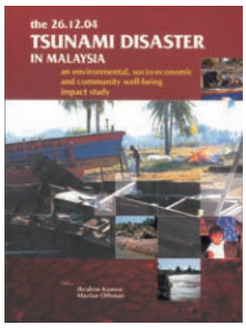

The 26.12.04 Tsunami Disaster in Malaysia: An Environmental, Socio-Economic and Community Well-being Impact Study

Ibrahim Komoo and *Mazlan Othman (Editors)*
(2006)

ISBN 983-9444-62-X
Price: RM100.00 / USD30.00

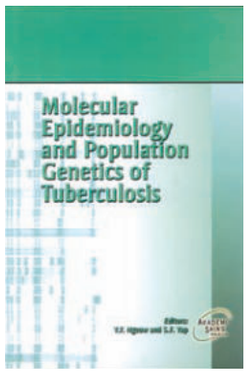

Molecular Epidemiology and Population Genetics of Tuberculosis

Y.F. Ngeow and *S.F.Yap (Editors)*
(2006)

ISBN 983-9445-14-6
Price: RM40.00 / USD12.00

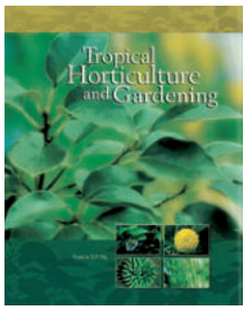

Tropical Horticulture and Gardening

Francis S.P. Ng
(2006)

ISBN 983-9445-15-4
Price: RM260.00 / USD75.00

Kecemerlangan Sains dalam Tamadun Islam: Sains Islam Mendahului Zaman
Scientific Excellence in Islamic Civilization: Islamic Science Ahead of its Time

Fuat Sezgin
(2006)

ISBN 983-9445-14-6
Price: RM40.00 / USD12.00

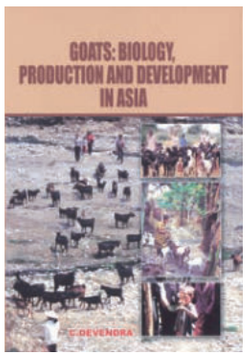

Goats: Biology, Production and Development in Asia

C. Devendra
(2007)

ISBN 978-983-9445-18-3
Price: RM180.00 / USD52.00

Proceedings: Seminar on Antarctic Research, 27–28 June 2005, University of Malaya, Kuala Lumpur, Malaysia

Irene K.P.Tan et al. *(Editors)*
(2006)

ISBN 978-983-9445-17-6
Price: RM40.00 / USD12.00

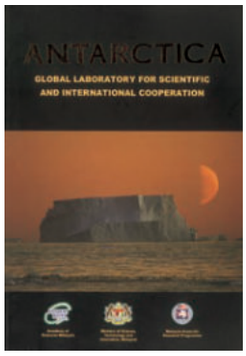

Antarctica: Global Laboratory for Scientific and International Cooperation

Aileen Tan Shau-Hwai et al. *(Editors)*
(2005)

ISBN 983-9445-13-8
Price: RM40.00 / USD12.00

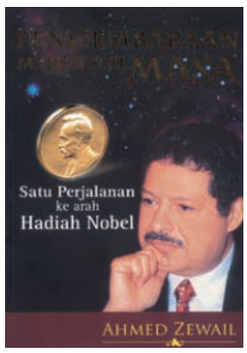

Pengembaraan Merentasi Masa: Satu Perjalanan ke Arah Hadiah Nobel

Ahmed Zewail
(2007)

ISBN 978-9445-20-6
Price: RM40.00 / USD12.00

ASM Publications

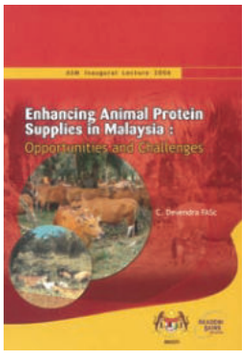

Enhancing Animal Protein Supplies in Malaysia: Opportunities and Challenges

C. Devendra
(2007)

ISBN 983-9444-62-X

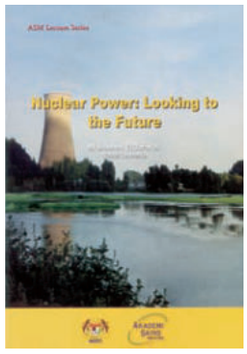

Nuclear Power: Looking to the Future

Mohamed ElBaradei
(2008)

ISBN 983-9445-14-6

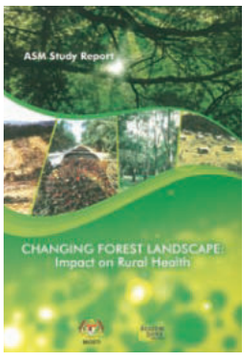

Changing Forest Landscape: Impact on Rural Health
(2007)

ISBN 983-9445-15-4

Dunia Sains
Vol. 5, No. 4, Oktober – Disember 2007
(2008)

A World of Science
Vol. 5, No. 4
October – December 2007

http://portal.unesco.org/science/en/ev.php-URL ID=5572&URL DO=DO TOPIC&URL SECTION=201.html

http://www. akademisains.gov.my/unesco/dunia_sains/okt_dis_2007.pdf

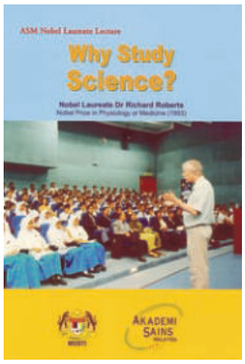

Why Study Science?

Richard Roberts
(2008)

ISBN 978-983-9445-18-3

Dunia Sains
Vol. 6, No. 1, Januari – Mac 2008
(2008)

A World of Science
Vol. 6, No. 1
January – March 2008

ASM Science Journal
Vol. 1, No. 1, June 2007

ISSN : 1823-6782

Price: RM100.00 / USD50.00 (Individual)
RM200.00 / USD100.00 (Institution)

ASM Science Journal
Vol. 1, No. 2, December 2007

ISSN : 1823-6782

Price: RM100.00 / USD50.00 (Individual)
RM200.00 / USD100.00 (Institution)

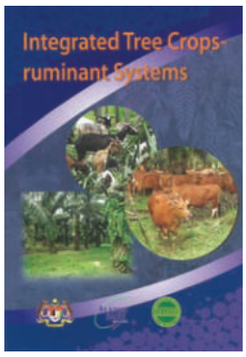

Integrated Tree Crops-ruminant Systems (Proceedings)

C. Devendra, S. Shanmugavelu and *Wong Hee Kum (Editors)*
(2008)

ISSN : 983-9445-24-3

Price: RM40.00 / USD12.00

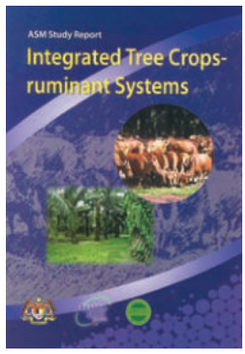

ASM Study Report: Integrated Tree Crops-ruminant Systems
(2008)

ISSN : 983-9445-24-4

Price: RM30.00 / USD9.00

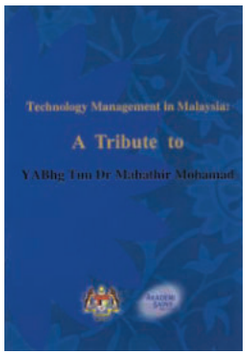

Technology Management in Malaysia: A Tribute to YABhg Tun Dr Mahathir Mohamad
(2008)

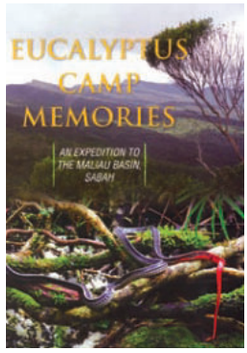

Eucalyptus Camp Memories: An Expedition to the Maliau Basin, Sabah
(2008)

ISSN : 978-983-9445-25-1

Price: RM220.00 / USD61.00 (Hard cover)
RM160.00 / USD42.00 (Soft cover)

ASM Science Journal
Vol. 2, No. 1, December 2008

ISSN : 1823-6782

Price: RM100.00 / USD50.00 (Individual)
RM200.00 / USD100.00 (Institution)

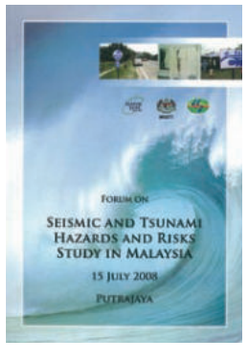

Forum on: Seismic and Tsunami Hazards and Risks Study in Malaysia 15 July 2008

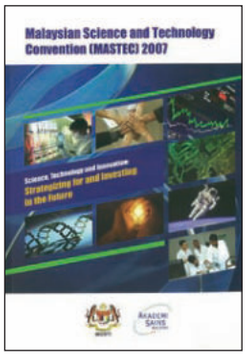

Science, Technology and Innovation: Strategizing for and Investing in the Future [Malaysian Science and Technology Convention (MASTEC) 2007]
(2009)

ISSN : 978-983-9445-27-5

Price: RM51.00 / USD22.00

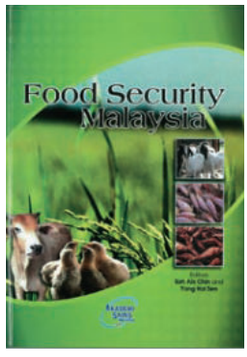

Food Security Malaysia (Proceedings)
Soh Aik Chin and Yong Hoi Sen (Editors)
(2009)

ISSN : 978-983-9445-28-2

Price: RM20.00 / USD6.00

ASM Publications

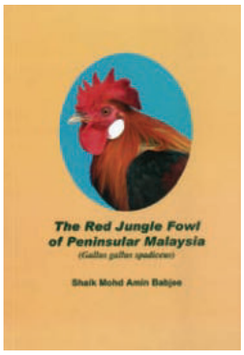

The Red Jungle Fowl of Peninsular Malaysia

Shaik Mohd Amin Babjee
(2009)

ISBN : 978-983-9445-29-9

Price: RM35.00 / USD12.00

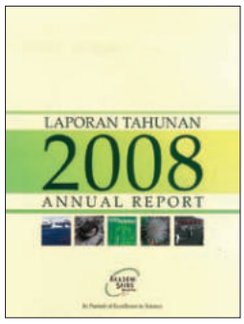

Academy of Science Malaysia

Annual Report 2008

Journal of Science & Technology in the Tropics

Vol. 4, No. 2, December 2008

ISSN:1823-5034

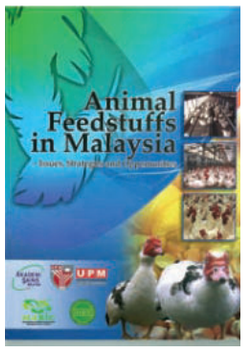

Animal Feedstuffs in Malaysia – Issues, Strategies and Opportunities
(2009)

ISBN : 978-983-9445-30-5

Price: RM35.00 / USD12.00

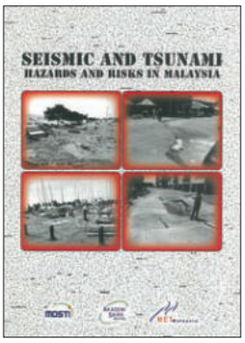

Seismic and Tsunami Hazards and Risks in Malaysia
(2009)

ISBN 978-983-9445-32-9

Price: RM45.00 / USD15.00

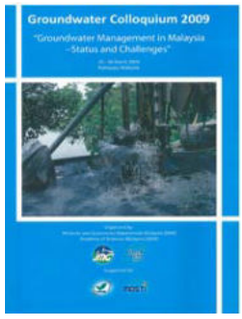

Groundwater Colloquium 2009 "Groundwater Management in Malaysia – Status and Challenges"

ISBN : 978-983-9445-30-5

Price: RM100.00 / USD75.00

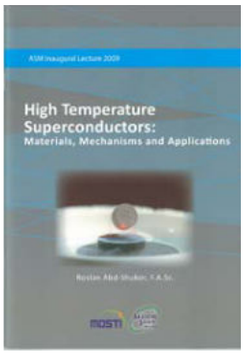

ASM Inaugural Lecture 2009
High Temperature Superconductors: Material, Mechanisms and Applications

ISBN : 978-983-9445-30-5

Price: RM20.00 / USD8.00

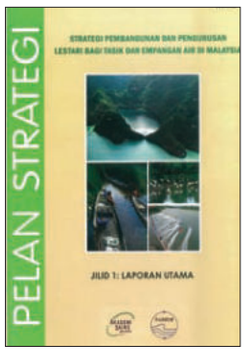

Pelan Strategi
Jilid 1: Laporan Utama

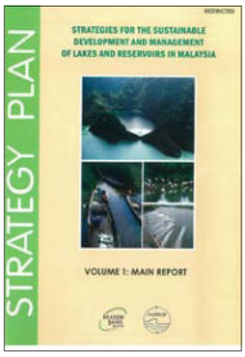

Strategy Plan
Volume 1: Main Report

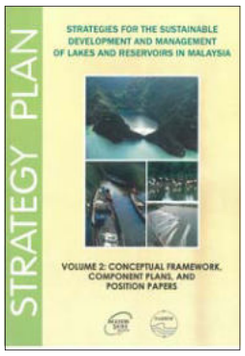

Strategy Plan
Volume 2: Conceptual Framework, Component Plans, and Position Papers

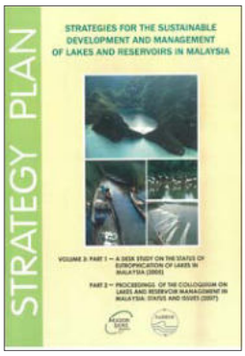

Strategy Plan
Volume 3: Part 1 & Part 2

ASM Science Journal
Vol. 2, No. 2, December 2008

ISSN : 1823-6782

Price: RM100.00 / USD50.00 (Individual)
RM200.00 / USD100.00 (Institution)

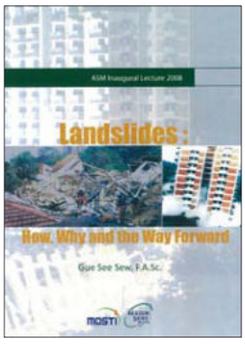

ASM Inaugural Lecture 2008
Landslides: How, Why and the Way Forward

ISBN : 978-983-9445-30-5

Price: RM20.00 / USD8.00

Journal of Science & Technology in the Tropics

Vol. 5, No. 1, June 2009

ISSN:1823-5034

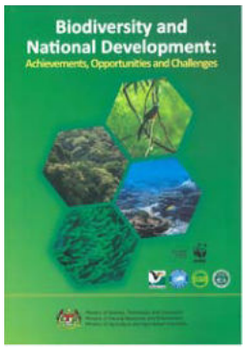

Biodiversity and National Development: Achievements, Opportunities and Challenges

ISBN : 978-983-9445-30-5

Price: RM40.00 / USD15.00

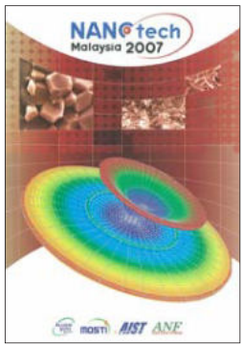

Nanotech Malaysia 2007

ISBN : 978-983-9445-30-5

Price: RM55.00 / USD20.00

Proceedings for the 3rd Malaysian International Seminar on Antarctica (MISA3) "From the Tropics to the Poles" 2007

ISBN : 978-983-9445-30-5

Price: RM40.00 / USD15.00

For purchasing, please access:
http://www.akademisains.gov.my

About the Journal

Mission Statement

To serve as the forum for the dissemination of significant research, S&T and R&D policy analyses, and research perspectives.

Scope

The ASM Science Journal publishes advancements in the broad fields of medical, engineering, earth, mathematical, physical, chemical and agricultural sciences as well as ICT. Scientific articles published will be on the basis of originality, importance and significant contribution to science, scientific research and the public.

Scientific articles published will be on the basis of originality, importance and significant contribution to science, scientific research and the public. Scientists who subscribe to the fields listed above will be the source of papers to the journal. All articles will be reviewed by at least two experts in that particular field. The journal will be published twice in a year.

The following categories of articles will be considered for publication:

Research Articles

Each issue of the journal will contain no more than 10 research articles. These are papers reporting the results of original research in the broad fields of medical, engineering, earth, mathematical, physical, chemical and life sciences as well as ICT. The articles should be limited to 6000 words in length, with not more than 100 cited references.

Short Communications

These are articles that report significant new data within narrow well-defined limits or important findings that warrant publication before broader studies are completed. These articles should be limited to 2000 words and not more that 40 cited references. Five (5) Short Communications will be accepted for publication in each issue of the journal.

Research Perspectives

These are papers that analyse recent research in a particular field, giving views on achievements, research potential, strategic direction etc. A Research Perspective should not exceed 2000 words in length with not more than 40 cited references.

Reviews/Commentaries

Each issue of the journal will also feature Reviews/ Commentaries presenting overviews on aspects such as Scientific Publications and Citation Ranking, Education in Science and Technology, Human Resources for Science and Technology, R&D in Science and Technology, Innovation and International Comparisons or Competitiveness of Science and Technology etc. Reviews/Commentaries will encompass analytical views on funding, developments, issues and concerns in relation to these fields and not exceed 5000 words in length and 40 cited references.

Science Forum

Individuals who make the news with breakthrough research or those involved in outstanding scientific endeavours or those conferred with internationally recognised awards will be featured in this section. Policy promulgations, funding, science education developments, patents from research, commercial products from research, and significant scientific events will be disseminated through this section of the journal. The following will be the categories of news:

- Newsmakers
- Significant Science Events
- Patents from Research
- Commercial Products from Research
- Scientific Conferences/Workshops/Symposia
- Technology Upgrades
- Book Reviews.

Instructions to Authors

The ASM Science Journal will follow the Harvard author-date style of referencing examples of which are given below.

In the text, reference to a publication is by the author's name and date of publication and page number if a quote is included, e.g. (Yusoff 2006, p. 89) or Yusoff (2006, p. 89) 'conclude.....' as the case may be. They should be cited in full if less than two names (e.g. Siva & Yusoff 2005) and if more than two authors, the work should be cited with first author followed by *et al*. (e.g. Siva *et al*. 1999).

All works referred to or cited must be listed at the end of the text, providing full details and arranged alphabetically. Where more than one work by the same author is cited, they are arranged by date, starting with the earliest. Works by the same author published in the same year are ordered with the use of letters a, b, c, (e.g. Scutt, 2003a; 2003b) after the publication date to distinguish them in the citations in the text.

General Rules

Authors' names:

- Use only the initials of the authors' given names.
- No full stops and no spaces are used between initials.

Titles of works:

- Use minimal capitalisation for the titles of books, book chapters and journal articles.
- In the titles of journals, magazines and newspapers, capital letters should be used as they appear normally.
- Use italics for the titles of books, journals and newspapers.
- Enclose titles of book chapters and journal articles in single quotation marks.

Page numbering

- Books: page numbers are not usually needed in the reference list. If they are, include them as the final item of the citation, separated from the preceding one by a comma and followed by a full stop.
- Journal articles: page numbers appear as the final item in the citation, separated from the preceding one by a comma and followed by a full stop.

  Use the abbreviations p. for a single page, and pp. for a page range, e.g. pp. 11–12.

Whole citation

- The different details, or elements, of each citation are separated by commas.
- The whole citation finishes with a full stop.

Specific Rules

Definite rules for several categories of publications are provided below:

Journal

Kumar, P & Garde, RJ 1989, 'Potentials of water hyacinth for sewage treatment', *Research Journal of Water Pollution Control Federation*, vol. 30, no. 10, pp. 291–294.

Monograph

Hyem, T & Kvale, O (eds) 1977, *Physical, chemical and biological changes in food caused by thermal processing*, 2nd edn, Applied Science Publishers, London, UK.

Chapter in a monograph

Biale, JB 1975, 'Synthetic and degradative processes in fruit ripening', eds NF Hard & DK Salunkhe, in *Post-harvest biology and handling of fruits and vegetables*, AVI, Westport, CT, pp. 5–18.

Conference proceedings

Common, M 2001, 'The role of economics in natural heritage decision making', in *Heritage economics: challenges for heritage conservation and sustainable development in the 21st century: Proceedings of the International Society for Ecological Economics Conference, Canberra, 4th July 2000*, Australian Heritage Commission, Canberra.

Website reference

Thomas, S 1997, *Guide to personal efficiency*, Adelaide University, viewed 6 January 2004, <http://library.adelaide.edu.au/~sthomas/papers/perseff.html>.

Report

McColloch, LP, Cook, HT & Wright, WR 1968, *Market diseases of tomatoes, peppers and egg-plants*, Agriculture Handbook no. 28, United States Department of Agriculture, Washington, DC.

Thesis

Cairns, RB 1965, 'Infrared spectroscopic studies of solid oxygen', PhD thesis, University of California, Berkeley, CA.

Footnotes, spelling and measurement units

If footnotes are used, they should be numbered in the text, indicated by superscript numbers and kept as brief as possible. The journal follows the spelling and hyphenation of standard British English. SI units of measurement are to be used at all times.

Submission of Articles

General. Manuscripts should be submitted (electronically) in *MS Word* format. If submitted as hard copy, two copies of the manuscript are required, double-spaced throughout on one side only of A4 (21.0 × 29.5 cm) paper and conform to the style and format of the *ASM Science Journal*. Intending contributors will be given, on request, a copy of the journal specifications for submission of papers.

Title. The title should be concise and descriptive and preferably not exceed fifteen words. Unless absolutely necessary, scientific names and formulae should be excluded in the title.

Address. The author's name, academic or professional affiliation, e-mail address, and full address should be included on the first page. All correspondence will be only with the corresponding author (should be indicated), including any on editorial decisions.

Abstract. The abstract should precede the article and in approximately 150–200 words outline briefly the objectives and main conclusions of the paper.

Introduction. The introduction should describe briefly the area of study and may give an outline of previous studies with supporting references and indicate clearly the objectives of the paper.

Materials and Methods. The materials used, the procedures followed with special reference to experimental design and analysis of data should be included.

Results. Data of significant interest should be included.

Figures. If submitted as a hard copy, line drawings (including graphs) should be in black on white paper. Alternatively sharp photoprints may be provided. The lettering should be clear. Halftone illustrations may be included. They should be submitted as clear black and white prints on glossy paper. The figures should be individually identified lightly in pencil on the back. All legends should be brief and typed on a separate sheet.

Tables. These should have short descriptive titles, be self explanatory and typed on separate sheets. They should be as concise as possible and not larger than a Journal page. Values in tables should include as few digits as possible. In most cases, more than two digits after the decimal point are unnecessary. Units of measurements should be SI units. Unnecessary abbreviations should be avoided. Information given in tables should not be repeated in graphs and vice versa.

Discussion. The contribution of the work to the overall knowledge of the subject could be shown. Relevant conclusions should be drawn, and the potential for further work indicated where appropriate.

Acknowledgements. Appropriate acknowledgements may be included.

Reprints. Twenty copies of reprints will be given free to all the authors. Authors who require more reprints may obtain them at cost provided the Editorial Committee is informed at the time of submission of the manuscript.

Correspondence

All enquiries regarding the ASM Science Journal, submission of articles, including subscriptions to it should be addressed to:

The Editor-in-Chief
ASM Science Journal
Academy of Sciences Malaysia
902-4, Jalan Tun Ismail
50480 Kuala Lumpur, Malaysia.
Tel: 603-2694 9898; Fax: 603-2694 5858
E-mail: sciencejournal@akademisains.gov.my

ASM SCIENCE JOURNAL
(ASM Sc. J.)

ORDER FORM

Subscription (Two issues per year)

	Malaysia	Other Countries
Individual	**RM100**	**USD50**
Institution	**RM200**	**USD100**

1. Complete form and return.

Name/Institution: .....
(Please print)
.....
.....

Street Address: .....
.....
.....

City, Region: .....

Country, Postal Code: .....

2. Payment method: Cheque/Bank Draft/Postal Order/ Money Order No.: .....
Payable to **"Akademi Sains Malaysia"**
(Please include bank commission, if applicable)
RM/USD: .....

Date: ..... Signature: .....

Please send to:
Academy of Sciences Malaysia
902-4, Jalan Tun Ismail
50480 Kuala Lumpur, Malaysia
Tel: 03-2694 9898; Fax: 03-26945858
E-mail: sciencejournal@akademisains.gov.my

ASM Science JOURNAL
In Pursuit of Excellence in Science

Affix
stamp
here

Academy of Sciences Malaysia
902-4, Jalan Tun Ismail
50480 Kuala Lumpur
Malaysia

RESEARCH ARTICLES

REVIEW

ANNOUNCEMENTS